Lehrstuhl für THERMODYNAMIK

MASTER'S THESIS

Effect of Hydrodynamics on the Early Stages of Particle Deposition in Membrane Systems

Einfluss der Hydrodynamik auf die Anfangsphase der Ablagerung von Partikeln in Membransystemen

Autor:
Raphaela Allgayer

Matrikel-No:
03647602

Betreuer:
Prof. Dr.-Ing. Thomas Sattelmayer
Andreas Kastl, M.Sc.

August 20, 2020

Lehrstuhl für Thermodynamik
Prof. Dr.-Ing. Thomas Sattelmayer

Erklärung

Hiermit versichere ich, die vorliegende Arbeit selbständig verfasst zu haben. Ich habe keine anderen Quellen und Hilfsmittel als die angegebenen verwendet.

Ort, Datum	Raphaela Allgayer

Abstract

Seawater desalination and the effective treatment of problematic wasterwaters mitigate the growing global water scarcity. In particular, processes which are facilitated by a semi-permeable membrane have gained popularity for water treatment. Although, in recent years, the efficiency of such processes has increased significantly through progress in material engineering of the membranes and optimizing the hydrodynamic conditions in the membrane modules, there is still room for improvement. Especially colloidal deposition on the membranes and concentration polarization lower the processing volume and impede the continuous operation of such water treatment plants. This thesis, which is based on analogous experimental studies, numerically investigates particle transport in a forward osmosis module. By resolving the forces which act on a particle in a fluid flow, the trajectories of the particles can be compared to the streamlines of the fluid flow. In this scope, the local variations in permeate water flux resulting from concentration polarization are incorporated into the model. While the particles in the main flow follow the streamlines of the channel flow with impermeable walls, the influence of the permeate water flux becomes increasingly important as the particle is transported closer to the membrane. In close proximity to the membrane local variations in permeate water flux resulting from concentration polarization also affect the particle trajectory. The resulting residence time distribution of the particles in the forward osmosis channel allows for the prediction of the deposition probability, which increases as the permeate water flux increases and as the crossflow velocity decreases. The local particle distribution within one spacer element can be attributed to the dominant particle transport mechanisms.

Kurzfassung

Meerwasserentsalzung und die effektive Aufbereitung problematischer Abwässer tragen wesentlich zur Bekämpfung der sich verschärfenden globalen Wasserknappheit bei. Hierbei haben besonders Prozesse, die durch semipermeable Membranen ermöglicht werden, große Popularität erlangt. Obwohl die Effizienz dieser Prozesse in den letzen Jahren durch die Verbesserung der Selektivität der Membranen und durch die Optimierung der Strömungsbedingungen in den Membranmodulen strark zugenommen hat, besteht nach wie vor Optimierungspotential. Ins Besondere die Ablagerung kolloidaler Partikel auf der Membran und Konzentrationspolarisation mindern den Durchsatz und verhindern den unterbrechungsfreien Betrieb der Anlagen. Basierend auf experimentellen Ergebnissen zur Partikelablagerung untersucht diese Arbeit numerisch den Transport von Partikeln in einem Vorwärtsosmosemodul. Durch das Aufstellen eines detaillierten Kräftegleichgewichts am Partikel können die Trajektorien der Partikel mit den Stromlinien des Fluids verglichen werden. Hierbei wird insbesondere die lokale Variation des Permeatstroms auf Grund von Konzentrationspolarisation berücksichtigt. Während die Partikel in der Hauptströmung den Stromlinien der Kanalströmung ohne Permeatstrom folgen, nimmt der Einfluss des Permeatstroms auf die Partikeltrajektorien mit abnehmender Distanz zur Membran zu. In unmittelbarer Nähe zur Membran wirken sich auch die lokalen Unterschiede des Permeatstroms auf die Trajektorien der Partikel aus. Somit kann mit Hilfe der Verweilzeitverteilung der Partikel in der Strömung eine vergleichende Vorhersage über die Ablagerungswahrscheinlichkeit der Partikel bei verschiedenen hydrodynamischen Bedingungen getroffen werden. Die Ablagerungswahrscheinlichkeit der Partikel nimmt mit dem Permeatstrom zu und mit der Durchschnittsgeschwindigkeit der Kanalströmung ab. Die lokale Verteilung der abgelagerten Partikel kann mit den Kräften, die auf einen Partikel im Fluid wirken, in Verbindung gebracht werden.

Contents

List of Figures **ix**

List of Tables **xi**

Nomenclature **xiv**

1 Introduction **2**

2 Theoretical Background **4**
2.1 Forward Osmosis Basics 4
2.1.1 Governing Equations for Hydrodynamic Mass Transport 4
2.1.2 Membrane Transport 7
2.2 Linear Momentum Conservation for a Single Particle 15
2.2.1 Volume Forces 17
2.2.2 Fluid Forces from the Undisturbed Flow 21
2.2.3 Fluid Forces from the Disturbance Flow 22
2.2.4 Saffman Lift Force 26
2.2.5 Relative Importance of the Force Components 27

3 Implementation **30**
3.1 Discretization - The Finite Volume Method 30
3.1.1 Convection Term 31
3.1.2 Diffusion Term 33
3.1.3 Source Term 33
3.2 Solvers 34
3.2.1 Solution Algorithm for the Ideal Channel Flow 36
3.2.2 Solution Algorithm for the Real Channel Flow 37
3.2.3 Numerics of Particle Transport 39
3.3 Implementation of Particle Forces 40
3.4 Boundary Conditions for the Membrane 40
3.4.1 Membrane Water Flux 41
3.4.2 Membrane Salt Flux 41
3.5 Case Set-Up 42
3.5.1 Meshing 42

3.5.2 Grid Convergence . . . 43
3.5.3 Flow Field Boundary Conditions . . . 45
3.5.4 Particles . . . 47

4 Results and Discussion **50**
4.1 Validation of the Membrane Transport . . . 50
4.2 Validation of the Particle Model . . . 50
4.3 Characterization of the Channel Flow . . . 52
4.4 Trajectories of Single Particles . . . 56
4.4.1 Particle Trajectories in the Bulk of the Channel Flow depend on Crossflow Velocity, Permeate Water Flux and Initial Point of Release . . . 56
4.4.2 Concentration Polarization Influences Deposition of Particles . . . 59
4.4.3 Comparison of the Results for the Single Particles to the Literature . . . 62
4.5 Deposition Patterns . . . 62
4.5.1 Uniform Deposition at Low Crossflow and High Permeate Water Flux . . . 63
4.5.2 Lower Deposition in Recirculation Zone and in Region of High Shear Stress 65
4.5.3 Particle Size Distribution of Deposited Particles Confirms Dominant Regional Deposition Mechanisms . . . 66

5 Conclusions and Future Work **68**

A Appendix **78**
A.1 OpenFOAM® . . . 78
A.2 Grid Convergence Study . . . 78
A.3 Additional Validation Case . . . 78
A.4 Detailed Analysis of Flow Characteristics at the Membrane . . . 80
A.5 Additional Particle Trajectories . . . 80
A.6 Control Experiments . . . 80
A.7 Particle Size Distribution for the Deposition Studies . . . 80

List of Figures

2.1 Process scheme of a forward osmosis plant. 5
2.2 Experimental set-up to visualize the osmotic pressure of a solution. 9
2.3 Schematic of a membrane facilitated desalination module with the possible operating modes for such a set-up. 10
2.4 Course of the concentration over the cross section of a forward osmosis membrane. 13
2.5 Geometrical framework for the derivation of the momentum conservation equation for a single particle. 16
2.6 Geometric features of the van der Waals attraction betwen a spherical particle and a flat plate. 19
2.7 Models for the interaction between a solid surface and an electrolyte solution. . . 20
2.8 DLVO theory. 21
2.9 Standard drag curve for a spherical particle. 24
2.10 Relevant forces on a particle in a membrane channel flow set-up. 28

3.1 Exemplary mesh cell with compass notation convention. 32
3.2 Flow diagram for the solvers in this thesis. 35
3.3 Algorithm of the concentration polarization solver. 38
3.4 Simplified geometry of a spacer-filled forward osmosis channel. 43
3.5 Flow diagram of the meshing procedure. 44

4.1 Comparison of the particle trajectories calculated by Chellam et al. [16] with the particle trajectories determined with the present model. 51
4.2 Characteristic flow profiles in a channel with zig-zag spacer configuration. 53
4.3 Concentration polarization in a forward osmosis channel with zig-zag spacer configuration. 55
4.4 Residence time of the particles in the channel and particle trajectories at low uniform crossflow velocity. 57
4.5 Close-ups of the particle trajectories. 60
4.6 Particle deposition pattern. 63

A.1 Grid convergence indices. 79
A.2 Comparison of the particle trajectories of large particles ($d = 26\mu$m) calculated by Chellam et al. [16] with the particle trajectories determined with the present model. 79

A.3 Local salt mass fraction and permeate water flux at the membrane. 81
A.4 Particle trajectories over four spacer elements at high and medium crossflow velocity and uniform permeate flux. 82
A.5 Particle trajectories over four spacer elements considering concentration polarization. 83
A.6 Control experiment for the comparison of the particle deposition of the ideal with the real case. 84
A.7 Rosin-Rammler particle size distribution. 84

List of Tables

3.1 Discretization schemes for the governing equations of the fluid phase. 31
3.2 Solution settings for fluid phase equations. 34
3.3 Crossflow and permeate velocities for the simulations. 46
3.4 Mass transport coefficients and resulting bulk salt mass fractions. 47

4.1 Relative reduction of volume flow in the feed channel at various initial crossflow rates and fixed permeate velocities. 54
4.2 Permeate water fluxes as calculated by the the simulation of the forward osmosis channel considering concentration polarization. 56
4.3 Particle residence time ratios. 58

Nomenclature

Latin Symbols

a	Discretization parameter	-
A	Water permeability of the membrane	$\mathrm{m\,s^{-1}\,Pa^{-1}}$
A_c	Cross sectional area	$\mathrm{m^2}$
B	Salt permeability of the membrane	$\mathrm{m\,s^{-1}}$
c	Concentration	$\mathrm{mol\,dm^{-3}}$
C	Coefficient	-
C_S	Safety factor	-
d	Diameter	m
d_h	Hydraulic diameter	m
d_s	Thickness of the porous support layer	m
D	Diffusion Coefficient	$\mathrm{m^2\,s^{-1}}$
D	Dimensionality of the mesh	-
e	Elementary charge	C
E	Energy	J
f	Helmholtz free energy density	$\mathrm{J\,m^{-3}}$
f	Characteristic variable for the problem	various
$\vec{f}$	Force density	$\mathrm{N\,m^{-3}}$
F	Helmholtz free energy	J
$\vec{F}$	Force	N
$\vec{g}$	Gravitational acceleration	$\mathrm{m\,s^{-2}}$
G	Gibbs free energy	J
H	Hamaker constant	J
H	Height	m
H_1	Discretization parameter	-
I	Identity matrix	-
J_S	Solute flux through the membrane	$\mathrm{mol\,m^{-2}\,s^{-1}}$
J_S	Solute flux through the membrane	$\mathrm{kg\,m^{-2}\,s^{-1}}$
$\vec{J}_\mathrm{S}$	Solute flux in the fluid	$\mathrm{mol\,m^{-2}\,s^{-1}}$
J_W	Water flux through membrane	$\mathrm{m\,s^{-1}}$
k_B	Boltzmann constant	$\mathrm{J\,K^{-1}}$
L	Length	m
m	Mass	kg
n	Number concentration	$\mathrm{m^{-3}}$

$\vec{n}$	Outward pointing surface normal	-
N	Molar amount	mol
N_c	Number of cells	-
p	Pressure	Pa
p	Order of convergence	-
q	Atom density	m^{-3}
r	Radial coordinate	m
r_P	Radius of the particle	m
R	Minimal distance between two objects	m
S	Surface area	m^2
S	Structural parameter of the membrane	m
S	Source term	various
S_p	Numerical particle force coefficient	$\mathrm{N\,s\,m}^{-1}$
$\vec{S}_\mathrm{u}$	Numerical particle force parameter	N
t	Time	s
T	Temperature	K
$\vec{u}$	Velocity of the fluid in resting reference frame in absence of particle	$\mathrm{m\,s}^{-1}$
$\vec{U}$	Generic velocity	$\mathrm{m\,s}^{-1}$
$\vec{v}$	Velocity of fluid	$\mathrm{m\,s}^{-1}$
V	Volume	m^3
$\overline{V}$	Molar Volume	$\mathrm{m}^3\,\mathrm{mol}^{-1}$
$\vec{V}$	Velocity of the particle in resting reference frame	$\mathrm{m\,s}^{-1}$
w	Mass fraction	-
$\vec{w}$	Velocity of the particle in moving reference frame	$\mathrm{m\,s}^{-1}$
W	Work	J
$\vec{x}$	Coordinate in resting reference frame	m
y	One-dimensional integration coordinate	m
$\vec{Y}$	Location of particle in resting reference frame	m
z	Valency of ions	-
z	One-dimensional integration coordinate	m
$\vec{z}$	Coordinate in moving reference frame	m

Greek Symbols

β	Mass transport coefficient of the solute	$\mathrm{m\,s}^{-1}$
Γ	Generalized diffusion coefficient	various
δ	Thickness of diffusive boundary layer	m
ϵ	Porosity	-
ϵ_0	Permittivity in vacuum	$\mathrm{F\,m}^{-1}$
ϵ_r	Relative permittivity	-
η	Dynamic viscosity, first viscosity coefficient	Pa s

θ	Angular coordinate	-
κ_D	Inverse Debye length	m
λ	Second viscosity coefficient	Pa s
λ	London-van der Waals constant	Jm^6
λ_I	Characteristic interaction wavelength	m
μ	Chemical potential	$J mol^{-1}$
ν	Kinematic viscosity	$m^2 s^{-1}$
$\vec{\Omega}$	Angular momentum	s^{-1}
Π	Osmotic pressure	Pa
ρ	Density	$kg m^{-3}$
σ	Stress tensor	$N m^{-2}$
τ	Tortuosity	-
τ	Time integration variable	s
τ	Characteristic time	s
ϕ	Volume fraction	-
ϕ	Potential	J
ϕ_ζ	Zeta-potential	J
φ	Transport variable	various
ψ	Surface potential	V

Superscript

$'$	Phase with lower solute concentration, feed solution
$''$	Phase with higher solute concentration, draw solution
$\ominus$	Standard conditions
o	Undisturbed flow
$*$	Disturbance flow
c	Correction
eff	Effective
n	Current time step
p	Prediction

Subscript

1	Object 1
2	Object 2
3	Fluid between two objects
b	Bulk
bv	Value boundary
bg	Gradient boundary

B	Buoyant
c	Crossflow
ch	Channel
coarse	Coarse
conv	Convective
coupled	Coupled
crit	Critical
C	Colloidal
diff	Diffusive
D	Steady state drag
e	Eastern boundary of control volume
exp	Experiment
E	Eastern node
fine	Fine
Flow	Flow
edl	Electronic double layer
F	Fluid
G	Gravitational
h	hydraulic
H	History
i	Running index, component index
iv	Value internal
ig	Gradient internal
kin	Kinetic
L	Lift
m	Membrane
max	Maximal
medium	Medium
min	Minimal
n	Northern boundary of control volume
nb	Neighboring
N	Northern node
P	Node
P	Particle
s	Southern boundary of control volume
sim	Simulation
sp	specific
sp	Spacer
S	Southern node
s-∞	sphere-infinite plate
S	Solute, Salt
S	Surface
t	Total
uncoupled	uncoupled

vdW	van der Waals
very fine	Very fine
V	Volume
VM	Virtual mass
φ	Transport variable
w	Western boundary of control volume
w	wall
W	Western node
W	Solvent, water

Dimensionless Numbers

GCI	Grid convergence index
Re	Reynolds number of the channel flow
$\mathrm{Re_P}$	Particle Reynolds number
$\mathrm{Re_S}$	Shear Reynolds number
$\mathrm{Re_W}$	Permeate Reynolds number
Sc	Schmidt number
Sh	Sherwood number
St	Stokes number
ϱ	Refinement ratio
X	Characteristic geometry for van der Waals interaction
ζ	Dimensionless distance from channel center

1 Introduction

Providing safe and clean drinking water under the pressure of industrialization, an increasing global population and climate change poses one of major challenges of our time [28]. By 2025, two thirds of the population are predicted to live in water scarce countries worldwide [71]. While water is abundant on the blue planet, only 1 % of the global water resources are readily available as fresh water. The remainder is bound in the form of snow and ice (2 %) or occurs as saline seawater (97 %) [50]. Therefore, increased water reuse and desalination pose the only two methods to increase the global water supply [73].
Within the realm of desalination technologies, pressure-driven, membrane-facilitated processes have recently superseded conventional thermal desalination [22]. In reverse osmosis, which is the most common membrane-based desalination method, water is forced through a semi-permeable membrane by applying an elevated pressure to the saline feed water. As the membrane retains the salt in the feed stream, the products of the process are a pure water permeate and a brine with increased salt concentration [26]. The energy requirement of state-of-the-art reverse osmosis processes is ten times lower compared to thermal processes [70, 71], which are based on the selective evaporation or vaporization of water. However, producing 1 m^3 of desalinated water still requires 1.5 kWh to 2.5 kWh of electricity, which is the most significant cost factor in desalination [22, 49].
Forward osmosis is another membrane-facilitated process for water treatment, which exploits the osmotic pressure difference between a draw and a feed solution instead of hydraulic pressure to overcome the resistance of the membrane for water transport [14]. Consequently, forward osmosis is applied when the osmotic pressure of the feed water exceeds the mechanical stress which can be imposed on a membrane module [72]. In a second step, the permeated water is separated from the draw solute by reverse osmosis, by ultrafiltration or by chemical or physical means. Energy in the form of cheaper waste heat might suffice to recover the draw solute, if the high osmotic pressure on the draw side is generated by volatile gases [47, 48] or other thermolytically regenerable solutes [22]. Alternatively, water additives such as fertilizers can be used as draw solutes to make their separation from the product water obsolete [58] or the diluted draw solution can be discarded. As the energy requirement in such optimized processes is lower than in reverse osmosis, forward osmosis has been identified as a promising technology for the cost-effective generation of fresh water.
Besides facile recovery or beneficial properties in the application of the product water, an ideal draw solute must exhibit a low propensity for concentration polarization [72]. Concentration polarization describes the depletion or concentration of solute in proximity to the membrane, which reduces the effective driving force for osmotic water transport from the feed to the draw channel [45]. In addition to optimizing the physiochemical properties of the draw solute, concentration polarization can be mitigated by improving the hydrodynamic conditions in the feed and draw channels of the forward osmosis module. Both, increasing the

crossflow velocity [30] and promoting mixing in the channels through the incorporation of so-called spacers [1] reduces concentration polarization, because the phenomenon is strongly linked to the development of a diffusive boundary layer. Hence, larger solutes with a lower mobility give rise to more severe concentration polarization than smaller solutes. However, small solutes are also more likely to diffuse through the membrane into the feed channel [34]. While the concentration polarization in the feed channel due to selective transport across the membrane towards the draw channel is negligible when the solute concentration in the feed channel is low, backdiffusion of solute promotes concentration polarization. Furthermore, the draw solute might alter the pH and ionic strength of the feed [58] and thus enhance colloidal or cellular deposition and adsorption on the membrane.

While biofouling, i.e. the deposition of microorganisms on the membrane, is further enhanced by the presence of spacers in the feed channel [86], spacers decrease colloidal fouling [11, 42, 43, 79] and alter the deposition pattern on the membrane [53, 60]. By investigating the initial stages of particle and bacterial deposition in a forward osmosis module, Bogler et al. [9] and Kastl et al. [39] propose that biofilm formation after bacterial deposition is responsible for the distinct behavior of microbes compared to inert particles. The similar initial stages of deposition in bio- and colloidal fouling are mostly influenced by the interactions between particles and the membrane [22] and the hydrodynamic flow patterns in the channel [72]. On the one hand, high shear stress at high crossflow velocities reduces fouling, because particles are transported away from the membrane in this lift force dominated regime. On the other hand, an increase in permeate water flux promotes particle deposition on the membrane [10,16,60]. While particle deposition patterns in spacer filled channels have been investigated [38,43,60], little is known about the governing mechanisms of colloidal transport in such a channel. Various hydrodynamic conditions occur within one forward osmosis module. As the draw solute is depleted along the channel, the average permeate water flux through the membrane decreases. Simultaneously, the crossflow velocity in the feed channel also decreases as water permeates through the membrane. If the draw solution volume flux is large compared to the permeate water flux, the reduction in crossflow velocity in the feed channel is more pronounced than the reduction of the permeate water flux. Accordingly, the drop in average permeate water flux is larger if the draw solution volume stream is comparably low. Each hydrodynamic flow condition induces a specific concentration polarization pattern, which alters the density of the fluid and the local permeate water flux. However, it remains unknown to what extend the crossflow velocity, the average permeate water flux and concentration polarization influence the particle trajectories in a forward osmosis channel. Furthermore, colloidal interactions between particles and membrane, which pose the ultimate deposition criterion, are altered by concentration polarization in the feed channel.

As concentration polarization cannot be decoupled from hydrodynamics in an experimental setup, this study applies computational fluid dynamics for investigating the influence of hydrodynamic flow conditions and concentration polarization on particle deposition in a forward osmosis feed channel. Ideal spacer filled channels without concentration polarization are compared to cases which consider the uneven salt distribution in the channel. A wide range of hydrodynamic conditions is investigated to elucidate various flow patterns and concentration polarization scenarios.

2 Theoretical Background

Both the conservation equations for the two component salt-water mixture and the transport of particles in a continuous phase are incorporated into the deposition and particle transport model of the forward osmosis channel. Therefore, this chapter first discusses the fluid mechanics of the continuous two-component salt water phase with an emphasis on the water and salt transport through a forward osmosis membrane. The second part of the chapter elaborates on the force components which are exerted on a solid particle in a continuous fluid. The resulting Newton force equation is the basis for computing the trajectories of the particles.

2.1 Forward Osmosis Basics

In a forward osmosis module, two thin channels are separated by a selectively permeable membrane. A continuous stream of untreated water flows through the feed channel, while the process solution is passed through the draw channel of the module. As water is transported across the membrane which rejects the solute, the feed solution is concentrated and leaves the channel as so-called brine or concentrate. Simultaneously, the permeate water flux dilutes the solution in the draw channel. In a subsequent process unit, the diluate is separated into the pure product water and the concentrated draw solution. The latter is re-fed into the forward osmosis module, possibly after dilution with the diluate. Figure 2.1 shows a basic forward osmosis process scheme. The subsequent sections first summarize the physical laws which govern hydrodynamic flow in the channels before the particularities of membrane transport are discussed.

2.1.1 Governing Equations for Hydrodynamic Mass Transport

The flow conditions within each of the channels are comparable to channel flows in closed channels, such as e.g. heat exchangers [41]. The physical laws which describe the motion of a Newtonian fluid are the conservation equations for mass, energy and momentum. Many elementary textbooks cover the derivation and discussion of the following conservation equations. In assembling this section, we referred to Atkins et al. [5] and von Böckh et al. [84].

Mass Conservation of the Fluid - Continuity Equation

The continuity equation states that mass cannot be created or destroyed. The mass which is contained in a control volume can, therefore, only be altered by flux across its surfaces or a change in density within the control volume. Thus, when a control volume experiences a net

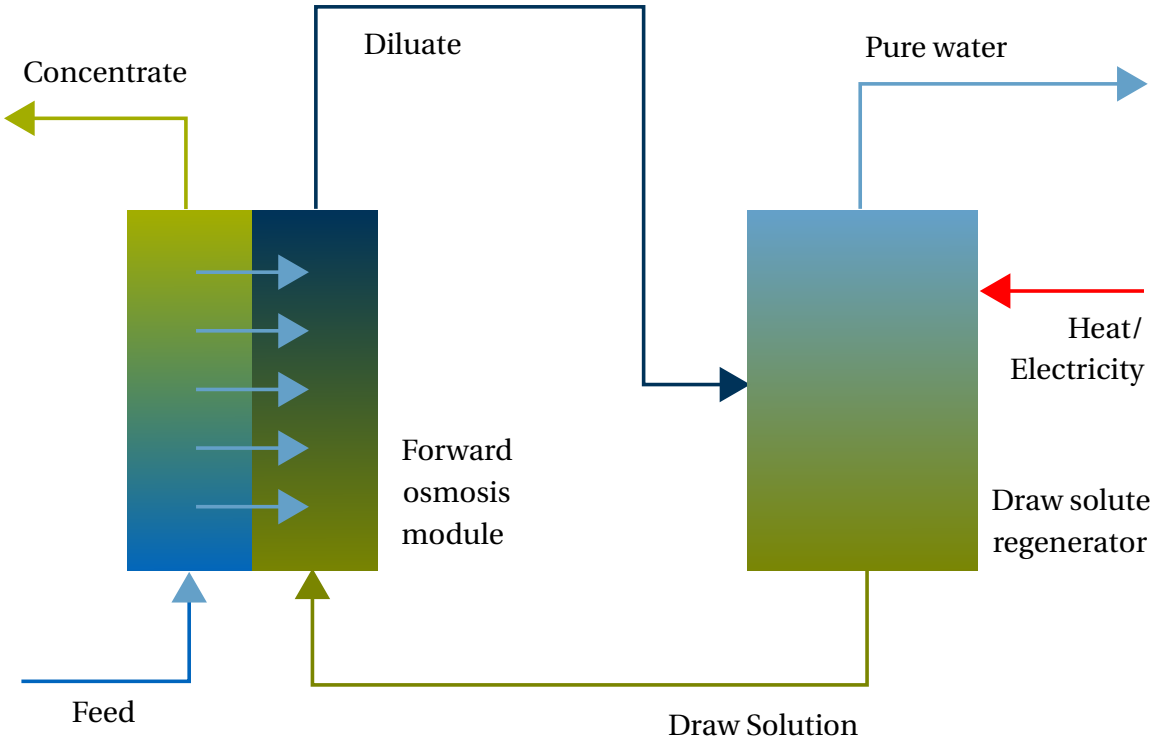

Figure 2.1: Process scheme of a forward osmosis plant. Adapted from [22].

influx of fluid, the density of the enclosed fluid increases

$$\int_S \rho_F \vec{v} \cdot \vec{n} \, dS = -\frac{\partial}{\partial t} \int_V \rho_F \, dV. \tag{2.1}$$

$\vec{n}$ is the outward pointing normal of the surface S of the control volume V. $\vec{v}$ denotes the velocity of the fluid and ρ_F is its density. The time variable is t. Applying the Gauss theorem, equation 2.1 is integrated to yield the general form of the continuity equation

$$\frac{\partial \rho_F}{\partial t} + \nabla \cdot \left(\rho_F \vec{v} \right) = 0. \tag{2.2}$$

For an incompressible fluid, the density is constant, such that the continuity equation reduces to

$$\nabla \cdot \vec{v} = 0. \tag{2.3}$$

Mass Conservation of the Salt - Diffusion-Convection Equation

Mass conservation does not only apply to the overall mass of the fluid, but also to each of the species that the fluid is made up of. Thus, the mass of solute within a control volume is

$$\frac{\partial c_S}{\partial t} + \nabla \cdot \vec{J}_{S,t} = S_S. \tag{2.4}$$

Analogously to the continuity equation (equation 2.2), c_S is the molar concentration of the solute and $\vec{J}_{S,t}$ is the total flux of the solute over the surface of the control volume. Here, the concentration of the solute is chosen instead of the density of the fluid to describe the change in the conservation variable within the volume. Conversely to the overall mass, a species can be converted into another species during a chemical reaction. Thus, a source term for the species S_S is introduced to account for these changes. However, salt water is an inert fluid, such that the source term is zero for the salt conservation in a FO module.
The overall solute flux across the surface of the control volume consists of a convective component $\vec{J}_{S,conv}$ and a diffusive component $\vec{J}_{S,diff}$, which are linearly independent. With Fick's law for the diffusive flux in binary mixtures

$$\vec{J}_{S,diff} = -D_{WS}\nabla c_S \tag{2.5}$$

the overall salt flux is

$$\vec{J}_{S,t} = \vec{J}_{S,conv} + \vec{J}_{S,diff} = c_S\vec{v} - D_{WS}\nabla c_S. \tag{2.6}$$

D_{WS} is the binary diffusion coefficient of the solute in water. Inserting equation 2.6 into equation 2.4, we obtain the diffusion-convection equation for salt conservation

$$\frac{\partial c_S}{\partial t} + \nabla\cdot(c_S\vec{v} - D_{WS}\nabla c_S) = S_S. \tag{2.7}$$

Momentum Conservation - Navier-Stokes Equation

Forces that are exerted on a body give rise to a change in its momentum. Applied to a fluid control volume of mass m_F, Newton's second law is

$$\vec{F} = \frac{\partial(m_F\vec{v})}{\partial t}. \tag{2.8}$$

$\vec{F}$ is the overall force on the control volume, which consists of body forces $\vec{F}_{V,F}$ and surface forces $\vec{F}_S$. Surface forces are made up of a component perpendicular to the surface of the control volume, which is the pressure gradient, and the forces from the fluid stress tensor $\boldsymbol{\sigma}$ which act parallel to the surface of the control volume ΔV

$$\vec{F} = \vec{F}_{V,F} + \vec{F}_S = \left(\vec{f}_{V,F} + \nabla p + \boldsymbol{\sigma}\cdot\nabla\right)\Delta V, \tag{2.9}$$

where $\vec{f}_{V,F}$ is the body force on the fluid normalized by the volume and p is the pressure.
The right-hand side of equation 2.8 encompasses a change in momentum within the boundaries of the control volume as well as a change in momentum resulting from the temporal shift of the control volume boundaries

$$\frac{\partial(m_F\vec{v})}{\partial t} = \left(\frac{\partial\left(\rho_F\vec{v}\right)}{\partial t} + (\vec{v}\cdot\nabla)\left(\rho_F\vec{v}\right)\right)\Delta V. \tag{2.10}$$

Inserting equations 2.9 and 2.10 into equation 2.8 yields the most general form of the momentum conservation equation

$$\vec{f}_{V,F} + \nabla p + \boldsymbol{\sigma}\cdot\nabla = \frac{\partial\left(\rho_F\vec{v}\right)}{\partial t} + (\vec{v}\cdot\nabla)\left(\rho_F\vec{v}\right). \tag{2.11}$$

For water or salt water, which are Newtonian fluids, the strain rate is proportional to the stress rate of the fluid and the fluid is isotropic, such that the stress tensor becomes

$$\boldsymbol{\sigma} = \eta_{\mathrm{F}} \left(\nabla \vec{v} + (\nabla \vec{v})^{T} \right) + \lambda_{\mathrm{F}} (\nabla \cdot \vec{v}) \boldsymbol{I}. \tag{2.12}$$

Here, $\boldsymbol{I}$ is a 3×3 identity matrix. η_{F} is the first viscosity coefficient of the fluid or more commonly the dynamic viscosity and λ_{F} is the second viscosity coefficient, also referred to as volume viscosity. For an incompressible or weakly compressible fluid, the second term of equation 2.12 is approximately zero because of mass conservation (equation 2.3). Therefore, the incompressible Navier-Stokes equation is

$$\rho_{\mathrm{F}} \left(\frac{\partial \vec{v}}{\partial t} + (\vec{v} \cdot \nabla) \vec{v} \right) = -\nabla p + \nabla \cdot \left(\eta_{\mathrm{F}} \left(\nabla \vec{v} + (\nabla \vec{v})^{T} \right) \right) + \vec{f}_{\mathrm{V,F}}. \tag{2.13}$$

If the viscosity of the fluid is also constant, equation 2.13 further reduces to the most common form of the Navier-Stokes equation

$$\rho_{\mathrm{F}} \left(\frac{\partial \vec{v}}{\partial t} + (\vec{v} \cdot \nabla) \vec{v} \right) = -\nabla p + \eta_{\mathrm{F}} \Delta \vec{v} + \vec{f}_{\mathrm{V,F}}. \tag{2.14}$$

The models in this thesis apply equations 2.13 and 2.14 for the simulation of the salt water flux and the ideal pure water flux, respectively.

Energy Conservation - First Law of Thermodynamics

The first law of thermodynamics states that the overall work which is done to a control volume and the net flux of heat into the control volume is equal to its overall change of energy. However, salt-water separation processes which apply a selectively permeable membrane are approximately isothermal. Furthermore, the salt water is assumed to be only weakly compressible [25]. This implies that the density distribution in the forward osmosis channel originates exclusively from local variations of the salt mass fraction. The pressure does not influence the density of the fluid. Therefore, the energy conservation equation is decoupled from equations 2.2, 2.7 and 2.13 and, thus, not evaluated in this model.

2.1.2 Membrane Transport

In accordance with the second law of thermodynamics, mass transport across the membrane is driven by the desire of the overall system to reach a state of equilibrium. Thus, water is transported from the channel which exhibits a higher chemical potential to the channel with lower chemical potential [5]. After giving a brief overview over the thermodynamic and kinetic principles of the mass transport across the membrane, this section discusses the implications of these phenomena for the expected salt concentration profile across the membrane. The thermodynamic fundamentals which are introduced in the following are assembled from textbooks by Atkins et al. [5] and Doi [21].

Chemical Potential

The fundamental equation for the Gibbs free energy G of a binary solution with constant volume is

$$G(p, T, N_\mathrm{W}, N_\mathrm{S}) = pV + F(N_\mathrm{W}, N_\mathrm{S}, T). \tag{2.15}$$

T is the temperature. N_W and N_S are the molar amount of the solvent and the solute, respectively. As the Helmholtz free energy F is an extensive quantity, it scales with the mass of the solution. In an incompressible fluid, the Helmholtz free energy can thus be written as a product of the solution volume and the free energy density of the solution f. The latter then depends on the volume fraction of the solute ϕ_S and the temperature

$$G(p, T, N_\mathrm{W}, N_\mathrm{S}) = V\left(p + f(\phi_\mathrm{S}, T)\right). \tag{2.16}$$

The chemical potential μ of a component in a mixture is defined as its partial molar Gibbs free energy, such that

$$\mu_\mathrm{S} = \left(\frac{\partial G}{\partial N_\mathrm{S}}\right)_{p,T,N_\mathrm{W}} \quad \text{and} \quad \mu_\mathrm{W} = \left(\frac{\partial G}{\partial N_\mathrm{W}}\right)_{p,T,N_\mathrm{S}}. \tag{2.17}$$

Inserting equation 2.16 into equation 2.17, the chemical potential of the solvent is

$$\mu_\mathrm{W}(\phi_\mathrm{S}, p, T) = \overline{V}_\mathrm{W}\left(p + f(\phi_\mathrm{S}, T) - \phi_\mathrm{S}\frac{\partial f(\phi_\mathrm{S}, T)}{\partial \phi_\mathrm{S}}\right). \tag{2.18}$$

Analogously, the chemical potential of the solute becomes

$$\mu_\mathrm{S}(\phi_\mathrm{S}, p, T) = \overline{V}_\mathrm{S}\left(p + f(\phi_\mathrm{S}, T) - (1-\phi_\mathrm{S})\frac{\partial f(\phi_\mathrm{S}, T)}{\partial \phi_\mathrm{S}}\right). \tag{2.19}$$

$\overline{V}_\mathrm{S}$ and $\overline{V}_\mathrm{W}$ are the molar volumes of the two species.
In homogeneously mixing solutions, the chemical potential of the solute increases with the solute concentration, while the chemical potential of the solvent decreases with the solute volume fraction or concentration.[1] To minimize the overall free energy of the system, the solute in an isobaric system migrates towards lower solute concentrations. Simultaneously, the solvent is drawn to regions of higher solute concentration.

Osmotic Pressure

The equilibrating motion of molecules in a solution from regions of higher chemical potential to regions of lower chemical potential causes a force, which is quantified as the osmotic pressure of the solution. Figure 2.2 shows the set-up of an experiment which visualizes this pressure. In the experiment, the solution is brought into contact with its corresponding sol-

[1] Two chemical compounds mix readily if the overall free energy density of the system decreases through mixing. In contrast, phase separation is favored when each of the free energy densities of the two phases is lower than the free energy density of their solution. Therefore, two species form a homogenous solution if

$$\frac{\partial^2 f}{\partial \phi_\mathrm{S}^2} > 0 \tag{2.20}$$

is satisfied. Differentiating equations 2.18 and 2.19 with respect to the volume fraction of solute, it becomes obvious that $\partial\mu_\mathrm{S}/\partial\phi_\mathrm{S} > 0$ and $\partial\mu_\mathrm{W}/\partial\phi_\mathrm{S} < 0$ for homogeneously mixing solutions.

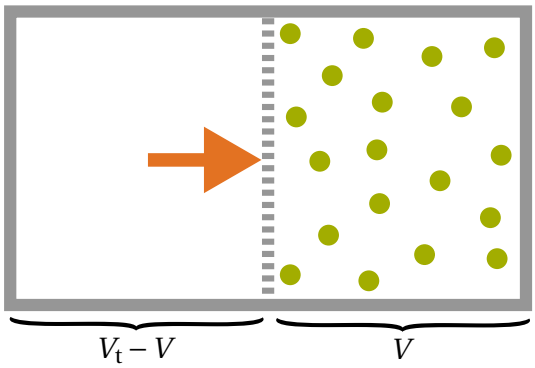

Figure 2.2: Experimental set-up to visualize the osmotic pressure of a solution. Adapted from [21].

vent through a semi-permeable membrane in a closed system. While the solvent can pass through the membrane, the membrane is impermeable for the solute. If the membrane could move freely, the solvent would pass through the membrane into solution until the solvent and the solution are fully mixed. Thus, a force must act on the membrane to prevent its motion. This force per unit area is the osmotic pressure. In other words, the work which is necessary to increase the solution volume by dV corresponds to the change of the overall Helmholtz free energy of the system

$$-\Pi \, \mathrm{d}V = \mathrm{d}F. \tag{2.21}$$

Π is the osmotic pressure of the solution. With the overall free energy of the system of total volume V_t

$$F = V f(\phi_S) + (V_t - V) f(0), \tag{2.22}$$

the osmotic pressure of the solution becomes

$$\Pi(\phi_S) = -f(\phi_S) + \phi_S \frac{\partial f(\phi_S, T)}{\partial \phi_S} + f(0, T). \tag{2.23}$$

When equation 2.20 holds, such that the solute and the solvent mix homogenously, the osmotic pressure of a solution increases with the solute volume fraction or concentration.
Lastly, we obtain a relationship between the osmotic pressure and the chemical potential by adding equations 2.18 and 2.23

$$\mu_W(\phi_S, p, T) = \overline{V}_W \left(f(0, T) + p - \Pi(\phi_S, T) \right) = \mu_W(0, p^\ominus, T) + \overline{V}_W \left(p - \Pi(\phi_S, T) \right) \tag{2.24}$$

$^\ominus$ denotes the reference state of the system, which is most commonly 25 °C and 1.013 bar. According to equation 2.24, the chemical potential of the solvent on both sides of a semi-permeable membrane can be altered by adjusting the osmotic pressure of the solution and/or the mechanical pressure in the compartment. As the solvent migrates from a region of higher chemical potential to a region of lower chemical potential (c.f. section 2.1.2), three major mechanisms for solvent transport across the membrane become conceivable. The process conditions for these three mechanisms are discussed in the following section.

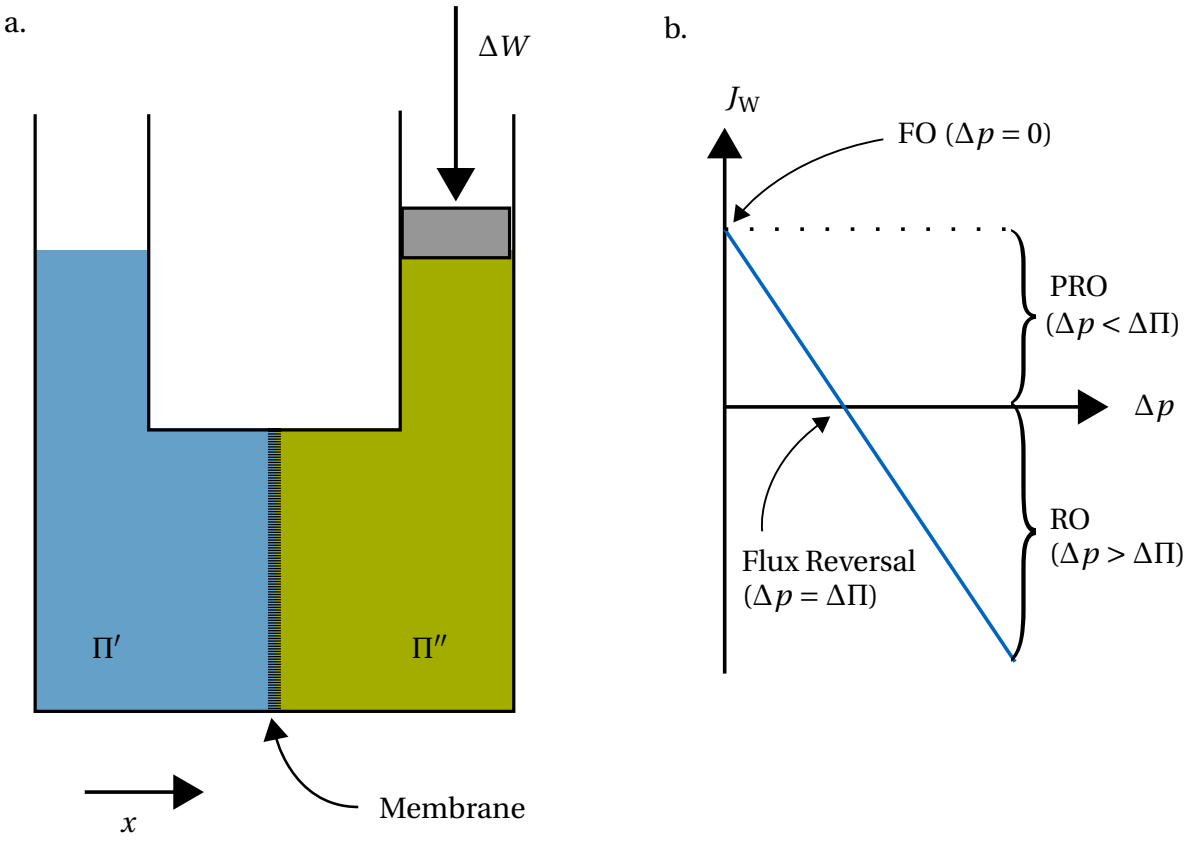

Figure 2.3: a. Schematic of a membrane facilitated desalination module with b. the possible operating modes for such a set-up. Adapted from [75] and [14].

Ideal Water Flux Across Semi-Permeable Membranes

In the case of desalination, the solvent is water and the solute is most often a soluble salt. Figure 2.3a schematically shows a desalination module, which consists of two chambers that are separated by a semi-permeable membrane. In the following, the indices $'$ and $''$ denote the left chamber and the right chamber, respectively. The reservoir on the left-hand side of the membrane is filled with a weakly saline solution. The compartment on the right side of the membrane contains highly saline water, which can be pressurized with a piston. Thus, the osmotic pressure on the right-hand side of the membrane is higher than the osmotic pressure in the open reservoir

$$\Pi' < \Pi'' \tag{2.25}$$

The membrane resistance for water transport and the friction of the piston are negligible. Let's first consider a case in which the piston can move freely, i.e. no work is done to the system. In such a scenario, the chemical potentials in the two solutions are

$$\mu'_W = \mu_W(0, p^\circ, T) + \overline{V}_W\left(p^\circ - \Pi'\right) \tag{2.26}$$

and

$$\mu''_{\mathrm{W}} = \mu_{\mathrm{W}}(0, p^{\ominus}, T) + \overline{V}_{\mathrm{W}}\left(p^{\ominus} - \Pi''\right). \tag{2.27}$$

As osmotic pressure on the left-hand side of the membrane is lower than on the right-hand side (equation 2.25), the chemical potential in the open reservoir is higher than in the compartment on the right-hand side

$$\mu'_{\mathrm{W}} > \mu''_{\mathrm{W}}. \tag{2.28}$$

Therefore, the water flows right and pushes the piston out until the difference in osmotic pressure between the two compartments is equal to the difference in hydrostatic pressure of the respective water columns. These operating conditions are applied in regular or forward osmosis. Here, the osmotic pressure difference is the sole driving force for the water transport between the two chambers and the water flux increases with the difference in osmotic pressures.

If a pressure Δp is imposed on the system through the piston, the comparison between the chemical potentials becomes more complex. While the expression for the chemical potential on the left-hand side remains unaltered compared to the first scenario (equation 2.26), the chemical potential on the right-hand side is now

$$\mu''_{\mathrm{W}} = \mu_{W}(0, p^{\ominus}, T) + \overline{V}_{\mathrm{W}}\left(p^{\ominus} + \Delta p - \Pi''\right). \tag{2.29}$$

By comparing the pressure terms of equations 2.26 and 2.29, we see that

$$\mu'_{\mathrm{W}} > \mu''_{\mathrm{W}} \qquad \text{if} \quad \Pi'' - \Pi' = \Delta\Pi > \Delta p. \tag{2.30}$$

The water is still transported right, but the driving force for the water transport is reduced by Δp. Pressure retarded osmosis operates under these conditions. The process exploits the difference in osmotic pressure between two solutions for power generation by creating a hydrostatic pressure in the chamber on the right-hand side.

Lastly, if the hydrostatic pressure that is imposed on the system is larger than the osmotic pressure difference between the two chambers, the chemical potential on the right-hand side becomes larger than the chemical potential on the left-hand side

$$\mu'_{\mathrm{W}} < \mu''_{\mathrm{W}} \qquad \text{if} \quad \Pi'' - \Pi' = \Delta\Pi < \Delta p. \tag{2.31}$$

The water flows from the region with higher salinity to the region of lower salinity. This operating mode which is called reverse osmosis is the most common operating mode in seawater desalination. While membrane transport in forward osmosis and pressure retarded osmosis does not require external energy, reverse osmosis relies on electrically operated pumps which generate the hydrostatic pressure in the chamber on the right-hand side.

As equation 2.24 and the above considerations suggest, the water flux J_{W} across the membrane in Figure 2.3a is proportional to the overall pressure difference between the two sides of the membrane [14]

$$J_{\mathrm{W}} = A\left(\Delta\Pi - \Delta p\right). \tag{2.32}$$

A is the water permeability of the membrane, which is a correction factor for the resistance of the membrane for water flux. Figure 2.3b summarizes the operating modes of membrane desalination.

Real Water Flux Across Semi-Permeable Membranes

Several simplifications are made in the derivation of equation 2.32. First, the membrane is assumed to be completely impermeable for salt. Although commercially available membranes exhibit high salt rejections, real membranes are not fully impermeable for the solute [57]. Therefore, back diffusion of solute towards the region of lower chemical potential must be incorporated into the model [78]. Second, the solutions on both sides of the membrane are considered ideally mixed, such that there are no concentration gradients within the chambers and the solute concentration at the membrane corresponds to the bulk solute concentration. However, due to the (partial) salt rejection of the membrane, the salt concentration in the laminar boundary layer of the feed channel increases, while the laminar boundary layer on the draw side is depleted of salt [45]. This phenomenon is referred to as external concentration polarization. Lastly, equation 2.32 assumes that the membrane is homogenous in the permeation direction. Yet, real desalination membranes commonly consist of an active layer which rejects the salt and a porous support layer which stabilizes the membrane. Within the porous support layer, convection is negligible, such that the mass transport is diffusion controlled. The resulting so-called internal concentration polarization in the support layer replaces the external concentration polarization on the respective side of the membrane [45].[2] In forward osmosis, the support layer most commonly faces the draw channel, which is free of particulate matter that could clog the pores of the support layer. Thus, the dilutive external concentration polarization on the draw side becomes internal. Figure 2.4 depicts the cross section of the membrane in a forward osmosis set-up. The effective water flux between the feed and the draw channel is determined by the difference in osmotic pressure across the active layer of the membrane Π_m [78]

$$J_\mathrm{W} = A\left(\Delta\Pi_\mathrm{m}\right) \tag{2.33}$$

Thus, back diffusion of salt, external concentration polarization and internal concentration polarization reduce the net water flux across the membrane compared to the ideal model in equation 2.32. If the chemical potential of the solute increases linearly with the solute concentration,[3] the reverse salt flux is [57]

$$J_\mathrm{S} = -B\left(c''_\mathrm{m} - c'_\mathrm{m}\right). \tag{2.34}$$

B is the permeability of the membrane for the solute. The signs are chosen such that fluxes in x direction are positive. With the surface film theory, we can obtain an expression for the salt concentrations on the surface of the active layer to determine the effective salt and water fluxes across the membrane.
When water is transported across the membrane, the salt is mostly rejected on the feed side, such that the water flux dilutes the solution in the porous support layer. However, some salt still passes through the membrane and is convectively transported within the support layer. Simultaneously, salt from the bulk diffuses into the membrane as the region in the porous

[2] Strictly speaking, this is also a simplification, because some external concentration polarization also occurs on the support layer. However, this concentration polarization is negligible compared to the internal concentration polarization within the support layer [45].

[3] This approximation is valid in ideal solutions or when the solute concentration is very small.

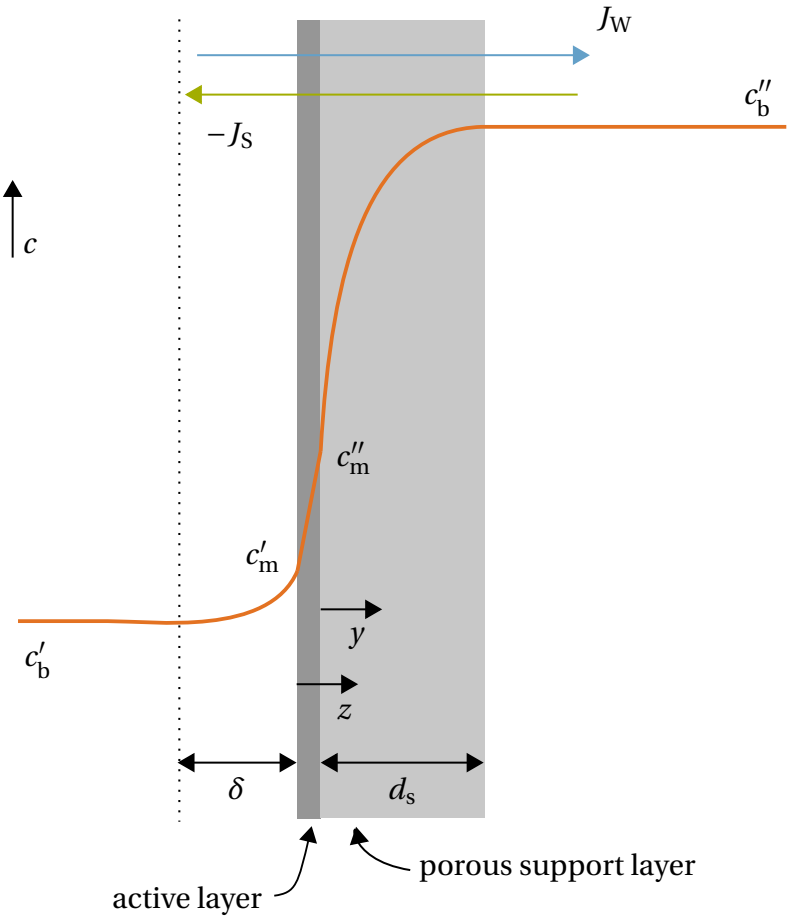

Figure 2.4: Course of the concentration over the cross section of a forward osmosis membrane. The porous support layer faces the draw solution. Adapted from [45].

support which is depleted of salt exhibits a lower chemical potential. With Fick's law for the diffusive flux (equation 2.5), the net salt flux in the support layer is therefore [78]

$$J_S = -D_{SW}^{eff} \frac{dc(y)}{dy} + J_W c(y). \tag{2.35}$$

D_{SW}^{eff} is the effective binary diffusion coefficient of salt in water corrected for the porosity ϵ and tortuosity τ of the support layer [57]

$$D_{SW}^{eff} = D_{SW} \frac{\epsilon}{\tau}. \tag{2.36}$$

At steady state, the salt mass flux in the porous support (equation 2.35) is equal to the salt flux across the active layer of the membrane (equation 2.34). Thus, integrating equation 2.35 from the surface of the active layer to the thickness of the support d_s yields an expression for the salt concentration at the membrane as a function of the bulk salt concentration in the draw

channel and the concentration difference across the active layer [46]

$$c''_{\mathrm{m}} = \underbrace{c''_{\mathrm{b}} \exp\left(-\frac{J_{\mathrm{W}} S}{D_{\mathrm{SW}}}\right)}_{\substack{\text{dilutive internal} \\ \text{concentration polarization}}} + \underbrace{\frac{B}{J_{\mathrm{W}}}(c''_{\mathrm{m}} - c'_{\mathrm{m}})\left(\exp\left(-\frac{J_{\mathrm{W}} S}{D_{\mathrm{SW}}}\right) - 1\right)}_{\text{back diffusion}}. \tag{2.37}$$

Here, the first term accounts for the depletion of salt in the support layer due to dilution by the transmembrane water flux and the second term captures the depletion of salt because of back diffusion of the salt into the feed channel [78]. $S = d_{\mathrm{s}}\tau/\epsilon$ is the structural parameter of the membrane.

Similar to equation 2.35, the net salt flux in the laminar boundary layer on the feed side of the membrane consists of a diffusive component which transports the salt away from the membrane into the bulk of the solution and a convective component which accounts for the salt that is transported with the convective water flux across the membrane

$$J_{\mathrm{S}} = -D_{\mathrm{SW}} \frac{\mathrm{d}c(z)}{\mathrm{d}z} + J_{\mathrm{W}} c(z). \tag{2.38}$$

At steady state, the salt flux through the boundary is equal to the salt flux across the membrane, such that equation 2.38 is integrated across the thickness of the boundary layer δ with equation 2.34. Parallel to equation 2.37, we obtain an expression for the salt mass fraction at the feed side of the active layer [78]

$$c'_{\mathrm{m}} = \underbrace{c'_{\mathrm{b}} \exp\left(\frac{J_{\mathrm{W}}}{\beta}\right)}_{\substack{\text{concentrative external} \\ \text{concentration polarization}}} - \underbrace{\frac{B}{J_{\mathrm{W}}}(c''_{\mathrm{m}} - c'_{\mathrm{m}})\left(1 - \exp\left(\frac{J_{\mathrm{W}}}{\beta}\right)\right)}_{\text{back diffusion}}. \tag{2.39}$$

Once again, the second term accounts for the increased salt concentration in the boundary layer resulting from leakage of the draw solute into the boundary layer. The first term accounts for the external concentration polarization on the surface of the membrane, as the water flux through the membrane transports salt to its surface which is rejected there. The mass transfer coefficient within the boundary layer is $\beta = D_{\mathrm{SW}}/\delta$, where δ is the thickness of the boundary layer.

Equations 2.37 and 2.39 implicitly provide the salt concentrations on both sides of the membrane. After some manipulation and inserting the expressions into equation 2.34 the reverse salt flux in forward osmosis becomes

$$J_{\mathrm{S}} = -B \left\{ \frac{c''_{\mathrm{b}} \exp\left(-\frac{J_{\mathrm{W}} S}{D_{\mathrm{SW}}}\right) - c'_{\mathrm{b}} \exp\left(\frac{J_{\mathrm{W}}}{\beta}\right)}{1 + \frac{B}{J_{\mathrm{W}}}\left(\exp\left(\frac{J_{\mathrm{W}}}{\beta}\right) - \exp\left(-\frac{J_{\mathrm{W}} S}{D_{\mathrm{SW}}}\right)\right)} \right\}. \tag{2.40}$$

For salt concentrations below 1.6 M, the salt mass fraction is approximately proportional to the osmotic pressure [27, 80]. If this simplification holds, equations 2.37 and 2.39 can also be inserted into equation 2.33 to yield an expression for the effective water flux across a forward osmosis membrane as a function of the respective bulk osmotic pressures

$$J_{\mathrm{W}} = A \left\{ \frac{\Pi''_{\mathrm{b}} \exp\left(-\frac{J_{\mathrm{W}} S}{D_{\mathrm{SW}}}\right) - \Pi'_{\mathrm{b}} \exp\left(\frac{J_{\mathrm{W}}}{\beta}\right)}{1 + \frac{B}{J_{\mathrm{W}}}\left(\exp\left(\frac{J_{\mathrm{W}}}{\beta}\right) - \exp\left(-\frac{J_{\mathrm{W}} S}{D_{\mathrm{SW}}}\right)\right)} \right\}. \tag{2.41}$$

2.2 Linear Momentum Conservation for a Single Particle

While the previous section covers the specifics of the fluid transport in forward osmosis modules, the following section investigates the motion of particles in a channel with a permeable membrane.
Most of the equations in this chapter are assembled from Maxey and Riley's [44] thorough derivation of the forces that act on a particle in a laminar flow regime, as well as from textbooks by Crowe et al. [19] and Michaelides [52]. Equations and thoughts which originate from another source are explicitly marked with the appropriate citation.
The motion of a small rigid sphere with diameter d_P located at $\vec{Y}(t)$ in a non-uniform flow can be derived from the Navier-Stokes equation (equation 2.14) and the continuity equation for incompressible fluids (equation 2.3). In a coordinate frame that moves at velocity $\vec{V}(t)$ with the center of the spherical particle, i.e. the origin $\vec{z}$ of the new reference frame is located at $\vec{z} = \vec{x} - \vec{Y}(t)$ with respect to the origin $\vec{x}$ of the resting reference frame, the velocity $\vec{w}$ of the particle is $\vec{w}(\vec{z}, t) = \vec{v}(\vec{x}, t) - \vec{V}(t)$. Expressed in the moving reference frame, equations 2.14 and 2.3 become

$$\rho_\mathrm{F} \frac{\mathrm{D}(\vec{w} + \vec{V})}{\mathrm{D}t} = \rho_\mathrm{F} \left(\frac{\partial \vec{w}}{\partial t} + \frac{\partial \vec{V}}{\partial t} + (\vec{w} \cdot \nabla)\vec{w} \right) = -\nabla p + \eta_\mathrm{F} \Delta \vec{w} + \vec{f}_{\mathrm{V,F}} \tag{2.42}$$

and

$$\nabla \cdot \vec{w} = 0, \tag{2.43}$$

respectively.[4] In equations 2.42 and 2.43 the derivatives are evaluated with respect to the new reference frame, whose coordinates are described by the vector $\vec{z}$. The geometric framework of the derivation is summarized in Figure 2.5. In the moving reference frame, the boundary conditions become

$$\vec{w}(\vec{z} \to \infty) = \vec{u} - \vec{V} \tag{2.45}$$

for the velocity infinitely far away from the particle and the no-slip boundary condition on the surface of the particle

$$\vec{w}(\vec{z} = d_\mathrm{P}/2) = \vec{\Omega} \times \vec{z}. \tag{2.46}$$

Here, $\vec{\Omega}$ is the angular velocity of the particle and $\vec{u}$ is the fluid flow field in the resting reference frame in absence of the particle. To further simplify equation 2.42, the flow field $\vec{w}$ is split into a part that describes the undisturbed flow $\vec{w}^o$ and the disturbance flow $\vec{w}^*$, which is caused by the particle, such that

$$\vec{w}^o = \vec{w} - \vec{w}^* = \vec{u} - \vec{V} \tag{2.47}$$

[4] The notation

$$\frac{\mathrm{D}}{\mathrm{D}t} = \frac{\partial}{\partial t} + (\vec{U} \cdot \nabla) \tag{2.44}$$

was chosen for the material derivative. The first term of the material derivative describes the temporary change and the second term describes the local change, which is characterized by the transport velocity $\vec{U}$ in the respective reference frame. Thus, the material derivative describes the rate of change of a vector or scalar field in a volume element which is transported at the velocity $\vec{U}$.

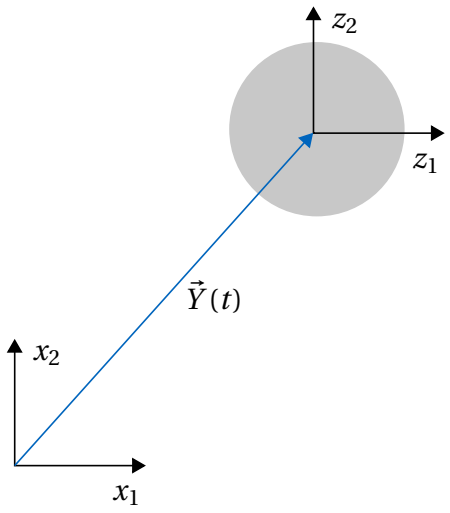

Figure 2.5: Geometrical framework for the derivation of the momentum conservation equation for a single particle.

is satisfied. This yields two momentum conservation equations, each of which fulfills continuity and can be evaluated seperatly. Equation 2.42 for the undisturbed flow is

$$\rho_{\mathrm{F}}\left(\frac{\partial \vec{w}^{o}}{\partial t}+\frac{\partial \vec{V}}{\partial t}+(\vec{w}^{o}\cdot\nabla)\,\vec{w}^{o}\right)=-\nabla p^{o}+\eta_{\mathrm{F}}\Delta\vec{w}^{o}+\vec{f}_{\mathrm{V,F}}. \tag{2.48}$$

With restriction of the analysis to low Reynolds number flows ($\mathrm{Re}\ll 1$), the advective terms $(\vec{w}^{*}\cdot\nabla)\,\vec{w}^{*}$ of the disturbance flow become negligible and the linear momentum conservation equation reduces to

$$\rho_{\mathrm{F}}\frac{\partial \vec{w}^{*}}{\partial t}=-\nabla p^{*}+\eta_{\mathrm{F}}\Delta\vec{w}^{*}. \tag{2.49}$$

Analogously, the boundary conditions for the disturbance are

$$\vec{w}^{*}(\vec{z}\to\infty)\to 0 \tag{2.50}$$

and

$$\vec{w}^{*}(\vec{z}=d_{\mathrm{P}}/2)=-(\vec{u}-\vec{V})+\vec{\Omega}\times\vec{z}, \tag{2.51}$$

while the boundary conditions of the undisturbed flow are the boundary conditions of the flow field without particles. To facilitate the treatment of the disturbance term, the body force is accounted for in equation 2.48.
According to Newton's second law (equation 2.8), the net force acting on a particle is the time derivative of its linear momentum

$$\vec{F}=\frac{\mathrm{d}(m_{\mathrm{P}}\vec{V})}{\mathrm{d}t}. \tag{2.52}$$

The forces that act on a particle immersed in a fluid flow can be categorized into body forces $\vec{F}_{\mathrm{V,P}}$ and surface forces $\vec{F}_{\mathrm{S}}$ (c.f. Section 2.1.1). Equation 2.52 applied to Maxey and Riley's simplifications of the Navier-Stokes equation is thus

$$m_{\mathrm{P}}\frac{\mathrm{d}\vec{V}}{\mathrm{d}t} = \sum \vec{F} = \sum \vec{F}_{\mathrm{V,P}} + \vec{F}_{\mathrm{S}}^{o} + \vec{F}_{\mathrm{S}}^{*} = \sum \vec{F}_{\mathrm{V,P}} + \oint_{S} \vec{n}\cdot\boldsymbol{\sigma}^{o}\,\mathrm{d}S + \oint_{S} \vec{n}\cdot\boldsymbol{\sigma}^{*}\,\mathrm{d}S. \tag{2.53}$$

The mass of the particle is assumed to be constant. $\boldsymbol{\sigma^o}$ and $\boldsymbol{\sigma}^*$ are the surface stress tensors of the undisturbed flow and the disturbance, respectively. Body forces are independent of the flow conditions, whereas surface forces result from the fluid velocity field. The following sections discuss the forces which act on particles in a fluid flow.

2.2.1 Volume Forces

Body forces act through the center of the particle. In the scope of this thesis, the most relevant forces are the gravitational force as well as the colloidal forces, i. e. van der Waals attraction and electrostatic double layer repulsion. Other examples for body forces, which are not discussed here, include Coulomb and magnetic forces.

Gravitational Force

The most prominent body force is the gravitational force $\vec{F}_{\mathrm{G}}$

$$\vec{F}_{\mathrm{G}} = m_{\mathrm{P}}\vec{g} = \rho_{\mathrm{P}} V_{\mathrm{P}}\vec{g}. \tag{2.54}$$

$\vec{g}$ denotes the gravitational acceleration. ρ_{P} and V_{P} are the particle density and volume, respectively.

Colloidal Force

The interaction between two solids in an electrolyte solution is governed both by the attractive van der Waals force and by electrostatic double layer repulsion between their surface charges. While the surface chemistry of the two solids determines the relative contribution of the two independent forces to the overall interaction, the flow conditions do not influence these solid-solid interactions. Hence, the van der Waals force and the electrostatic double layer force can be mathematically treated as body forces in the definition of equation 2.53.
The probabilistic motion of electrons in a chemical compound gives rise to temporarily non-uniform electron distributions in molecules and atoms. These so-called statistic dipoles induce uneven charge distributions in their neighboring atoms, which in turn cause further dipoles in their proximity. Through this mechanism, statistic dipoles propagate themselves until they experience interference by another statistic dipole. In accordance with their origin, induced dipoles are oriented such that neighboring atoms and molecules attract each other. Thus, the van der Waals force, in general, pulls two atoms, molecules or colloidal particles towards each other.
The overall van der Waals potential ϕ_{vdW} is the sum of the interaction potentials of all atom

pairs in the approaching bodies. For convenience, their individual contribution is accounted for by the product of the volume element and the local material-specific atom density

$$\phi_{\mathrm{vdW}} = -\int_{V_1} \mathrm{d}V_1 \int_{V_2} \mathrm{d}V_2 \frac{q_1 q_2 \lambda_{12}}{r^6}. \tag{2.55}$$

The strength of the interaction thus decreases sharply with the distance r between the volume elements $\mathrm{d}V_1$ and $\mathrm{d}V_2$ of particles 1 and 2 with total volumes V_1 and V_2 and atom densities q_1 and q_2, respectively [33]. λ_{12} is the London-van der Waals constant of the material pair. Through integration, Hamaker [33] obtains the van der Waals potential between a spherical particle and an infinite mass bound by a flat plate, which represents the membrane [16, 74]

$$\phi_{\mathrm{vdW,s-\infty}} = -\frac{H_{12}}{12}\left(\frac{1}{X} + \frac{1}{X+1} + 2\ln\frac{X}{X+1}\right). \tag{2.56}$$

Here, $H_{12} = \pi^2 q_1 q_2 \lambda_{12}$ is the Hamaker constant and the characteristic geometry is $X = R/d_{\mathrm{P}}$. R represents the closest distance between the particle surface and the infinite plate [33].[5] The geometric features of the problem are summarized in Figure 2.6.
The derivation of equation 2.56 does not consider the matter between the bodies. Thus, it is only valid for a particle and a flat plate in vacuum. However, the statistic dipoles of the atoms in the fluid between the objects also interact with the atoms in the particles and therefore contribute to the overall van der Waals force. Hence, equation 2.55 must be expanded by a three-way integration (Figure 2.6) to include the interactions of each atom with the material between the bodies (matter 3) and the interactions of the atoms in matter 3 with all the atoms in particles 1 and 2. Visser et al. [82] show that this adjustment reduces to a modification of the Hamaker constant

$$H_{132} \approx \left(\sqrt{H_{11}} - \sqrt{H_{33}}\right)\left(\sqrt{H_{22}} - \sqrt{H_{33}}\right), \tag{2.57}$$

where $H_{ii} = \pi q_i^2 \lambda_{ii}$ is the interaction of each material with itself. Another shortcoming of the Hamaker theory is that it does not consider the finite propagation time of the underlying electromagnetic interactions. This evokes retardation effects, which become significant at larger distances between the interacting bodies [54]. Thus, Gregory et al. [29] proposed

$$\phi_{\mathrm{vdW,s-\infty}} = -\frac{H_{132} d_{\mathrm{P}}}{12R}\left(\frac{1}{1 + 14R/\lambda_{\mathrm{I}}}\right) \tag{2.58}$$

as an approximation for the retarded van der Waals interactions between a sphere and a flat plate, which sufficiently fits the exact but cumbersome Clayfield calculations [18]. λ_{I} refers to the characteristic interaction wavelength of the problem, which is approximately 100 nm [29].
The electrostatic double layer force, which quantifies the electrostatic interaction between two charged particles in an electrolyte solution, counteracts the van der Waals force if the two particles exhibit opposite surface charge. These surface charges originate from the uncoordinated bonds on the surface of the particle or from material-specific covalently bound functional groups. The ions in solution assemble themselves around these charged surfaces which

[5] Particle-particle, i.e. sphere to sphere, interactions can be evaluated in a similar manner. However, their derivation is not discussed here, as they are only relevant in sophisticated models of channel flows that exhibit medium to high particle concentrations [35].

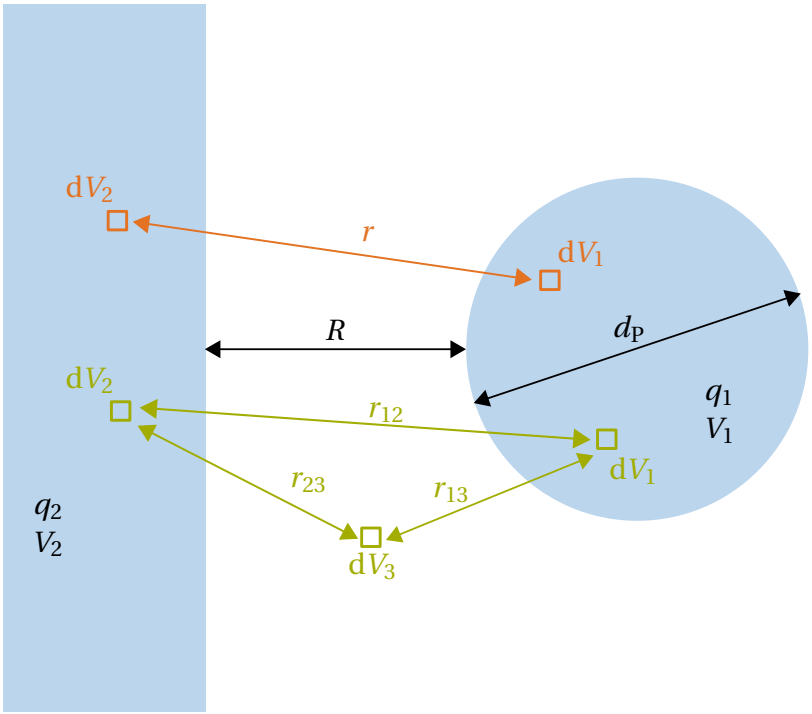

Figure 2.6: Geometric features of the van der Waals attraction betwen a spherical particle and a flat plate. Adapted from [33]

alters the ideal exponential decay of the surface potential into the solution (Figure 2.7) [5]. In a first simplified model, Helmholtz [85] postulated a loose bond of solvatized ions to the surface of the particle which results in a linear decrease of the potential. However, this model does not capture the thermal mobility of the electrolyte. Thus, the Guoy-Champan theory [15, 31] assumes a diffuse ion cloud in proximity to the charged surface, where the ions of opposite charge assemble closer to the surface than the ions that exhibit the same charge as the surface. In fact, the combination of these two models best represents the actual ion distribution. Solvatized ions bind to the charged surface, but there is a diffuse ion layer farther away from the surface which enables a gradual transition to the solution potential [76]. Surface potential measurements yield the so-called ζ-potential ϕ_ζ, which corresponds to the potential on the outer surface of the Helmholtz layer. The ζ-potential differs from the solution potential, but also from the surface charge of the particle. This observation confirms the double layer theory; the particle cannot be stripped of the bound inner ions, but the Helmholtz layer also does not suffice to reach the solution potential. With these considerations, the potential of a charged particle which approaches a charged flat surface ϕ_{edl} is

$$\phi_{\mathrm{edl}} = \frac{\pi}{2}\epsilon_0\epsilon_{\mathrm{r}} d_P \left\{ 2\psi_1\psi_2 \ln\left[\frac{1+\exp(-\kappa_{\mathrm{D}}R)}{1-\exp(-\kappa_{\mathrm{D}}R)}\right] + (\psi_1^2+\psi_2^2)\ln\left[1-\exp(-2\kappa_{\mathrm{D}}R)\right]\right\}. \tag{2.59}$$

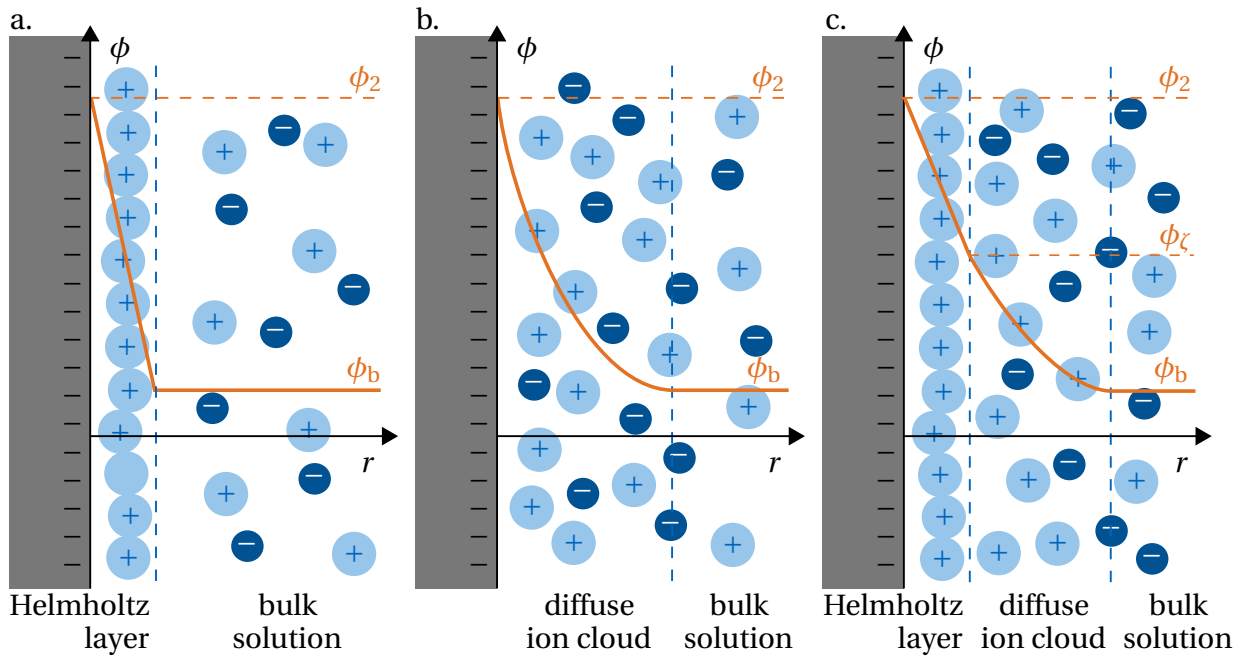

Figure 2.7: a. Helmholtz, b. Guoy-Chapman and c. Stern model for the interaction between a solid surface and an electrolyte solution. Adapted from [5].

ϵ_0 is the permittivity in vacuum, ϵ_r the permittivity of water, ψ_1 and ψ_2 are the surface potentials of the spherical particle and the plane and κ_D is the inverse Debye length, which depends on the ion number concentration n_i in solution and the temperature T

$$\kappa_D = \sqrt{\frac{e^2 \sum n_i z_i^2}{\epsilon_0 \epsilon_r k_B T}}. \tag{2.60}$$

Here, k_B denotes the Boltzmann constant, e the elementary charge and z_i is the valency of ion i [36].
According to the Derjaguin Landau Verweey Overbeek (DLVO) theory [20, 81], the colloidal force $\vec{F}_C$ is the sum of the van der Waals $\vec{F}_{vdW}$ and the double layer force $\vec{F}_{edl}$ or the negative gradient of the sum of the respective potentials

$$\vec{F}_C = \vec{F}_{vdW} + \vec{F}_{edl} = -\nabla(\phi_{vdW} + \phi_{edl}). \tag{2.61}$$

The resulting overall potential exhibits a maximum and two minima (Figure 2.8). When a particle approaches a surface, it "falls" into the secondary minimum, which corresponds to a non-stable equilibrium separation distance. However, if the (thermal) kinetic energy of the particle is larger than the maximum potential, it can overcome the energetic barrier and reach the primary minimum. This state corresponds to an irreversible attachment of the particle to the membrane [5].
While the van der Waals potential remains approximately constant, the electrostatic double layer is compressed as the ionic strength increases. This lowers the energetic barrier and attachment becomes more likely. Thus, concentration polarization should be considered when

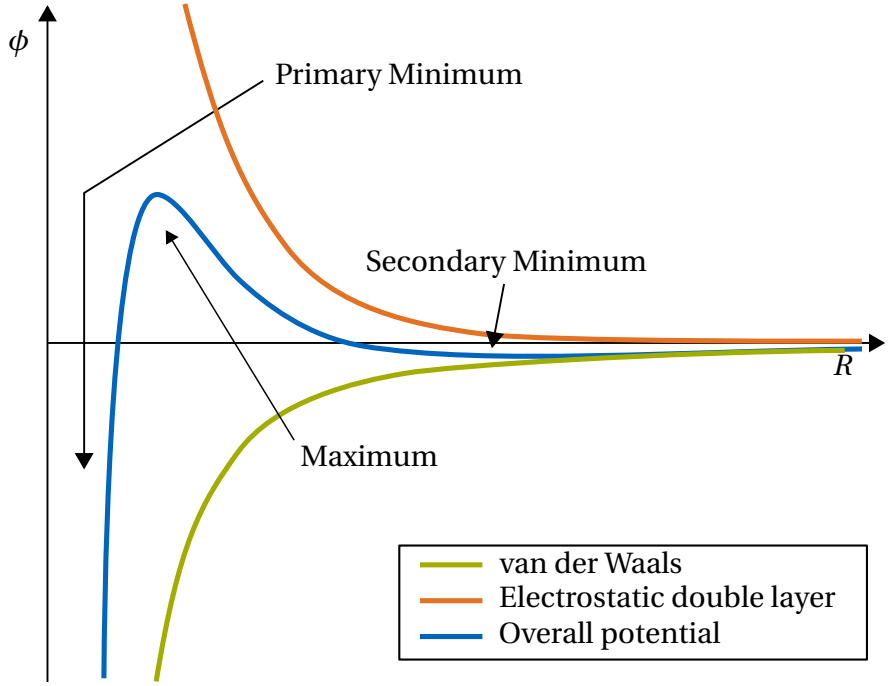

Figure 2.8: The DLVO theory describes the interactions between two particles by adding their electrostatic repulsion and their van-der-Waals attraction to obtain the potential between the particles as a function of their distance. Reprinted from [3].

explicitly resolving the colloidal forces in forward osmosis channels. As a simplification, Radu et al. [60] and Horstmeyer et al. [38] suggest that a particle always attaches if it is less than one particle diameter away from the membrane. However, this approach does not consider the influence of the kinetic energy of the particle on its attachment. Alternatively, an attachment criterion can be defined such that the particle sticks to the membrane if its kinetic energy is higher than the energetic barrier. Otherwise the particle rebounds from the surface. The latter approach is particularly useful in turbulent flows, when the grid resolution close to the wall is multiple orders of magnitude larger than the range of colloidal forces [35].

2.2.2 Fluid Forces from the Undisturbed Flow

Evaluating the first surface integral in equation 2.53 yields the force that is exerted on the particle by the undisturbed flow

$$\vec{F}_{\mathrm{S}}^{o} = \frac{\pi d_{\mathrm{P}}^{3}}{6}\left(-\nabla p + \eta_{\mathrm{F}} \Delta \vec{w}^{o}\right). \tag{2.62}$$

Together with the Navier-Stokes equation for the undisturbed flow (Equation 2.48) this force becomes

$$\vec{F}_{\mathrm{S}}^{o} = -\vec{F}_{\mathrm{V,F}} + m_{\mathrm{F}}\left(\frac{\partial \vec{w}^{o}}{\partial t} + \frac{\partial \vec{V}}{\partial t} + (\vec{w}^{o}\cdot\nabla)\,\vec{w}^{o}\right), \tag{2.63}$$

where $m_{\mathrm{F}} = \rho_{\mathrm{F}} V_{\mathrm{P}}$ is the mass of the fluid that occupies the volume of the particle. The additional body force corresponds to the buoyant force $\vec{F}_{\mathrm{B}}$

$$-\vec{F}_{\mathrm{V,F}} = \vec{F}_{\mathrm{B}} = -\rho_{\mathrm{F}}\vec{g}\,V_{\mathrm{P}}, \tag{2.64}$$

which results from the gradient of the hydrostatic pressure in the fluid. Transformed back into the resting reference frame, the fluid force on a particle from undisturbed flow is

$$\vec{F}_{\mathrm{S}}^{o} = \vec{F}_{\mathrm{B}} + m_{\mathrm{F}}\left(\frac{\partial \vec{u}}{\partial t} + (\vec{u}\cdot\nabla)\,\vec{u}\right). \tag{2.65}$$

Note that the force is now expressed in terms of the fluid flow field $\vec{u}$, which describes the flow field without particles instead of the overall flow field $\vec{v}$ which also accounts for the disturbance by the particles.

2.2.3 Fluid Forces from the Disturbance Flow

The second surface integral in equation 2.53, which accounts for the disturbance of the fluid by the particle, is not as straight forward to solve as the integral for the undisturbed flow. With an adaption of the Faxen symmetry relation for the steady Stokes flow and Burger's results for the point force flow, the disturbance surface integral in equation 2.53 is evaluated in terms of its Laplace transform to yield

$$\begin{aligned}\vec{F}_{\mathrm{S}}^{*} &= \overbrace{3\pi\eta_{\mathrm{F}} d_{\mathrm{P}}\left[(\vec{u}-\vec{V}) + \frac{d_{\mathrm{P}}^{2}}{24}\Delta\vec{u}\right]}^{\text{steady state drag}} + \overbrace{\frac{1}{2}m_{\mathrm{F}}\frac{\mathrm{d}}{\mathrm{d}t}\left[(\vec{u}-\vec{V}) + \frac{d_{\mathrm{P}}^{2}}{40}\Delta\vec{u}\right]}^{\text{virtual mass term}} \\ &+ \overbrace{\frac{3}{2}\pi\eta_{\mathrm{F}} d_{\mathrm{P}}^{2}\int_{0}^{t}\left[\frac{\frac{\mathrm{d}}{\mathrm{d}\tau}\left(\vec{u}-\vec{V}+\frac{d_{\mathrm{P}}^{2}}{24}\times\Delta\vec{u}\right)}{\pi\nu_{\mathrm{F}}(t-\tau)^{0.5}}\right]\mathrm{d}\tau}^{\text{Basset or history term}}.\end{aligned} \tag{2.66}$$

τ is the integration variable for the time and ν_{F} is the kinematic viscosity of the fluid. With equation 2.66, the forces from the disturbance flow can now be determined from the flow field in absence of particles and the velocity of the particles. The following considerations are about the three force terms in equation 2.66, namely steady state drag, virtual mass and Basset force.

Steady state Drag Force

The steady state drag force acts on particles which exhibit a constant velocity relative to the fluid flow. When a body force accelerates a particle in a fluid flow, the steady state drag force counteracts this acceleration, such that the particle moves at constant velocity. An example for such a behavior is the steady settling of a spherical particle under the influence of gravity. The second term of the steady state drag force, which depends on the curvature of the fluid velocity profile, is the Faxen force [23]. Its contribution to the steady state drag force is negligible if the particle is much smaller than the channel, such that the velocity profile in the vicinity of the particle is approximately uniform. Under these prerequisites, Reynolds number effects prevail. These effects are accounted for by the first term of the steady state drag force.
The drag coefficient C_D was introduced to quantify this Reynolds number-dependent momentum transfer between the two phases [32,66]. If the carrier phase is homogenous, viscous and isotropic, the drag coefficient is a scalar, such that the simplified steady state drag force becomes

$$\vec{F}_\mathrm{D} = \frac{1}{2} C_\mathrm{D} \rho_\mathrm{F} A_\mathrm{c,P} |\vec{u} - \vec{V}| (\vec{u} - \vec{V}) \tag{2.67}$$

with the cross-sectional area of the dispersed phase $A_\mathrm{c,P}$

$$A_\mathrm{c,P} = \frac{\pi}{4} d_\mathrm{P}^2. \tag{2.68}$$

For solid, non-rotating, spherical particles, the relationship between the particle Reynolds number $\mathrm{Re_P}$ and the drag coefficient is given in the standard drag curve (Figure 2.9). The particle Reynolds number is defined as

$$\mathrm{Re_P} = \frac{\rho_\mathrm{F} d_\mathrm{P} |\vec{u} - \vec{V}|}{\eta_\mathrm{F}}. \tag{2.69}$$

At low Reynolds numbers, the laminar velocity profile of the carrier phase around a spherical particle can be determined analytically. Stokes [77] obtained

$$\vec{F}_\mathrm{D} = 3\pi d_\mathrm{P} \eta_\mathrm{F} (\vec{u} - \vec{V}) \tag{2.70}$$

for the drag force of a spherical solid particle in the so-called Stokes flow regime ($\mathrm{Re_P} < 1$). Comparing the coefficients of equations 2.67 and 2.70 yields the analytical expression

$$C_\mathrm{D} = \frac{24}{\mathrm{Re_P}} \tag{2.71}$$

for the drag coefficient. Thus, in the laminar flow regime, the drag coefficient is proportional to the inverse of the particle Reynolds number. As the velocity increases, the flow begins to detach and to form vortices behind the sphere, which increases the pressure difference between the forward and the rearward stagnation point and thus the drag coefficient. In the regime of Newton's drag law ($750 < \mathrm{Re_P} < 3 \times 10^5$), the detachment is fully developed, such that the drag coefficient is approximately constant at $C_\mathrm{D} = 0.445$. At the critical Reynolds number $Re_\mathrm{P,crit} \approx 3 \times 10^5$, the boundary layer becomes turbulent and the drag coefficient decreases

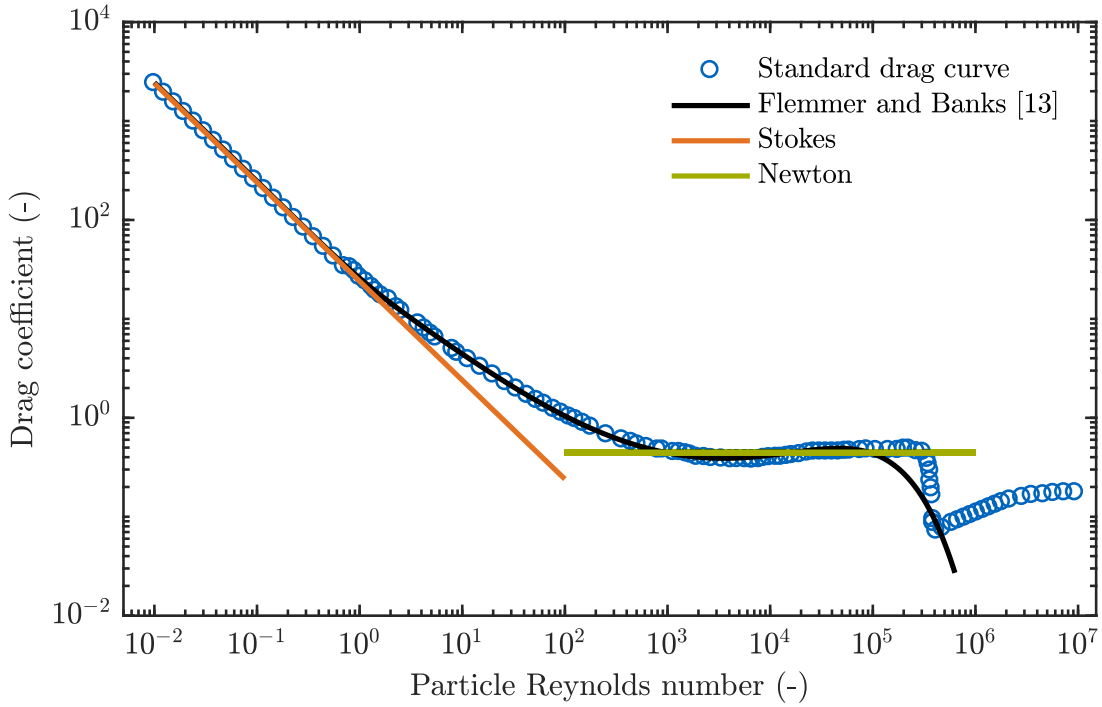

Figure 2.9: Influence of the particle Reynolds number $\mathrm{Re_P}$ on the drag coefficient of a spherical particle. Adapted from [19].

sharply.[6] Building on previously published models, Flemmer and Banks [24] determined the empirical relationship

$$C_\mathrm{D} = \frac{24 \times 10^{A}}{\mathrm{Re_P}} \quad \text{with} \quad A = 0.261\ \mathrm{Re_P^{0.369}} - 0.105\ \mathrm{Re_P^{0.431}} - \frac{0.124}{1 + (\log(\mathrm{Re_P}))^2} \tag{2.72}$$

for the drag coefficient, which shows good fits up to $\mathrm{Re_P} = 1 \times 10^5$ and also captures the transition between the Stokes and the Newton regime.
Strictly speaking, the so-determined drag coefficients are only valid for non-rotating spheres. However, Rubinov and Keller [64] showed that the spin effect on the drag coefficient is negligible for particle Reynolds numbers up to $\mathrm{Re_P} \approx 1$, which are characteristic for most particle channel flows.

Virtual Mass Force

In contrast to the steady-state drag force, which acts at a constant relative velocity of the particle, the virtual mass force describes the drag due to acceleration of a particle relative to the fluid. The virtual mass effect originates from the concomitant acceleration of the surrounding fluid. In a control volume which is bound by the surface of the accelerating particle, i.e. the control volume encompasses all the fluid but not the particle, the kinetic energy E_kin of the

[6] With increasing surface roughness of the particle, the critical Reynolds number decreases.

fluid is

$$E_{\text{kin}} = \frac{1}{2}\rho_{\text{F}} \int_V \nabla \cdot (\phi \, \nabla\phi) \, \mathrm{d}V. \tag{2.73}$$

Here, the relative velocity of the fluid is expressed as the derivative of a potential function.[7] Accordingly, equation 2.43 becomes

$$\Delta\phi = 0. \tag{2.74}$$

Expanding equation 2.73 with the continuity equation (equation 2.74) and applying the divergence theorem yields

$$E_{\text{kin}} = \frac{1}{2}\rho_{\text{F}} \int_V \nabla \cdot (\phi \, \nabla\phi) \, \mathrm{d}V = \frac{1}{2}\rho_{\text{F}} \int_S \phi \, \nabla\phi \cdot \vec{n} \, \mathrm{d}S. \tag{2.75}$$

In spherical coordinates, the potential function of a sphere moving through a fluid is

$$\phi = -\frac{|\vec{w}| r_{\text{P}}^3}{2r^2} \cos\theta. \tag{2.76}$$

Here, r_{P} is the radius of the particle, r is the radial coordinate and θ is an angular coordinate. With the surface element of the sphere $\mathrm{d}S$

$$\mathrm{d}S = r_{\text{P}}^2 \, \sin\theta \, 2\pi \, \mathrm{d}\theta \tag{2.77}$$

equation 2.75 becomes

$$E_{\text{kin}} = \frac{\pi\rho_{\text{F}} r_{\text{P}}^3 |\vec{w}|^2}{2} \int_0^{\pi} \cos^2\theta \sin\theta \, \mathrm{d}\theta = \frac{\pi\rho_{\text{F}} r_{\text{P}}^3 |\vec{w}|^2}{3}. \tag{2.78}$$

The norm of the virtual mass force $|\vec{F}_{\text{VM}}|$ results from the change rate of the kinetic energy of the fluid

$$|\vec{F}_{\text{VM}}| = \frac{1}{|\vec{w}|} \frac{\mathrm{d}E_{\text{kin}}}{\mathrm{d}t} = \frac{2\pi\rho_{\text{F}} r_{\text{P}}^3}{3} \frac{\mathrm{d}|\vec{w}|}{\mathrm{d}t} = \frac{1}{2} m_{\text{F}} \frac{\mathrm{d}|\vec{w}|}{\mathrm{d}t}. \tag{2.79}$$

Hence, phenomenologically, the virtual mass force is equivalent to increasing the mass of the particle by the mass of the fluid which occupies half the volume of the sphere.[8] In vector notation, the virtual mass force $\vec{F}_{\text{VM}}$ is

$$\vec{F}_{\text{VM}} = \frac{1}{2} m_{\text{F}} \frac{\mathrm{d}\vec{w}}{\mathrm{d}t} = \frac{1}{2} m_{\text{F}} \frac{\mathrm{d}}{\mathrm{d}t}(\vec{u} - \vec{V}), \tag{2.82}$$

[7] This is valid for inviscid and incompressible fluids.

[8] Strictly speaking, the force which is necessary to accelerate a mass m relative to a fluid flow is

$$\vec{F} = m\left(\frac{\mathrm{d}\vec{u}}{\mathrm{d}t} - \frac{\mathrm{d}\vec{V}}{\mathrm{d}t} + (\vec{u}\cdot\nabla)\vec{u}\right) \tag{2.80}$$

with the material derivative of the undisturbed flow. Indeed, Auton et al. [6, 7] showed that

$$\vec{F}_{\text{VM}} = \frac{1}{2} m_{\text{F}} \left(\frac{\mathrm{d}\vec{u}}{dt} - \frac{d\vec{V}}{\mathrm{d}t} + (\vec{u}\cdot\nabla)\vec{u}\right) \tag{2.81}$$

is the accurate representation of the virtual mass force. However, the difference between equation 2.82 and equation 2.81 is negligible for $\mathrm{Re}_{\text{P}} \ll 1$, which was assumed in the derivation of equation 2.66 [44].

which is equivalent to the first term of the virtual mass force in equation 2.66. As for the steady-state drag, the second term of the virtual mass force, i.e. the Faxen term, scales with

$$\left(\frac{d_\mathrm{P}}{2\,L_\mathrm{Flow}}\right)^2, \tag{2.83}$$

where L_Flow is the characteristic length scale of the flow. Thus, it is negligible for most particle-laden channel flows.

Basset Force

The Basset force accounts for the viscous drag upon acceleration of the particle. Phenomenologically, it describes the lag in boundary layer development resulting from a relative acceleration of the particle with respect to the fluid. Thus, the Basset force is of particular interest in transient cases, such as the gravitational acceleration of a particle in a still fluid or in oscillatory flow fields. In such cases, the diffusion of particle-induced vortices away from the sphere is limited by the relatively small displacement of the particle. The vortices which remain in proximity to the particle in turn influence its future motion, which explains the integral nature of the so-called history term. It encompasses the motion of the spherical particle from its initiation up to the present.
For a small, finite relative velocity of the particle with respect to the fluid, the magnitude of the history term is

$$\vec{F}_\mathrm{H} = \frac{3}{2}\pi\eta_\mathrm{F} d_\mathrm{P}^2 \left[\int_0^t \frac{\frac{\mathrm{d}}{\mathrm{d}\tau}\left(\vec{u}-\vec{V}+\frac{d_\mathrm{P}^2}{24}\times\Delta\vec{u}\right)}{\pi\nu_\mathrm{F}(t-\tau)^{0.5}}\mathrm{d}\tau + \frac{\vec{u}(t=0)-\vec{V}(t=0)}{t^{0.5}}\right]. \tag{2.84}$$

The evaluation of the integral, which is implicit in the velocity of the particle, requires a lot of computational resources. Reeks et al. [61] extended equation 2.66 to treat initially non-resting particles. While this facilitates the simulation of particle flows, an initial relative velocity between particle and fluid is physically incongruous with the assumption of an initially undisturbed flow field. In another attempt to minimize computational resources, Michaelides et al. [51, 83] analytically converted the integrodifferential equation into a second-order differential equation, which is explicit in the particle velocity. However, the numerical solution of this differential equation is only stable for particles which are significantly denser than the fluid.

2.2.4 Saffman Lift Force

One central assumption in Maxey and Riley's derivation of the forces that act on a particle in low Reynolds number flows is that the velocity and pressure gradient are small over the extension of the particle. However, in channel shear flows, the velocity difference between opposite sides of the particle might not be negligible, especially for larger particles. In such cases, a lower pressure develops on the high velocity side of the particle and the low velocity

on the other side gives rise to a high pressure. Under the assumption that the particle Reynolds number is much smaller than the square root of the shear Reynolds number Re_S

$$\mathrm{Re}_\mathrm{S} = \frac{d_\mathrm{P}^2}{\nu_\mathrm{F}} |\nabla \times \vec{u}|, \tag{2.85}$$

this pressure gradient causes the Saffman lift force $\vec{F}_\mathrm{L}$ [67]

$$\vec{F}_\mathrm{L} = 1.61\ C_\mathrm{L} \sqrt{\frac{\eta_\mathrm{F}\rho_\mathrm{F}}{|\nabla \times \vec{u}|}}\ d_\mathrm{P}^2 (\vec{u} - \vec{V}) \times (\nabla \times \vec{u}). \tag{2.86}$$

The magnitude of the Saffman lift force increases with the particle diameter and the velocity difference over the particle. C_L is the lift force coefficient, which is

$$C_\mathrm{L} = \begin{cases} \left(1 - 0.3314\beta^{0.5}\right) \exp\left(-\frac{\mathrm{Re_S}}{10}\right) + 0.3314\beta^{0.5} & \text{if } \mathrm{Re_S} \leq 40 \\ 0.0524\sqrt{\beta \mathrm{Re_S}} & \text{if } \mathrm{Re_S} > 40 \end{cases} \tag{2.87}$$

with

$$\beta = \frac{d_\mathrm{P}}{2\left|\vec{u} - \vec{V}\right|} |\nabla \times \vec{u}|. \tag{2.88}$$

The Saffman lift force pushes the particle towards its higher velocity side if the relative velocity is positive, i.e. the particle is travelling slower than the surrounding fluid. If the particle is faster than the continuous phase, the Saffman lift force acts towards the lower velocity side.

2.2.5 Relative Importance of the Force Components

Figure 2.10 summarizes the relevant forces on a particle in a membrane channel flow set-up [16]. The force from the undisturbed flow $\vec{F}_\mathrm{S}^o$ transports the particle along a streamline of the continuous phase [60]. Sphere drag $\vec{F}_\mathrm{D}$, virtual mass $\vec{F}_\mathrm{VM}$ and history forces $\vec{F}_\mathrm{H}$, which result from the disturbance flow, counteract this motion. However, because of their dependence on the relative acceleration of the particle with respect to the continuous phase, the virtual mass and history term are only significant in transient flow scenarios [16, 44].
The buoyant force $\vec{F}_\mathrm{B}$ and the gravitational force $\vec{F}_\mathrm{G}$ determine the effective settling velocity of the particle in a resting fluid. For neutrally buoyant particles, i.e. particles which exhibit the same density as the surrounding fluid, the gravitational force balances the buoyancy term and the particles do not settle. The other two body forces, namely the van der Waals force $\vec{F}_\mathrm{vdW}$ and the electrostatic double layer repulsion $\vec{F}_\mathrm{edl}$, gain significance if the particle approaches a channel wall, the membrane or another particle [35]. However, particle-particle interactions become negligible in very dilute particle flows, where the probability of particle-particle encounters is very small [19].
Lastly, inertial lift forces $\vec{F}_\mathrm{L}$ accelerate the particle perpendicular to the main flow direction. They do not appear in Maxey and Riley's derivation, because Maxey and Riley assume a no-slip boundary condition on the surface of the particle and a sufficiently small particle to avoid large velocity gradients between opposite sides of the particle. However, lift forces do become prominent for larger particles. When this is the case, they can simply be added to the Maxey

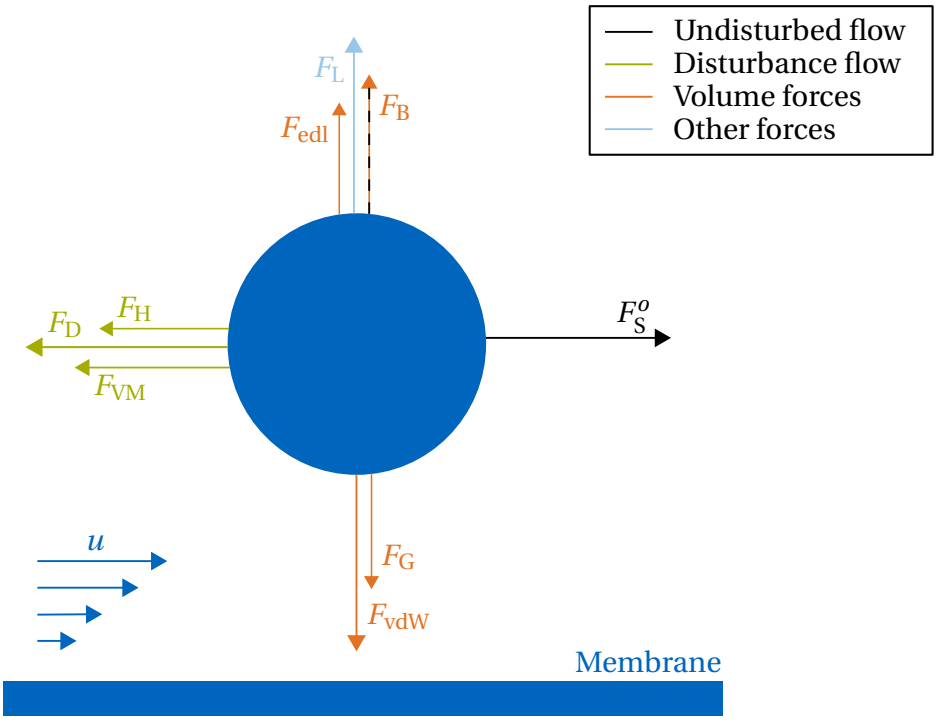

Figure 2.10: Relevant forces on a particle in a membrane channel flow set-up. Adapted from [16].

Riley equation, as they are linearly independent of the other terms. The most prominent lift force is the Saffman lift force, but the Magnus lift force, which is caused by the rotation of the particle, results in a similar behavior.

3 Implementation

The trajectories of the particles depend strongly on the flow conditions. Thus, the first step in the implementation of the particle transport is to resolve the flow in the channel. Adequate boundary conditions for the water and salt transport across the membrane must be defined to determine the flow characteristics close to the membrane (c.f. Section 2.1.2). In a second step, the particles are introduced to the system. Their trajectories are calculated considering the forces discussed in section 2.2 and the local salt concentrations, fluid density and viscosity from the previous step. The following chapter explains the numerical solution mechanism for the fluid conservation equations from section 2.1.1 and the momentum conservation of the particle. Furthermore, the setup of the simulations is discussed. All calculations are performed in the Open Source Fields Operation and Manipulation (OpenFOAM®) software version 6. More information about OpenFOAM® is provided in the Appendix.

3.1 Discretization - The Finite Volume Method

For numerical solutions in continuum mechanics, the fluid volume is divided into discrete cells. The entirety of the cells is referred to as the mesh of the problem. Analogously, the time is divided into discrete time steps. To numerically evaluate the flow variables at the centroid of each cell, the conservation equations of the flow problem (c.f. section 2.1.1) must be discretized, too [84].
The generalized integral form of the conservation equations is

$$\underbrace{\int_V \frac{\partial(\rho_\mathrm{F}\,\varphi)}{\partial t}\mathrm{d}V}_{\substack{\text{local temporal}\\ \text{change}}} + \underbrace{\int_V \nabla\cdot\left(\rho_\mathrm{F}\,\vec{u}\,\varphi\right)\mathrm{d}V}_{\text{convection}} = \underbrace{\int_V \nabla\cdot(\Gamma_\varphi\,\nabla\varphi)\mathrm{d}V}_{\text{diffusion}} + \underbrace{\int_V S_\varphi \mathrm{d}V}_{\text{source}}, \tag{3.1}$$

where $\varphi = \varphi(t,\vec{x})$ determines the conservation quantity. For $\varphi = 1$ equation 3.1 corresponds to the continuity equation. u_x, u_y, u_z are inserted to obtain momentum conservation equations in the respective directions and $\varphi = w_\mathrm{S}$[1] yields the salt conservation equation. Γ_φ is

[1]The salt conservation equation is solved in terms of the salt mass fraction instead of the concentration. The conversion between the salt mass fraction and the concentration is

$$w_\mathrm{S} = \frac{c_\mathrm{S}\overline{M}_\mathrm{S}}{\rho_\mathrm{F}}. \tag{3.2}$$

Thus, the salt conservation equation can be formulated in parallel to the other conservation equations

$$\nabla\cdot\left(\rho_\mathrm{F}\vec{u}\,w_\mathrm{S}\right) - \nabla\cdot\left(\rho_\mathrm{F}D_\mathrm{SW}\nabla w_\mathrm{S}\right) = 0, \tag{3.3}$$

as the molar mass of the salt $\overline{M}_\mathrm{S}$ is a constant.

Table 3.1: Discretization schemes for the governing equations of the fluid phase.

Mathematical term	Discretization scheme
$\frac{\partial}{\partial t}$	none (steady state)
∇	linear interpolation
$\nabla\cdot$	linear interpolation limited to upwind/ pure upwind
Δ	linear interpolation of the scalar, non-orthogonal correction for gradient component normal to cell face
Point-to-point interpolation	linear interpolation
Gradient component normal to cell face	corrected for non-orthogonalities

the diffusion coefficient which must correspond to the conservation quantity, i. e. the binary diffusion coefficient D_{SW} for salt conservation and the dynamic viscosity η_{F} for momentum conservation. S_φ is the source term of φ [84]. With the divergence theorem (Gauss theorem), the convection and the diffusion term become surface integrals

$$\int_V \frac{\partial(\rho_{\mathrm{F}}\,\varphi)}{\partial t}\mathrm{d}V + \int_S \rho_{\mathrm{F}}\,\varphi\;(\vec{u}\cdot\vec{n})\,\mathrm{d}S = \int_S \Gamma_\varphi\;\left(\nabla\varphi\cdot\vec{n}\right)\mathrm{d}S + \int_V S_\varphi \mathrm{d}V. \tag{3.4}$$

In a small control volume, such as one cell of a mesh, the variables are approximately constant on each surface of the control volume. Thus, the surface integrals can be transformed into sums over the surfaces of the control volume. Additionally, the values of the variables within the control volume are accounted for by a representative average over the cell. With these simplifications, equation 3.4 becomes [84]

$$\overline{\frac{\partial(\rho_{\mathrm{F}}\,\varphi)}{\partial t}}\;V + \sum_i \left(\rho_{\mathrm{F}}\,\varphi\right)_i (u_i S_i) = \sum_i \Gamma_{\varphi,i}\;(\nabla\varphi)_i S_i + \overline{S_\varphi}\;V. \tag{3.5}$$

Here, the flow variables are represented in terms of their average values within the control volume and on the surface of the control volume [84]. However, the goal of numerical computation is to determine their values at the centroid of the cells (also called nodes). Thus, the terms in equation 3.5 need to be expressed as functions of their respective cell center values. The local temporal change is equal to zero for steady state solutions and therefore not further considered in the following discussion. A summary of the discretization settings for all cases is provided in Table 3.1. The next steps in the discretization of the terms in equation 3.5 are discussed in the following sections.

3.1.1 Convection Term

For the cell in Figure 3.1 the convection term is

$$\begin{aligned}\textstyle\sum_i \left(\rho_{\mathrm{F}}\,\varphi\right)_i (u_i S_i) \;&=\; \rho_{\mathrm{F,e}} u_{x,\mathrm{e}} S_{\mathrm{e}} \varphi_{\mathrm{e}} - \rho_{\mathrm{F,w}} u_{x,\mathrm{w}} S_{\mathrm{w}} \varphi_{\mathrm{w}} \\ &+\; \rho_{\mathrm{F,n}} u_{y,\mathrm{n}} S_{\mathrm{n}} \varphi_{\mathrm{n}} - \rho_{\mathrm{F,s}} u_{y,\mathrm{s}} S_{\mathrm{s}} \varphi_{\mathrm{s}}\end{aligned} \tag{3.6}$$

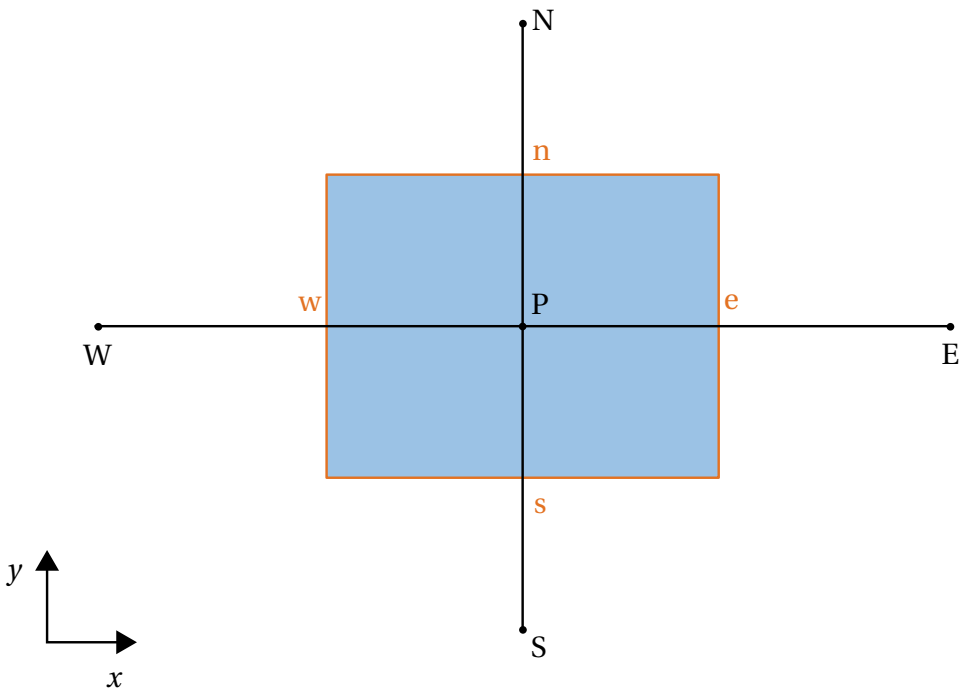

Figure 3.1: Exemplary mesh cell with compass notation convention. Adapted from [84].

The indices specify the position at which the variable is evaluated. Small letters indicate cell surface values and capital letters stand for the value of the variable at the node. Through interpolation or similar rules, the variables in equation 3.6 are expressed in terms of the node values. The upwind scheme, which is applied in our simulations for the discretization of the convection term in the momentum conservation equation, approximates the flow variable at the cell surface with the center value of the nearest upstream cell [59]

$$\varphi_\mathrm{e} = \begin{cases} \varphi_\mathrm{E} \text{ if } u_{x,\mathrm{e}} < 0 \\ \varphi_\mathrm{P} \text{ if } u_{x,\mathrm{e}} > 0 \end{cases} \qquad \varphi_\mathrm{w} = \begin{cases} \varphi_\mathrm{P} \text{ if } u_{x,\mathrm{w}} < 0 \\ \varphi_\mathrm{W} \text{ if } u_{x,\mathrm{w}} > 0 \end{cases}$$
$$\varphi_\mathrm{n} = \begin{cases} \varphi_\mathrm{N} \text{ if } u_{y,\mathrm{n}} < 0 \\ \varphi_\mathrm{P} \text{ if } u_{y,\mathrm{n}} > 0 \end{cases} \qquad \varphi_\mathrm{s} = \begin{cases} \varphi_\mathrm{P} \text{ if } u_{y,\mathrm{s}} < 0 \\ \varphi_\mathrm{S} \text{ if } u_{y,\mathrm{s}} > 0 \end{cases} \tag{3.7}$$

Similarly, the density and the transport velocity at the surface of the cell is equivalent to that of the upstream node. Hence, the discretization depends on the flow characteristics of the problem. With the relationships in equations 3.7, the convection term (equation 3.6) is expressed as a function of cell centroid values and the cell geometry. The advantage of upwind discretization over interpolation between the nodes of the mesh, is its robustness. On the other hand, the scheme is also prone to numerical diffusion, a common discretization error [84].
A (mostly) linear interpolation scheme is chosen for the convection term in the salt conservation equation, as the stability of the solver allows for a more precise but less robust discretization scheme here. Through linear interpolation of the centroid values to determine the values

of the flow variables at the surface of the cell, equation 3.6 becomes a function of node values

$$\begin{aligned}\sum_i \left(\rho_{\mathrm{F}}\,\varphi\right)_i (u_i S_i) &= \tfrac{1}{2}\left(\left(\rho_{\mathrm{F,E}} u_{x,\mathrm{E}}\varphi_{\mathrm{E}} + \rho_{\mathrm{F,P}} u_{x,\mathrm{P}}\varphi_{\mathrm{P}}\right) S_{\mathrm{e}}\right.\\ &- \left(\rho_{\mathrm{F,P}} u_{x,\mathrm{P}}\varphi_{\mathrm{P}} + \rho_{\mathrm{F,W}} u_{x,\mathrm{W}}\varphi_{\mathrm{W}}\right) S_{\mathrm{w}}\\ &+ \left(\rho_{\mathrm{F,N}} u_{y,\mathrm{N}}\varphi_{\mathrm{N}} + \rho_{\mathrm{F,P}} u_{y,P}\varphi_{P}\right) S_{\mathrm{n}}\\ &- \left.\left(\rho_{\mathrm{F,P}} u_{y,\mathrm{P}}\varphi_{\mathrm{P}} + \rho_{\mathrm{F,S}} u_{y,\mathrm{S}}\varphi_{\mathrm{S}}\right) S_{\mathrm{s}}\right).\end{aligned} \tag{3.8}$$

For the convection term in the salt conservation equation we apply a discretization scheme, which strictly limits the linear scheme towards the upwind scheme in regions where the gradient of the flow variable changes strongly. In the forward osmosis channels, this is particularly important close to the membrane where we observe large concentration gradients. In the other regions the cell surface values are calculated through linear interpolation.

3.1.2 Diffusion Term

In compass notation (Figure 3.1), the diffusion term in equation 3.5 is

$$\sum_i \Gamma_{\varphi,i}\,(\nabla\varphi)_i S_i = \Gamma_{\varphi,\mathrm{e}}\left(\frac{\partial\varphi}{\partial x}\right)_{\mathrm{e}} S_{\mathrm{e}} - \Gamma_{\varphi,\mathrm{w}}\left(\frac{\partial\varphi}{\partial x}\right)_{\mathrm{w}} S_{\mathrm{w}} + \Gamma_{\varphi,\mathrm{n}}\left(\frac{\partial\varphi}{\partial y}\right)_{\mathrm{n}} S_{\mathrm{n}} - \Gamma_{\varphi,\mathrm{s}}\left(\frac{\partial\varphi}{\partial y}\right)_{\mathrm{s}} S_{\mathrm{s}}. \tag{3.9}$$

Here, linear interpolation between the centroid values is chosen to determine the value of the diffusion coefficient at the surface of the cell. The surface normal gradient is calculated through a central difference, which is corrected for the non-orthogonality of the cell. With these specifications the diffusion term becomes [84]

$$\begin{aligned}\sum_i \Gamma_{\varphi,i}\,(\nabla\varphi)_i S_i &= \tfrac{1}{2}\left(\Gamma_{\varphi,\mathrm{E}} + \Gamma_{\varphi,\mathrm{P}}\right)\tfrac{\varphi_{\mathrm{E}}-\varphi_{\mathrm{P}}}{\Delta x_{\mathrm{e}}} S_{\mathrm{e}} - \tfrac{1}{2}\left(\Gamma_{\varphi,\mathrm{P}} + \Gamma_{\varphi,\mathrm{W}}\right)\tfrac{\varphi_{\mathrm{P}}-\varphi_{\mathrm{W}}}{\Delta x_{\mathrm{w}}} S_{\mathrm{w}}\\ &+ \tfrac{1}{2}\left(\Gamma_{\varphi,\mathrm{N}} + \Gamma_{\varphi,\mathrm{P}}\right)\tfrac{\varphi_{\mathrm{N}}-\varphi_{\mathrm{P}}}{\Delta y_{\mathrm{n}}} S_{\mathrm{n}} - \tfrac{1}{2}\left(\Gamma_{\varphi,\mathrm{P}} + \Gamma_{\varphi,\mathrm{S}}\right)\tfrac{\varphi_{\mathrm{P}}-\varphi_{\mathrm{S}}}{\Delta y_{\mathrm{s}}} S_{\mathrm{s}}.\end{aligned} \tag{3.10}$$

3.1.3 Source Term

The most important source term in the momentum equation is the pressure term. Other potential source terms, such as the generation of a species due to a chemical reaction or the loss of momentum as a result of friction, are zero in our flow problem. Therefore, the discretization of such source terms is not discussed here. Assuming that the cell faces on opposite sides of the cell are equal, linear interpolation of the centroid pressures to the cell faces yields [59]

$$\begin{aligned}\varphi = u_x: &\quad \frac{\partial p}{\partial x} = p_{\mathrm{e}} S_{\mathrm{e}} - p_{\mathrm{w}} S_{\mathrm{w}} = \left(\tfrac{1}{2}\left(p_{\mathrm{P}} + p_{\mathrm{E}}\right) - \tfrac{1}{2}\left(p_{\mathrm{W}} + p_{\mathrm{P}}\right)\right) S = \tfrac{1}{2}\left(p_{\mathrm{E}} - p_{\mathrm{W}}\right) S\\ \varphi = u_y: &\quad \frac{\partial p}{\partial y} = p_{\mathrm{n}} S_{\mathrm{n}} - p_{\mathrm{s}} S_{\mathrm{s}} = \left(\tfrac{1}{2}\left(p_{\mathrm{P}} + p_{\mathrm{N}}\right) - \tfrac{1}{2}\left(p_{\mathrm{S}} + p_{\mathrm{P}}\right)\right) S = \tfrac{1}{2}\left(p_{\mathrm{N}} - p_{\mathrm{S}}\right) S\end{aligned} \tag{3.11}$$

Inserting the expression for the pressure from equations 3.11 into the x-momentum conservation version of equation 3.5, one notes that the velocity at node P is independent of the pressure at the node

$$u_{x,\mathrm{P}} = \ldots + \frac{1}{2}\frac{S}{a_{\mathrm{P}}}(p_{\mathrm{W}} - p_{\mathrm{E}}). \tag{3.12}$$

Table 3.2: Solution settings for fluid phase equations.

Field variable	Matrix solver	Smoother	Tolerance
$\vec{u}$	smooth solver	Gauss-Seidel	10^{-7}
w_S	GAMG	Gauss-Seidel	10^{-10}
p	GAMG	Gauss-Seidel	10^{-7}

The factor a_P contains the geometric data of the mesh, the discretization scheme and the thermophysical properties of the fluid. To avoid this decoupling, the pressure is stored in a different grid than the velocity. The two grids are staggered in the control volume, such that the velocities are stored at the center of the velocity grid, which corresponds to the surface of the overlapping cell of the pressure grid. Other scalar variables are also stored at the nodes of the pressure grid. If the cells are non-orthogonal the velocity nodes might not lie between the corresponding pressure nodes. These shifts are corrected with so-called non-orthogonal correctors. For more information, the reader is referred to Polifke et al. [59].

3.2 Solvers

Solvers numerically evaluate the discretized conservation equations, which were derived in the previous section. This thesis applies two solvers to determine the flow profile in the channel and two solvers to calculate the particle trajectories. One of the solvers for the fluid flow and one of the solvers for the particle flow resolve the ideal case without concentration polarization. The other pair of solvers performs the same calculations for the non-ideal case which involves salt transport. In the following, the solution mechanisms of the solvers are explained. While the fluid solvers are provided by the OpenFOAM® library and an external package which was developed by Gruber et al. [30] specifically for desalination simulations, modifications are made to the OpenFOAM® original solver IcoUncoupledKinematicParcelFoam to obtain a detailed resolution of the particle forces and to account for the non-uniform thermophysical properties of the real flow. The flow diagrams of the solvers are depicted in Figure 3.2.
The solution algorithm of the solver determines the order in which the conservation equations are evaluated and how they are re-arranged to obtain individual equations for the flow variables. The resulting flow variable equations are solved in each iteration. The pressure and the salt mass fraction equations are solved with the geometric-algebraic multi-grid (GAMG) solver [65], which applies a solution on a coarse grid as an initial guess for the solution on a finer grid. The mesh is refined in each iteration until the mesh specified by the user is reached. The velocity equation is solved with a smooth solver. In this context, smooth refers to the elimination of the high-frequency errors of the solution. The most commonly applied smoother in OpenFOAM® is the Gauss-Seidel smoother [88]. Here, we use the same smoother for the solution of all three equations. The solution settings for the flow variable equations are summarized in Table 3.2. The overall solver terminates its iterative calculation of the flow variable when the convergence criterion of a residual smaller than 1×10^{-6} for all flow variables is reached.

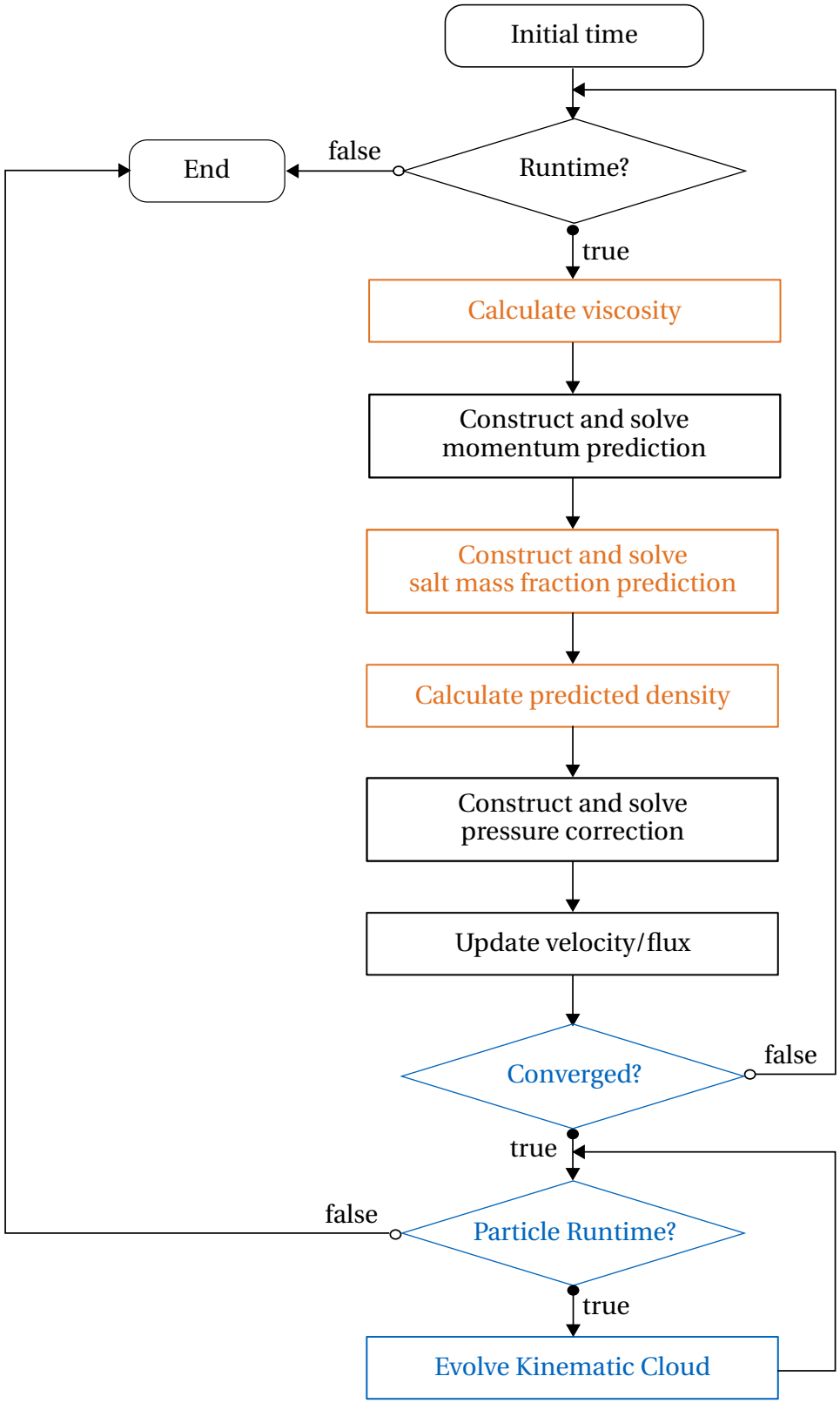

Figure 3.2: Flow diagram for the solvers in this thesis.

3.2.1 Solution Algorithm for the Ideal Channel Flow

The flow in the forward osmosis module which neglects the concentration polarization is calculated with the OpenFOAM® original solver simpleFoam. It applies the semi-implicit method for pressure-linked equations (SIMPLE) for the solution of incompressible, steady state problems. The SIMPLE algorithm decouples the momentum and continuity equations to separately solve for the pressure and the velocity components. Hence, the momentum equations serve as predictors for the velocity, while the continuity equation is transformed such that it maps the pressure. Based on the predicted velocity from the momentum equation, the continuity equation corrects the pressure and the velocity in the control volume. Therefore, velocity and pressure fields are evaluated in separate equations. Numerical methods which follow this approach are referred to as predictor-corrector or segregated methods [37].
The black elements in Figure 3.2 are included in the original simpleFoam solver. The prerequisites for the iterative solution of the conservation equations are (i) that the current run time is within the time limits and (ii) that the solution is not converged. If either of these prerequisites is not met, the time step is ended. Otherwise, the velocity field u^{p} of the time step is predicted by solving

$$a_{\mathrm{P}} u_{\mathrm{P}}^{\mathrm{p}} - \sum_{\mathrm{nb}} a_{\mathrm{nb}} u_{\mathrm{nb}}^{\mathrm{p}} = \frac{S}{\rho_{\mathrm{F}}} \left(p_{-1/2}^{\mathrm{n-1}} - p_{+1/2}^{\mathrm{n-1}} \right) \tag{3.13}$$

with a guessed pressure field p^{p} in the fist time step and the pressure field of the previous time step $p^{\mathrm{n-1}}$ in all subsequent iterations [59]. a_i contains the geometric data of the mesh, the discretization scheme and the thermophysical properties of the fluid. The index $_{\mathrm{nb}}$ refers to the neighboring nodes of node P. $_{-1/2}$ and $_{+1/2}$ indicate the values at the respective cell faces, e.g. $_{\mathrm{w}}$ and $_{\mathrm{e}}$ for u_x, $_{\mathrm{s}}$ and $_{\mathrm{n}}$ for u_y, etc. Note that equation 3.13 is obtained by inserting equations 3.6, 3.9 and 3.11 into the momentum form of equation 3.5. Thus, equation 3.13 is independent of the selected discretization scheme, but the a_i's contain the discretization information of the case.
In general, the predicted velocity field is not mass consistent. Therefore, the predicted velocity must be adapted to fulfill continuity (equation 3.5, $\varphi = 1$, incompressible, no sources) [59]

$$\sum_i u_i S_i = \sum_i u_i^{\mathrm{p}} S_i + \sum_i u_i^{\mathrm{c}} S_i = \dot{V}^{\mathrm{p}} + \sum_i u_i^{\mathrm{c}} S_i = 0. \tag{3.14}$$

Here, u_i^{c} is the correction to the velocity field and $\dot{V}^{\mathrm{c}}$ is the net volumetric flux from the predictor step. With the SIMPLE approximation [56]

$$u_{\mathrm{P}}^{\mathrm{c}} = \frac{\sum_{\mathrm{nb}} a_{\mathrm{nb}} u_{\mathrm{nb}}^{\mathrm{c}}}{a_{\mathrm{P}}} - \frac{S}{\rho_{\mathrm{F}} a_{\mathrm{P}}} \left(p_{+1/2}^{\mathrm{c}} - p_{-1/2}^{\mathrm{c}} \right) \approx - \frac{S}{\rho_{\mathrm{F}} a_{\mathrm{P}}} \left(p_{+1/2}^{\mathrm{c}} - p_{-1/2}^{\mathrm{c}} \right) \tag{3.15}$$

velocity changes u^{c} in the control volume are related to pressure changes p^{c}. In a converged solution of the coupled linear equations, the correction field approaches zero ($u^{\mathrm{c}} \to 0$ and $p^{\mathrm{c}} \to 0$), which justifies the simplification.[2] With equation 3.15, the continuity equation (equa-

[2] Alternatively, the SIMPLEC approximation can be chosen. Its key assumption is

$$\sum_{\mathrm{nb}} a_{\mathrm{nb}} u_{\mathrm{nb}}^{\mathrm{c}} \approx \sum_{\mathrm{nb}} a_{\mathrm{nb}} u_{\mathrm{P}}^{\mathrm{c}} = H_1 u_{\mathrm{P}}^{\mathrm{c}}, \tag{3.16}$$

tion 3.14) becomes the pressure correction equation [59]

$$\sum_i \left(\frac{\sum_{\mathrm{nb}} a_{\mathrm{nb}} u_{\mathrm{nb}}^{\mathrm{p}}}{a_{\mathrm{P}}} \right)_i S_i - \sum_i \left(\frac{S}{\rho_{\mathrm{F}} a_{\mathrm{P}}} \left(p_{+1/2}^{\mathrm{n}} - p_{-1/2}^{\mathrm{n}} \right) \right)_i S_i = 0, \tag{3.18}$$

which is solved for the pressure field of the current step

$$p^{\mathrm{n}} = p^{\mathrm{n-1}} + p\mathrm{c}. \tag{3.19}$$

Lastly, the velocity field is updated by applying the SIMPLE approximation (equation 3.15)

$$u_{\mathrm{P}}^{\mathrm{n}} = u_{\mathrm{P}}^{\mathrm{p}} + u_{\mathrm{P}}^{\mathrm{c}} = u_{\mathrm{P}}^{\mathrm{p}} - \frac{S}{\rho_{\mathrm{F}} a_{\mathrm{P}}} \left(p_{+1/2}^{\mathrm{c}} - p_{-1/2}^{\mathrm{c}} \right). \tag{3.20}$$

The SIMPLE algorithm assumes that all fluid properties are constant. Thus, the conservation equations are divided by the density and the pressure normalized by the fluid density is treated as one variable. In laminar flows, the density and viscosity are not explicitly calculated.

3.2.2 Solution Algorithm for the Real Channel Flow

The solver simpleSaltTransport [30] extends the solver for the ideal channel flow by the salt conservation equation. Fletcher et al. [25] formulated a weakly compressible model for salt transport in desalination channels, which is incorporated into the solver. In their approach, the salt mass fraction influences the density of the fluid, while the density remains independent of the local temperature and pressure. This simplification connects the additional mass conservation equation for the salt to the overall continuity equation and the momentum conservation equation. Furthermore, the mass and momentum equations are linked through the pressure (c.f. section 3.2.1). The orange elements of the flow diagram (Figure 3.2) correspond to the additional elements of the solver for the non-ideal channel flow.
Figure 3.3 illustrates the connection between the flow variables in the framework of the solver. First, the dynamic viscosity field is calculated based on the salt mass fraction from the previous step $w_{\mathrm{S}}^{\mathrm{n-1}}$ (or a guessed salt mass fraction $w_{\mathrm{S}}^{\mathrm{p}}$ in the first time step)

$$\eta_{\mathrm{F}} = \eta_{\mathrm{F}}^{0} \left(1 + C_{\eta}\, w_{\mathrm{S}}^{\mathrm{n-1}}\right). \tag{3.21}$$

$\eta_{\mathrm{F}}^{0} = 0.89 \times 10^{-3}\,\mathrm{Pa\,s}$ and $C_{\eta} = 1.62921$ are constants for the empirical relationship between the salt mass fraction and the viscosity [27], which is the diffusion coefficient Γ_{φ} for the momentum ($\varphi = u_i$). Together with the pressure and the flux from the previous step $(\rho_{\mathrm{F}} \vec{u})^{\mathrm{n-1}}$, the momentum predictor equation (equation 3.13) is solved. Contrary to the solver for the ideal case, the density and the pressure are explicitly treated as independent variables, while the velocity and the density are combined in the flux.

such that the velocity correction becomes

$$u_{\mathrm{P}}^{\mathrm{c}} = -\frac{S}{\rho_{\mathrm{F}} (a_{\mathrm{P}} - H_1)} \left(p_{+1/2}^{\mathrm{c}} - p_{-1/2}^{\mathrm{c}} \right). \tag{3.17}$$

In general, SIMPLEC converges faster than the pure SIMPLE algorithm.

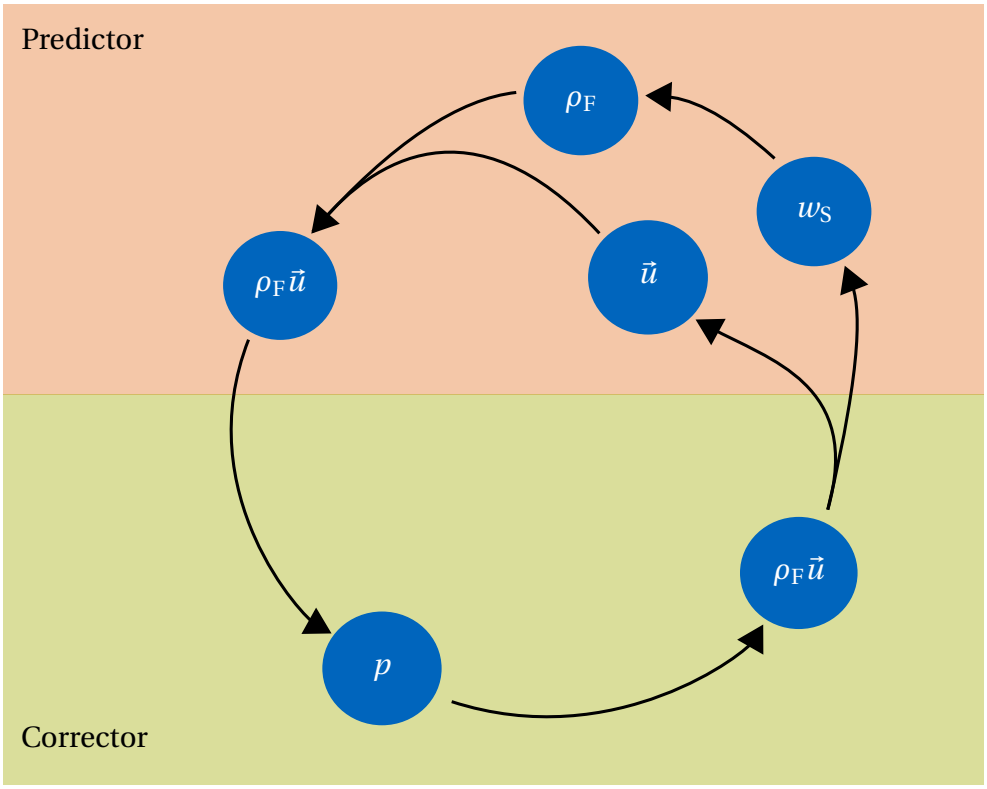

Figure 3.3: Algorithm of the concentration polarization solver.

The salt conservation equation (equation 3.5, $\varphi = w_S$, stationary, no sources) serves as a predictor for the density of the fluid. It is solved with the flux and the diffusion coefficient from the previous time step

$$D_{SW}^{n-1} = \max(D_{SW}^{0}\,(1 - C_{diff}\,w_S^{n-1}),\, D_{SW,min}). \tag{3.22}$$

$D_{SW}^{0} = 1.61 \times 10^{-9}\,m^2\,s^{-1}$, $C_{diff} = 14$ and $D_{SW,min} = 1.45 \times 10^{-9}\,m^2\,s^{-1}$ are the constants for the empirical relationship between the diffusion coefficient and the salt mass fraction [27]. The density is updated based on the salt mass fraction of the current time step w_S^n to yield the predicted density ρ_F^p

$$\rho_F^p = \rho_F^0(1 + C_\rho\,w_S^n). \tag{3.23}$$

Here, $\rho_F^0 = 997.1\,kg\,m^{-3}$ and $C_\rho = 1.44$ are the corresponding empirical constants [27]. The predicted density and the predicted velocity make up the predicted flux $(\rho\vec{u})^p$.
In the corrector step, the compressible continuity equation is solved for the current pressure

$$\sum_i \left(\frac{\sum_{nb} a_{nb}(\rho_F u_{nb})^p}{a_P} \right) S_i - \sum_i \left(\frac{S}{a_P} \left(p_{+1/2}^n - p_{-1/2}^n \right) \right)_i S_i = 0. \tag{3.24}$$

Finally, the flux is updated analogously to the velocity in the incompressible SIMPLE algorithm (equation 3.20)

$$(\rho_F u_P)^n = (\rho_F u_P)^p + (\rho_F u_P)^c = (\rho_F u_P)^p - \frac{S}{a_P} \left(p_{+1/2}^c - p_{-1/2}^c \right). \tag{3.25}$$

By combining the velocity and the density in the correction step, both variables are updated simultaneously. The parallel structures of the conservation equations for momentum and salt enables this numeric device.

3.2.3 Numerics of Particle Transport

The particle trajectories and deposition patterns are calculated after the fluid flow is resolved. The blue elements of the flow diagram (Figure 3.2) correspond to the steps in Lagrangian particle tracking. The modified solver myIcoUncoupledKinematicParcelFoam uses the same solution mechanism as the OpenFOAM® original solver IcoUncoupledKinematicParcelFoam, but incorporates an additional library which contains classes for newly coded particle forces and a class for writing out the effective forces on the particle at each time step. As the motion of particles also depends on the local density and viscosity of the fluid, the particle solver for the real forward osmosis channel myUncoupledKinematicParcelFoam furthermore constructs the density and velocity fields based on the salt mass fraction distribution determined by the fluid solver.
Both solvers apply the discrete parcel method (DPM) to follow a computational particle, i.e. a group of particles, which exhibit the same dynamic properties, through the flow field. If the number of particles in a parcel is set to 1, computational and physical particles are equivalent. In dilute flows, which are characterized by a particle volume fraction smaller than 0.1 %, the particle motion is dominated by particle-fluid interactions [19]. Thus, the streamline of a particle can be determined by numerically solving

$$m_{\mathrm{P}} \frac{\mathrm{d}\vec{V}}{\mathrm{d}t} = \vec{F}_{\mathrm{S}}^{o} + \vec{F}_{\mathrm{D}} + \vec{F}_{\mathrm{L}} + \vec{F}_{\mathrm{G}} + \vec{F}_{\mathrm{edl}} + \vec{F}_{\mathrm{vdW}} + \vec{F}_{\mathrm{Brown}} \tag{3.26}$$

for the particle velocity. $\vec{F}_{\mathrm{Brown}}$ is the Brownian motion force which accounts for the diffusive transport of the particle. The forces are calculated according to section 2.2. Note that the virtual mass force and the history term are omitted, because they are negligible in steady state fluid flows [44].
After the particles are introduced, the particle motion is calculated and the particle positions are updated based on the results. For the particle motion, the temporal derivative is not equal to zero. Therefore, an Euler discretization scheme [84] is chosen for the integration of equation 3.26.
In calculating the particle motion, OpenFOAM® distinguishes between coupled forces, that are exerted on the particle by the continuous phase, and non-coupled forces, which result from particle-particle interactions. For both types of forces, each force component is split into a term that depends on the relative velocity of the particle and a constant term

$$\vec{F} = S_{\mathrm{p}}(\vec{u} - \vec{V}) + \vec{S}_{\mathrm{u}}. \tag{3.27}$$

Dividing the resulting force equation by the effective mass of the particle (the virtual mass term can be included here) yields an acceleration, which depends on the relative velocity of the particle. By integrating this acceleration over the time step, the velocity difference of the particle $\Delta\vec{V}$ between the two discrete time points is calculated

$$\Delta\vec{V} = \Delta\vec{V}_{\mathrm{coupled}} + \Delta\vec{V}_{\mathrm{uncoupled}}. \tag{3.28}$$

Due to the distinction between coupled and non-coupled forces, it is possible to explicitly determine the momentum change of the particle resulting from the fluid forces. Momentum conservation states that the corresponding decrease in momentum in the continuous phase is equivalent to the increase in momentum of the particle. Thus, the velocity in the cell that contains the parcel can be updated accordingly. However, the influence of the particles on the fluid flow field is negligible if the particle mass loading of the flow is smaller than 0.2 [13]. Therefore, uncoupled solvers are chosen to determine the particle trajectories.
Lastly, the particle velocity is adjusted, such that

$$\vec{V}^{n} = \vec{V}^{n-1} + \Delta\vec{V} \tag{3.29}$$

and the position of the parcel is calculated by integrating its current velocity.

3.3 Implementation of Particle Forces

In the present model, the OpenFOAM ® original classes sphereDrag, pressureGradient, SaffmanMeiLift and gravity are included to account for the steady state drag force (equation 2.67), the force from the undisturbed flow (equation 2.65), the lift force (equation 2.86) and gravity (equation 2.54), respectively.
Equations 2.58 and 2.59 are implemented as the additional force classes GregoryWallAttraction and DoubleLayer to account for the membrane interaction of the particles. While the influence of the solute mass fraction on the Hamaker constant of the fluid and thus the Gregory wall attraction is negligible, the electrostatic double layer force depends strongly on the solute mass fraction [5]. Therefore, an additional force class DoubleLayerSalt is implemented to resolve the influence of the local salt concentration on double layer repulsion. All membrane interaction forces are included as non-coupled components of the overall force (c.f. equation 3.27).
Lastly, the class BrownianMotionLaminar is derived from the BrownianMotion class, which belongs to turbulence classes of the Lagrangian library. To include the Brownian motion force in the present model, the turbulence features are removed, such that only the diffusive transport of the particles in laminar flows is considered. While this diffusion is negligible for particles which are larger than 1 µm, it becomes increasingly important as the particle diameter decreases.

3.4 Boundary Conditions for the Membrane

In the concentration polarization cases, the water flux and reverse salt transport across the membrane are considered as boundary conditions for the velocity field and the salt mass fraction, respectively. For this purpose, the two boundary conditions MembraneUFvPatchVectorField and MembraneSaltFvPatchScalarField are implemented. The main functionality of the boundary conditions is to explicitly solve equations 2.33 and 2.38 for the water flux across the membrane and the salt concentration on the boundary patch and update the respective boundary fields. Thus, the concentration polarization in the channel can be resolved by combining the two boundary conditions with the solver for the salt transport.

3.4.1 Membrane Water Flux

The boundary condition for the water flux is a non-uniform Dirichlet boundary condition for the velocity, which is calculated iteratively. At each time step, the local salt mass fraction on the feed side of the membrane is read, while the salt mass fraction in the bulk of the draw channel is fixed. Based on the salt mass fractions, the osmotic pressures on both sides of the membrane are determined. The osmotic pressure depends linearly on the salt mass fraction if $w_S < 0.09$ [25, 80], such that

$$\Pi = \Pi^0 w_S. \tag{3.30}$$

The proportionality constant is $\Pi^0 = 805.1 \times 10^5$ Pa [27].
As the external concentration polarization on the feed side is calculated in the simulation, the salt concentration on the feed side of the active layer is known. The salt concentration on the draw side of the membrane is provided by equation 2.37. By assuming proportionality between the concentration and the osmotic pressure and inserting equation 2.37 in equation 2.33, we obtain an explicit formula for the water flux across the membrane

$$J_W = A\left(\exp\left(-\frac{J_W S}{D_{SW}}\right)\Pi''_b - \Pi'_m\right) + B\left(\exp\left(-\frac{J_W S}{D_{SW}}\right) - 1\right). \tag{3.31}$$

Ridder's method for root finding [62] is applied to solve equation 3.31 for the magnitude of the local water flux at each boundary cell surface of the feed channel. If the salt permeability of the membrane is very low, the second term of equation 3.31 is negligible. To determine the velocity vector which corresponds to the membrane water flux, a no-slip boundary condition is applied for the velocity components parallel to the membrane.

3.4.2 Membrane Salt Flux

Similar to the boundary condition for the water flux, boundary values and gradients of the salt mass fraction are calculated. The net salt flux in the boundary layer of the feed channel is given in equation 2.38. As the salt mass flux depends on both the gradient of the salt mass fraction and the salt mass fraction, the corresponding boundary condition is a mixed Dirichlet and von Neumann boundary condition [30]. Therefore, coefficients for the value of the salt mass faction and for its gradient need to be specified, such that

$$w_{S,m} = C_{i,v}\, w_{S,P} + C_{b,v} \tag{3.32}$$

and

$$\left.\frac{\partial w_S}{\partial z}\right|_m = C_{i,g}\, w_{S,P} + C_{b,g}. \tag{3.33}$$

The indices $_m$ and $_P$ denote the boundary value at the membrane and the node value of the adjacent cell. $C_{i,v}$ and $C_{b,v}$ are the value internal coefficient and the value boundary coefficient and $C_{i,g}$ and $C_{b,g}$ are the respective coefficients for the gradient.
Equation 2.38 contains the information to determine the four constants for the salt mass fraction. With the approximation

$$\frac{\partial w_S}{\partial z} \approx \frac{w_{S,m} - w_{S,P}}{\Delta z_{mP}}. \tag{3.34}$$

Equation 2.38 can be arranged to fit the scheme of equation 3.32

$$w_{\mathrm{S,m}} = \underbrace{\frac{1}{1+\frac{u_z}{D_{\mathrm{SW}}}\Delta z_{\mathrm{bP}}}}_{C_{\mathrm{i,v}}} w_{\mathrm{S,P}} + \underbrace{\frac{J_{\mathrm{S}}}{\frac{\rho_{\mathrm{F}} D_{\mathrm{SW}}}{\Delta z_{\mathrm{bP}}} + \rho_{\mathrm{F}} u_z}}_{C_{\mathrm{b,v}}}. \tag{3.35}$$

Inserting equation 3.35 into equation 2.38 yields the gradient coefficients of the von Neumann part of the salt mass fraction boundary condition

$$\left.\frac{\partial w_{\mathrm{S}}}{\partial z}\right|_{\mathrm{m}} = \underbrace{-\frac{1}{\frac{u_z}{D_{\mathrm{SW}}}+\Delta z_{\mathrm{bP}}}}_{C_{\mathrm{i,g}}} w_{\mathrm{S,P}} + \underbrace{\frac{J_{\mathrm{S}}}{\rho_{\mathrm{F}} D_{\mathrm{SW}} + \rho_{\mathrm{F}} u_z \Delta z_{\mathrm{bP}}}}_{C_{\mathrm{b,g}}}. \tag{3.36}$$

The diffusion coefficients and the densities are calculated with the boundary salt mass fraction from the previous time step according to equations 3.22 and 3.23.

3.5 Case Set-Up

The real geometry of the spacer-filled feed channel is approximated by a two-dimensional slice of the channel along the flow direction with circular recesses as spacer filaments (Figure 3.4) [40, 42]. The centers of the spacer filaments (diameter 0.55 mm) are alternatingly placed at z = 0.25 mm and z = 0.75 mm with 4 mm horizontal distance between the filaments. Thus, one repetitive unit of the feed channel is 8 mm long and 1 mm high. The flux is calculated in four consecutive spacer elements with an outflux of 10 mm to avoid channel exit effects [69]. The influx of the channel is not calculated, because a fully developed laminar flow profile is imposed on the inlet patch as a boundary condition. The particles are transported through all four elements.

3.5.1 Meshing

During the meshing process, the fluid volume is divided into cells that facilitate the numerical solution of the governing conservation equations. The meshes for this study are adapted from Kiefer [40] using OpenFOAM® utilities for automated mesh generation.
The basic meshed cuboid structure of the feed channel is generated with the blockMesh utility. One raw spacer element is made up of 427 cells in x-direction, 1 cell in y-direction and 107 cells in z-direction, which are evenly distributed along the axes. Additionally, the types of boundary faces, also called patches, are defined. The inlet and outlet patches of the feed and draw channel are such that different inlet and outlet conditions can be specified without having to create a new mesh. The type wall is chosen for the top patch of the channel. The bottom face, which corresponds to the membrane, is also specified to account for varying permeate flow rates. The front and back patches of the channel are empty, such that the mesh is two-dimensional.
The mesh is snapped around the surfaces of cylinders to introduce the spacers. Four consecutive spacer elements are cut out of the cuboid base structure in this manner and the newly

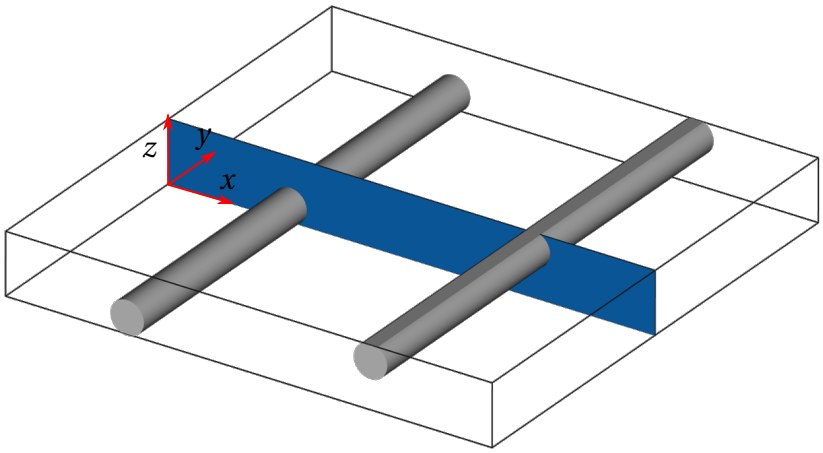

Figure 3.4: Simplified geometry of a spacer-filled forward osmosis channel. Adapted from [43].

created faces of the geometry are defined as wall patches. Additionally, the cells are gradually refined perpendicular to the surface of the spacer filaments, the membrane patch and the feed channel wall [40], such that the smallest cells adjacent to the respective patches are 0.5 µm to 1.8 µm high.
Throughout the manipulation of the original cuboid mesh, the cell boundaries are shifted, and non-orthogonal cells are created. However, two-dimensional geometries require that the nodes on the two faces, whose surface normal points in the direction of the unresolved dimension, lie on top of each other. Thus, in a last step in the mesh generation, the nodes of the front patch are projected onto the back patch and the cell faces are re-aligned parallel to the y-axis. The flow diagram for meshing is depicted in Figure 3.5.

3.5.2 Grid Convergence

The discretization of the geometry gives rise to a deviation of the numerical solution from the continuous solution. This error asymptotically decreases as the cell size approaches zero. A grid convergence study was conducted to ensure that the numerical solution is independent of the mesh, i.e. to determine whether the number of cells in the grid is sufficient to obtain a solution in the asymptotic error range. The following equations and concepts summarize Roache's [63] strategy to estimate grid convergence.
A very fine, a fine, a medium and a coarse mesh with equal refinement ratios are generated following the meshing strategy described in section 3.5.1. The block mesh of one spacer element of the coarse mesh consists of 240 × 60 cells, the medium mesh is made up of 321 cells in x-direction and 80 cells in z-direction, and the very fine mesh consists of 569 × 143 cells. The refinement ratio ϱ depends on the total number of cells of the two meshes $N_{\text{very fine}}$ and

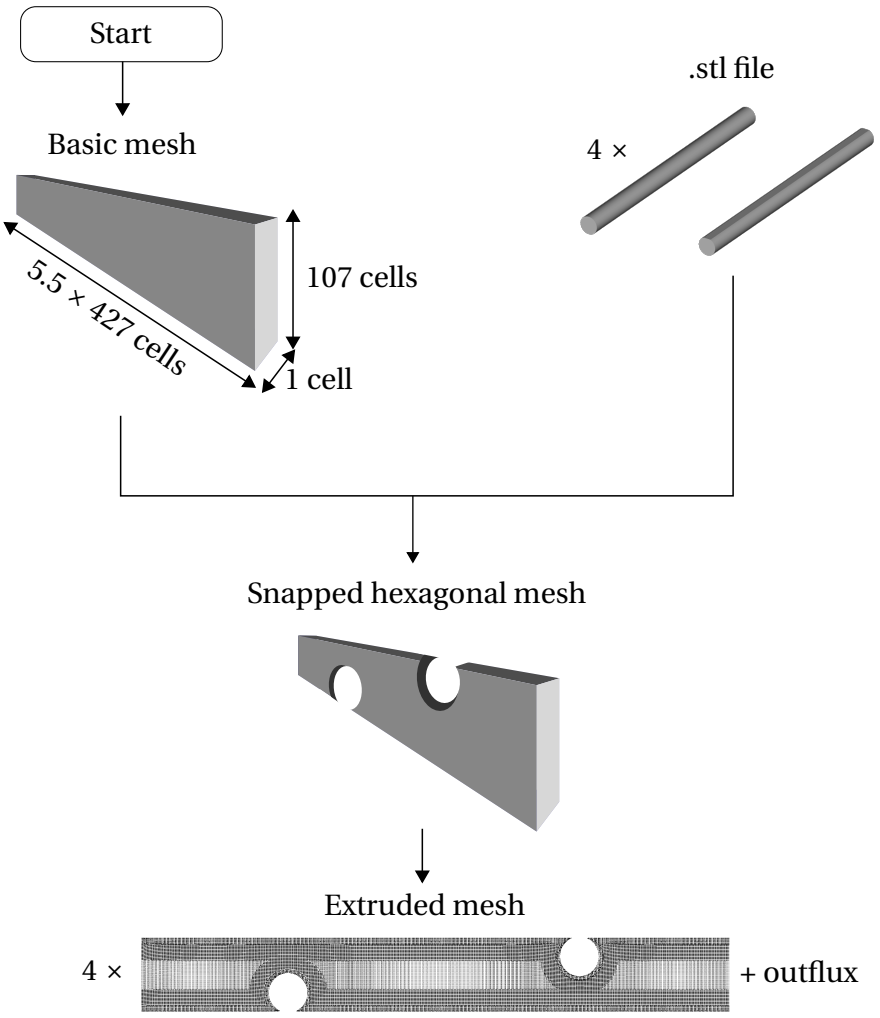

Figure 3.5: Flow diagram of the meshing procedure.

N_{fine} (N_{fine} and N_{medium}, N_{medium} and N_{coarse}), as well as on the dimensionality D of the grid

$$\varrho = \sqrt[D]{\frac{N_{\text{very fine}}}{N_{\text{fine}}}} = \sqrt[D]{\frac{N_{\text{fine}}}{N_{\text{medium}}}} = \sqrt[D]{\frac{N_{\text{medium}}}{N_{\text{coarse}}}}. \tag{3.37}$$

The order of convergence p is

$$p = \frac{\ln \frac{f_{\text{coarse}} - f_{\text{medium}}}{f_{\text{medium}} - f_{\text{fine}}}}{\ln \varrho}. \tag{3.38}$$

As we are interested in determining the hydrodynamic properties of the flow in the channel, the average velocity at the first filament of the third spacer element and the average salt fraction at the feed side of the membrane in the third spacer element were chosen as characteristic measures f of the problem.

With the refinement ratio and the order of convergence, the grid convergence index GCI becomes

$$\mathrm{GCI}_{\text{very fine}} = \frac{C_\mathrm{s}\left|\frac{f_{\text{fine}}-f_{\text{very fine}}}{f_{\text{very fine}}}\right|}{\varrho^p - 1}, \tag{3.39}$$

$$\mathrm{GCI}_{\text{fine}} = \frac{C_\mathrm{s}\left|\frac{f_{\text{medium}}-f_{\text{fine}}}{f_{\text{fine}}}\right|}{\varrho^p - 1} \tag{3.40}$$

and

$$\mathrm{GCI}_{\text{medium}} = \frac{C_\mathrm{s}\left|\frac{f_{\text{coarse}}-f_{\text{medium}}}{f_{\text{medium}}}\right|}{\varrho^p - 1} \tag{3.41}$$

for the very fine, the fine and the medium mesh, respectively. $C_\mathrm{s} = 3$ is a safety factor. The grid convergence index of the coarse mesh is

$$\mathrm{GCI}_{\text{coarse}} = \varrho^p\, \mathrm{GCI}_{\text{medium}}. \tag{3.42}$$

If the grid has converged, the $\mathrm{GCI}_{\text{very fine}}$ and $\mathrm{GCI}_{\text{fine}}$ are in the asymptotic range when plotting the grid convergence index over the cell number of the mesh. The results of the grid convergence study are depicted in Figure A.1.

3.5.3 Flow Field Boundary Conditions

Boundary conditions constrain the solutions of differential equations such as the ones encountered in the present transport model. The boundary conditions on the front and back of the channel are set to empty for all flow variables (c.f. section 3.5.1).

Pressure

The pressure gradient at the inlet patches, the walls, the spacers and the membrane is set to zero. This corresponds to a von Neumann boundary condition. The error which is induced by the zero gradient inlet boundary condition is negligible, because this study only examines the steady state [30]. A Dirichlet boundary condition in the form of a uniform gauge pressure of 0 Pa is specified at the outlet patches. This simplification is possible, because the pressure does not influence the fluid density in our simulations [30]. The initial internal pressure field is 0 Pa.

Velocity

A no-slip velocity boundary condition is set on the wall and the spacer filaments of the channel. On the outlet patches, the gradient of the velocity is zero. The inlet and permeate velocities of the feed channel are set to match the respective Reynolds numbers in experiments reported by Bogler et al. [10]. The crossflow Reynolds number Re is

$$\mathrm{Re} = \frac{\rho_\mathrm{F}\, d_\mathrm{h}\, u_\mathrm{c}}{\eta_\mathrm{F}}, \tag{3.43}$$

Table 3.3: Crossflow and permeate velocities for the simulations.

	Crossflow (C)	Permeate water flux (P)
High (H)	$42.70 \times 10^{-3}\,\mathrm{m\,s^{-1}}$	$2.78 \times 10^{-6}\,\mathrm{m\,s^{-1}}$
Medium (M)	$20.00 \times 10^{-3}\,\mathrm{m\,s^{-1}}$	$8.00 \times 10^{-7}\,\mathrm{m\,s^{-1}}$
Low (L)	$3.34 \times 10^{-3}\,\mathrm{m\,s^{-1}}$	$5.56 \times 10^{-7}\,\mathrm{m\,s^{-1}}$

where u_c is the average x-component of the crossflow velocity and d_h represents the hydraulic diameter of the channel

$$d_\mathrm{h} = \frac{4\epsilon}{\frac{2}{H} + (1-\epsilon)S_\mathrm{sp,sp}}. \tag{3.44}$$

Here, H is the channel height and $S_\mathrm{sp,sp}$ is the specific surface area of the spacer. The porosity ϵ of the channel is

$$\epsilon = 1 - \frac{V_\mathrm{sp}}{V_\mathrm{ch}} \tag{3.45}$$

with the volume of the spacers V_sp and the volume of the entire channel V_ch [68].
Therefore, the average crossflow velocity in the simulation $u_\mathrm{c,sim}$ is

$$u_\mathrm{c,sim} = \frac{d_\mathrm{h,exp}}{d_\mathrm{h,sim}} u_\mathrm{c,exp}. \tag{3.46}$$

The indices $_\mathrm{exp}$ and $_\mathrm{sim}$ correspond to the experimental value and the value in the simulation, respectively. The resulting crossflow velocities in the simulation are summarized in Table 3.3. Additionally, an intermediate crossflow velocity is investigated.
The crossflow velocity profile on the inlet patch of the feed channel is the Hagen-Poiseuille profile of a fully developed laminar flow

$$u_\mathrm{c}(z) = u_\mathrm{c,max}\left(1 - \frac{\zeta^2}{(H/2)^2}\right). \tag{3.47}$$

$u_\mathrm{c,max} = 3/2\,u_\mathrm{c,sim}$ is the maximum x-component of the crossflow velocity and $\zeta = \sqrt{(z-(H/2))^2}$ is the distance from the center of the channel.
Similar to the crossflow Reynolds number, the permeate Reynolds number $\mathrm{Re_w}$ [16]

$$\mathrm{Re_w} = \frac{\rho_\mathrm{F} d_\mathrm{h} u_\mathrm{w}}{\eta_\mathrm{F}} \tag{3.48}$$

provides the link between the z-component of the permeate velocities u_w of the experiment and the simulations. The permeate velocities for the simulation are summarized in Table 3.3. Additional calculations were performed for an intermediate permeate velocity. In the ideal cases, the permeate water fluxes are a fixed value boundary condition of (0 0 u_w) on the membrane wall.
In the concentration polarization cases, the membrane velocity boundary condition is specified by the membrane parameters water transport coefficient A = $7.1139 \times 10^{-12}\,\mathrm{m\,s^{-1}\,Pa}$, the salt transport coefficient B = $1.7383 \times 10^{-8}\,\mathrm{m\,s^{-1}}$ and the structural parameter of the porous

Table 3.4: Mass transport coefficients and resulting bulk salt mass fractions.

		$\beta \times 10^{-6}\,\mathrm{m\,s^{-1}}$	$w''_{\mathrm{S,b}} \times 10^{-3}$
HC	HP	20.47	7.4
	MP		1.6
	LP		1.1
MC	HP	15.58	7.4
	MP		1.6
	LP		1.1
LC	HP	8.18	7.4
	MP		1.6
	LP		1.1

support layer S = 215 µm. The values are chosen to fit the parameters of the membrane which was used in Bogler et al.'s experiments [10]. With equation 2.41, we estimate the salt mass fraction in the bulk of the draw channel which is necessary to obtain a certain water flux. The mass transfer coefficient in the boundary layer of the feed is calculated from the Sherwood number Sh of the spacer-filled channel [8]

$$\mathrm{Sh} = \frac{\beta d_{\mathrm{h}}}{D_{\mathrm{SW}}} = 0.46(\mathrm{Re}\,\mathrm{Sc})^{0.36}. \tag{3.49}$$

The Schmidt number Sc

$$\mathrm{Sc} = \frac{\eta_{\mathrm{F}}}{\rho_{\mathrm{F}} D_{\mathrm{SW}}} \tag{3.50}$$

relates the viscous diffusion to the molecular diffusion. Table 3.4 summarizes the so-obtained mass transfer coefficients and salt mass fractions in the draw channel.

Salt Mass Fraction

The salt mass fraction boundaries are only specified in the concentration polarization cases. At the outlet, the walls and the spacers, the gradient of the salt mass fraction is zero. The inlet salt mass fraction of the feed channel is set to $4.70 \times 10^{-7}\,\mathrm{kg\,kg^{-1}} = 8\,\mathrm{mmol\,dm^{-3}}$ [10].

3.5.4 Particles

Lastly, the particle properties are specified. The density of the particles is set to $1055\,\mathrm{kg\,m^{-3}}$, such that the particles are approximately neutrally buoyant. This corresponds to the material constant of the carboxylated polystyrene beads, which were used in Bogler et al.'s experiments [10].
Two different injection models are selected for tracking the streamlines of the particles and for the deposition studies. Injection models specify both the location of the particle injection and the size distribution of the particle cloud. The manual injection model allows for releasing the particles at fixed positions throughout the geometry, which is advantageous for determining

the particle tracks. In particular, nine particles are evenly distributed over the feed channel height at $x = 0\,\text{mm}$ and released simultaneously at the start of the simulation. All particles exhibit a diameter of $3\,\mu\text{m}$. For the deposition studies, particles are injected statistically distributed over the inlet patch. A Rosin-Rammler size distribution is chosen to also simulate abberated and agglomerated particles, which deviate from the ideal fixed particle diameter. The average particle diameter is set to $3\,\mu\text{m}$, the minimum diameter is $0.5\,\mu\text{m}$ and the maximum diameter is $5.5\,\mu\text{m}$ (Figure A.7).
Lastly, we specify that the particles rebound from the front and back patches of the geometry. As these patches are not real boundaries of the problem but only serve the purpose of decreasing the required computational power, the particles remain in the computational domain when they come in contact with these patches. The particles are allowed to escape the geometry through the inlet and outlet patches. When a particle is transported out of the channel, it is removed from the computational domain and not considered in the subsequent time steps. The wall and membrane interaction of the particle is best represented by the stick boundary condition, which implies that the particle remains in the computational domain but is irreversibly bound to the boundary patch.

4 Results and Discussion

After the validation of the newly implemented boundary conditions and particle transport model, the flow characteristics in the forward osmosis channel with and without concentration polarization are resolved. The particle trajectories for three channel Reynolds numbers and three permeate water fluxes for both the ideal and the real case are calculated and compared to other particle transport models and experimental data. Lastly, deposition studies for selected flow conditions are conducted.

4.1 Validation of the Membrane Transport

The transmembrane water flux is compared to the water flux which was experimentally determined by Bogler et al. [10]. At a draw salt mass fraction of 0.0568 $\mathrm{kg\,kg^{-1}}$ and the high Reynolds number (Re = 82.5) in the feed channel, the permeate water flux determined by the simulation is 33.4 $\mathrm{L\,m^{-2}\,h^{-1}}$. Under the same conditions, the experimental permeate water flux is 30 $\pm$ 4.6 $\mathrm{L\,m^{-2}\,h^{-1}}$. Thus, our concentration polarization simulations agree with the experimental data. This does not only confirm the membrane transport model, but also validates the approximation of the three-dimensional spacer channel with the two-dimensional zig-zag geometry.

4.2 Validation of the Particle Model

To validate the particle transport model, the particle trajectories are compared to the trajectories determined by Chellam et al. [16] for a simple Poiseuille flow channel with a permeable wall (Figure 4.1). Their semi-analytical ordinary differential equation for the location of a particle as a function of time considers hydrodynamic and volume forces including colloidal forces that describe the wall interaction. Empirical equations are applied to determine hydrodynamic forces as a function of lateral distance from the permeable wall and axial location in the channel.[1] The permeate flow rate ($u_\mathrm{w} = |u_z(z=0)| = 1.9 \times 10^{-4}\,\mathrm{m\,s^{-1}}$) is constant over the length of the channel. Under the geometric boundaries given by [16], the volume flux of permeate is not negligible compared to the channel flow, such that the velocity profile displayed in Figure 4.1b is established.
To keep the volume flux and thus the velocity profile constant over the length of the channel, the boundary condition for the fluid velocity on the top channel wall was set to make up for the volume loss through the permeable bottom wall ($u(z=0) = u(z=H)$; Figure 4.1a). These

[1] The main flow direction is the x-direction of the geometry and the channel extends laterally in z-direction. The y-direction is not resolved.

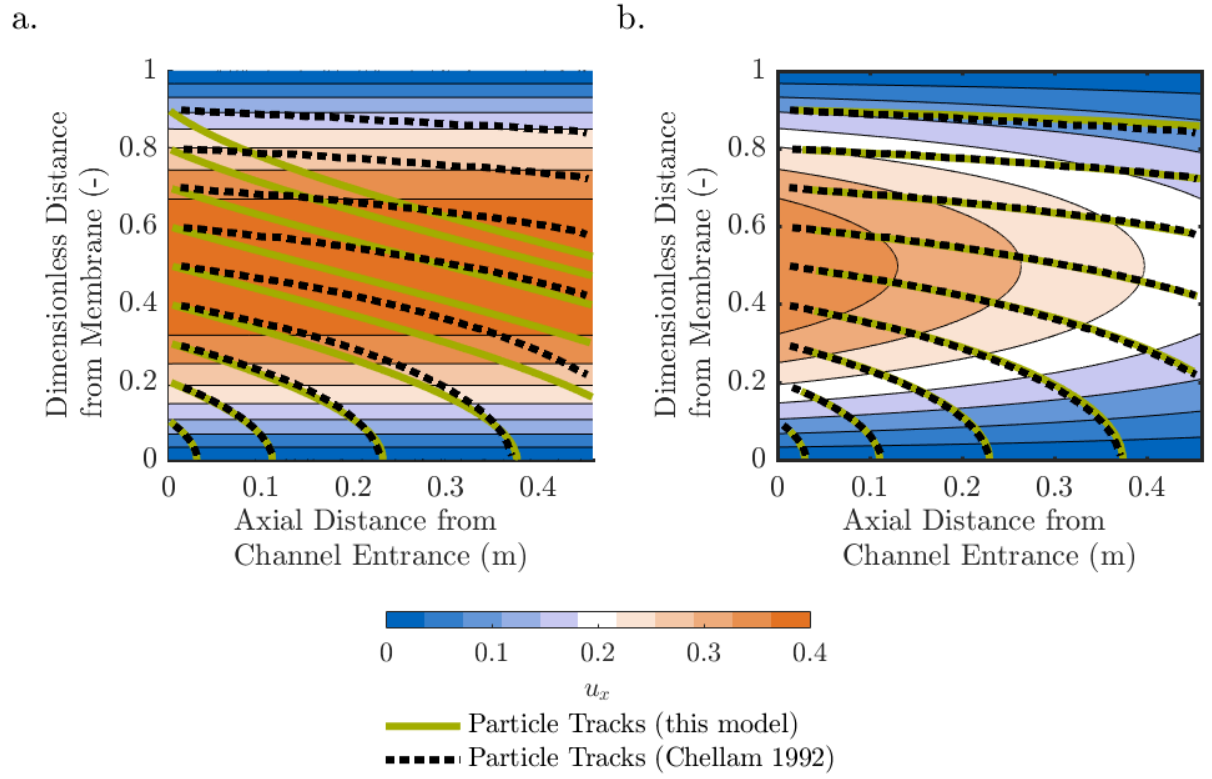

Figure 4.1: Comparison of the particle trajectories calculated by Chellam et al. [16] with the particle trajectories evaluated with the present model for a uniform permeate velocity through a. the bottom and top wall and b. only the bottom wall with a no-slip boundary condition on the top wall.

boundary conditions ensure that continuity is fulfilled when evaluating periodic flow models, such as suggested in previous CFD studies of spacer-filled channels [40, 60].
The particles are introduced to the fully developed flow. For inlet positions in the bottom half of the channel, Figure 4.1a shows very good agreement between the particle trajectories determined through our CFD calculations and the semi-analytical differential equation presented in [16]. However, the trajectories of the particles, which were initialized in the top half of the channel, strongly deviate toward lower positions compared to the trajectories calculated by Chellam et al. [16]. The fixed velocity boundary condition on the top wall introduces a uniform lateral fluid velocity throughout the channel. As a no-slip boundary condition on the top wall represents the flow conditions in the channel more accurately, the simplification $u(z = 0) = u(z = H)$ overestimates the lateral fluid velocity in the top half of the channel. Hence, the drag force on the particles in the upper half of the channel is larger than their acceleration due to lateral hydrodynamic drag in a channel with an impermeable upper wall.
When applying a no-slip boundary condition to the top wall, the particle trajectories calculated with this model are in excellent agreement with the previously reported trajectories [16]. Even in simple channel flow geometries, the lateral velocity is not uniform throughout the

channel, but increases towards the permeable surface [12]. An approximation of the lateral fluid velocity through identical boundary conditions on the top and bottom wall, which is a prerequisite for using periodic flow conditions to determine the flow in the channel, produces a significant error. Thus, Radu et al. [60] performed their calculations with four consecutive spacer elements and considered the third element representative for any spacer element sufficiently far from the influx and outflux of the flow cell. Li et al. [43] studied particle trajectories over three repetitive spacer units with a permeable membrane on the top and bottom of the channel. To ensure that the flow is fully developed and to avoid effects of the spacer eddies on the channel exit, the entrance and exit distances of the channel are 10 and 20 times the spacer filament diameter, respectively.
An additional evaluation case was set up to determine whether this model also correctly calculates the particle trajectories of larger particles. However, our results for the lift force dominated transport of larger particles differ significantly from the trajectories which were determined by Chellam et al. [16] for particles with a diameter of 26 µm (Figure A.2). While the particles in our model still experience a significant permeation drag that pulls them towards the membrane, the literature results suggest that such particles tend towards their equilibrium distance from the channel wall [16]. In the present model we do not resolve the spin of the particles resulting from the velocity gradient across the particle. In contrast, Chellam et al. [16] incorporated empirical relationships for the lift force of freely rotating particles. Thus, they inherently considered the Magnus lift force in addition to the Saffman lift force, whereas the present model only includes the Saffman lift force. While this simplification holds well for the 7 µm particles, it becomes inaccurate for larger particles. Therefore, the present model is restricted to small particles in the permeation drag dominated regime.

4.3 Characterization of the Channel Flow

In the trade-off between computational capacity and accurate reproduction of the fluid mechanics in a forward osmosis module, the particle flow is first evaluated in four consecutive, two-dimensional zig-zag spacer elements with a constant permeate flow rate at the bottom wall ($u_w \neq f(x)$). Figure 4.2 displays exemplary flow conditions in the third spacer element of such a channel for three different crossflow velocities. The velocity at $x = 0$ mm adopts the characteristic parabolic Hagen-Poiseuille profile of laminar channel flows (data not shown). In proximity to the spacer, the flow accelerates as the cross-sectional area of the channel is reduced. Stagnation zones ($u_x \approx 0\,\mathrm{m\,s^{-1}}$) develop up- and downstream of the spacer. Their dilation adjusts to the crossflow velocity in the channel (Figure 4.2). As the crossflow volume stream increases, the length of the stagnation zone before the filament decreases while the stagnation area behind the spacer is extended [2]. Thus, the flow profile imposed by the upstream filament directly transitions into the flow distortion induced by the next filament. However, if the crossflow is sufficiently slow, the axial velocity component resumes a Hagen-Poiseuille profile between the spacer filaments. This is the case for the lowest crossflow velocity.
In two-dimensional simulations of laminar channel flows with a permeable wall, the lateral component of the fluid velocity is commonly treated independently of the main channel flow [16,74]. However, in the present case, the channel flow itself exhibits a lateral component,

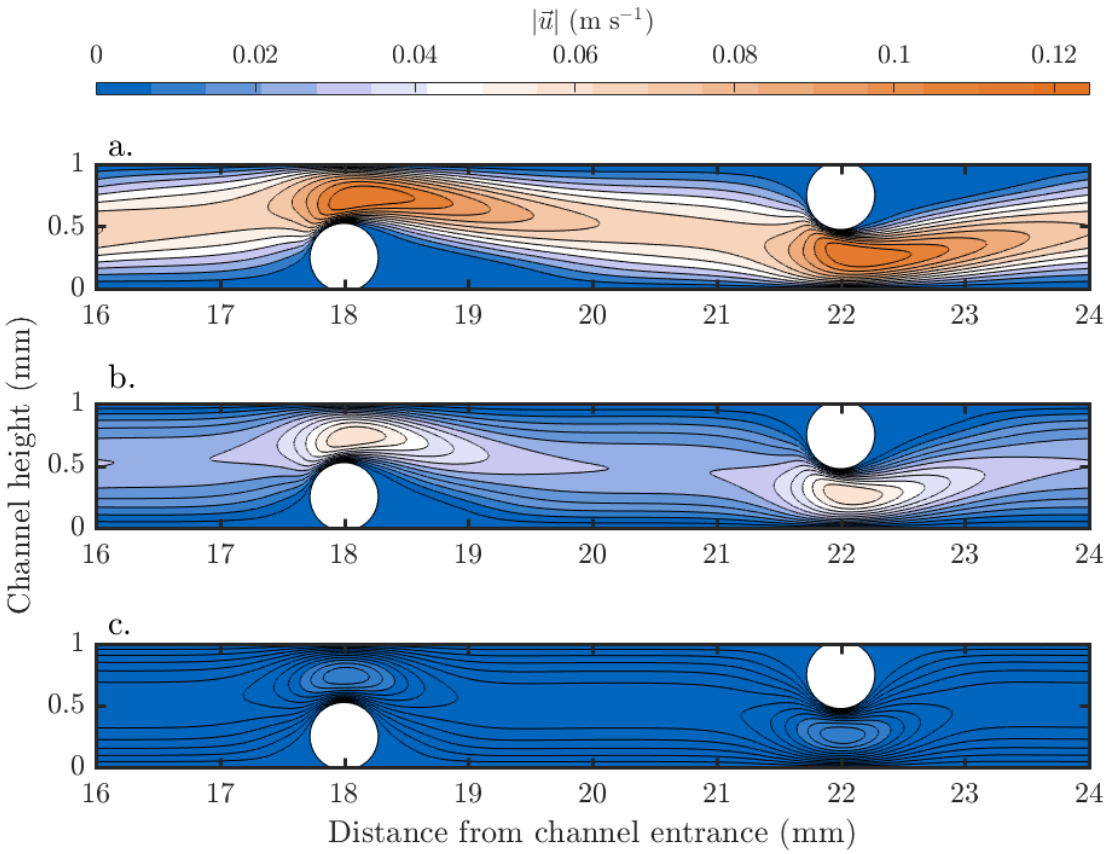

Figure 4.2: Characteristic flow profiles in a channel with zig-zag spacer configuration. The average crossflow velocity at the inlet is a. $42.70 \times 10^{-3}\,\mathrm{m\,s^{-1}}$ (HC), b. $20.00 \times 10^{-3}\,\mathrm{m\,s^{-1}}$ (MC) and c. $3.34 \times 10^{-3}\,\mathrm{m\,s^{-1}}$ (LC) and the permeate water flux of $2.78 \times 10^{-6}\,\mathrm{m\,s^{-1}}$ (HP) is constant over the length of the channel.

which superimposes the lateral fluid velocity induced by the membrane flow. At low permeate flow rates, which are characteristic for forward osmosis modules [45], the lateral acceleration from the spacers is three to four orders of magnitude larger than the flow rate through the membrane. Hence, the crossflow velocity influences the overall fluid velocity perpendicular to the membrane more than the permeation rate. In proximity to the membrane, the crossflow velocity approaches zero, such that the permeate water flux governs the hydrodynamics of the channel flow.

As a constant volume stream permeates through the bottom wall, the crossflow volume stream decreases approximately linearly with the channel length. This loss accounts for less than 0.05% of the feed flux in the high crossflow-low permeate set-up and for up to 2.67% of the feed flux under low crossflow-high permeate boundary conditions. Table 4.1 summarizes the relative loss in volume flux for the four boundary conditions.

The magnitude of the permeate water flux and the crossflow rate in a forward osmosis channel are physically coupled. Concentration polarization, which influences the permeate water flux, is more pronounced at lower crossflow velocities than at higher crossflow rates (Figure 4.3).

Table 4.1: Relative reduction of volume flow in the feed channel at various initial crossflow rates and fixed permeate velocities of $5.56 \times 10^{-7}\,\mathrm{m\,s^{-1}}$ (LP), $8.00 \times 10^{-7}\,\mathrm{m\,s^{-1}}$ (MP) and $2.78 \times 10^{-6}\,\mathrm{m\,s^{-1}}$ (HP) in %.

		$1 - \dot{V}_{\mathrm{out}}/\dot{V}_{\mathrm{in}}$ (%)
HC	HP	0.21
	MP	0.06
	LP	0.04
MC	HP	0.45
	MP	0.13
	LP	0.09
LC	HP	2.67
	MP	0.77
	LP	0.53

The thickness of the concentration polarization layer and the salt concentration at the membrane decrease as the crossflow velocity increases. Furthermore, concentration polarization increases towards the end of the channel (Figure A.3a, c and e) as the boundary layer fully develops. This effect is reinforced by a decreasing crossflow velocity in the feed channel as permeate is lost to the draw side. Concomitantly, the feed becomes more concentrated, as it is depleted of water while the salt is rejected by the membrane and the draw solution becomes more dilute. In consequence, the local transmembrane pressure, which is the driving force for the water flux through the membrane, decreases over the length of the channel [17, 45]. However, as this study only investigates four spacer elements instead of a whole channel, this dilution is negligible in calculating the permeate water flux.
In forward osmosis, back diffusion of the draw solute further lowers the difference in osmotic pressures between the feed and draw solution and, therefore, the permeate water flux [57]. According to equation 2.34, the reverse salt flux across the membrane increases with the transmembrane concentration difference. As the salt concentration in the feed channel is kept constant in all simulations, concentration polarization is more pronounced at higher salt concentrations in the draw channel (Figure A.3a, c and e). This effect is further enhanced by the increase in transmembrane water flux as the draw concentration increases. When more water is transported to the membrane, more salt is left behind in the boundary layer as the water passes through the membrane. Thus, the salt accumulates at the membrane.
The stagnation zones of the spacers on the membrane side of the channel exhibit an elevated salt concentration compared to other membrane near regions of the channel. Thus, the regions of elevated salt concentration expand or shrink depending on the crossflow velocity. In contrast, the salt mass fraction in the stagnation zones of the spacers on the draw side of the channel corresponds to the bulk salt mass fraction. As recirculation zones are characterized by a long residence time of the fluid elements, mixing between the main flow and the recirculation zones is impeded. Salt which is transported to membrane-near regions accumulates in the recirculation zone [55]. Opposite of the top spacer element, the concentration polar-

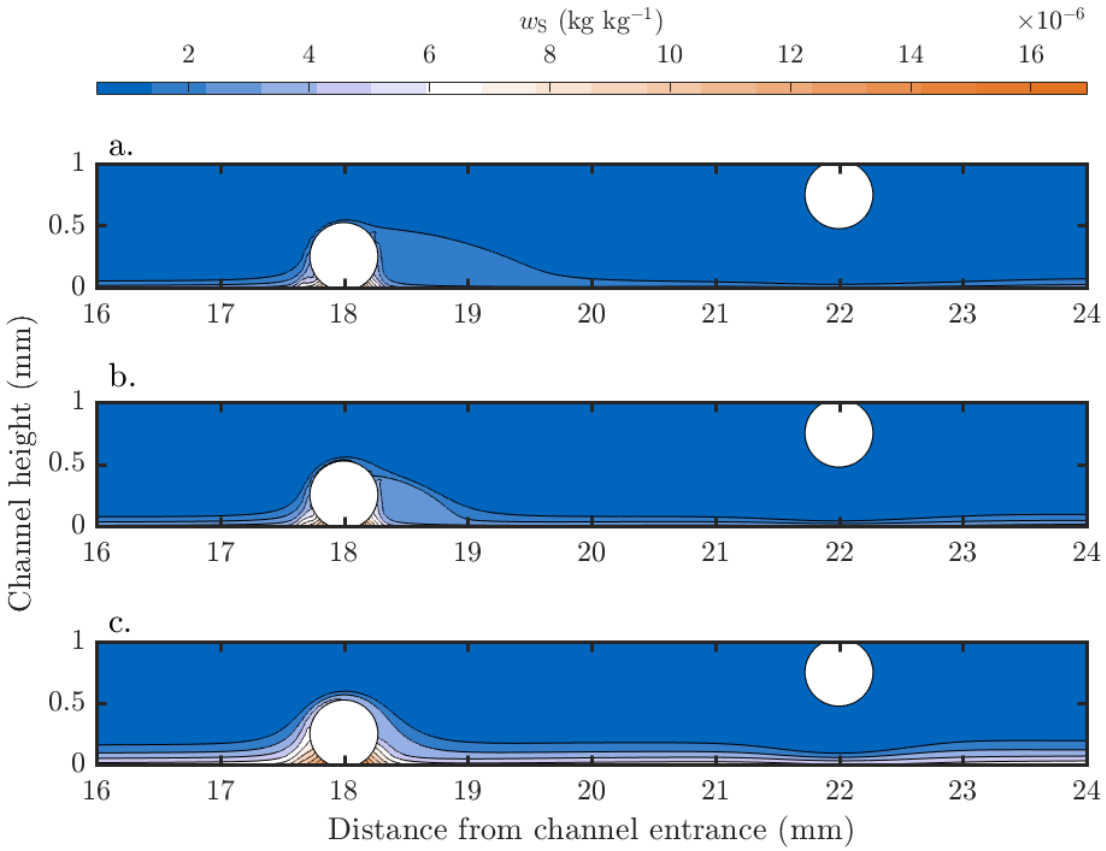

Figure 4.3: Concentration polarization in a forward osmosis channel with zig-zag spacer configuration. The average crossflow velocity at the inlet is a. $42.70 \times 10^{-3}\,\mathrm{m\,s^{-1}}$ (HC), b. $20.00 \times 10^{-3}\,\mathrm{m\,s^{-1}}$ (MC) and c. $3.34 \times 10^{-3}\,\mathrm{m\,s^{-1}}$ (LC) and the draw salt mass fraction is $7.4 \times 10^{-3}\,\mathrm{kg\,kg^{-1}}$.

ization layer becomes thinner and the membrane salt concentration decreases (Figure A.3a, c and e). Here, the increased shear stress facilitates the salt transport into the bulk phase, which is the main purpose of the spacer element. Similar concentration polarization patterns have been observed in spacer filled reverse osmosis [4] and membrane distillation channels [40].
The membrane water flux is approximately proportional to the local difference in salt concentration across the membrane. With the simplification that the draw salt mass fraction is constant over the length of the channel, the permeate water flux is thus proportional to the local salt concentration at the membrane (Figure A.3). The average permeate water fluxes in our simulations are slightly higher than expected based on the calculations in section 3.5.3 (Table 4.2). Possibly, the correlation for the Sherwood number does not fit our spacer geometry. Nevertheless, the average crossflow velocities in the concentration polarization experiments are within 5 % of the expected crossflow velocity. Thus, the comparison of the particle transport between the concentration polarization cases, the cases without concentration polarization and the corresponding experimental results [10] is valid.

Table 4.2: Permeate water fluxes as calculated by the simulation of the forward osmosis channel considering concentration polarization.

	m_S (10^{-3} kgkg^{-1})	u_w (10^{-6} ms^{-1})
HC	7.4	2.885
	1.6	0.822
	1.1	0.583
MC	7.4	2.884
	1.6	0.821
	1.1	0.583
LC	7.4	2.883
	1.6	0.821
	1.1	0.583

4.4 Trajectories of Single Particles

By calculating the motion of individual particles, the effect of the hydrodynamic transport mechanisms and body forces on the particle can be resolved in detail. Nine particles are uniformly distributed over the inlet of the channel, such that the distance between the particles is 0.1 mm. The distance from the bottommost particle to the membrane and from the uppermost particle to the channel wall is also 0.1 mm. All particles are released into the channel at the same time and the trajectories of the particles are recorded.

4.4.1 Particle Trajectories in the Bulk of the Channel Flow depend on Crossflow Velocity, Permeate Water Flux and Initial Point of Release

The trajectories of the particles in forward osmosis channel with uniform permeate water flux are depicted in Figure A.4 for medium and high crossflow velocities and in Figure 4.4d for the low crossflow velocity. Figure 4.4a-c shows the corresponding residence times of the particles in the channel as a function of their initial point of release. At the highest crossflow velocity, the particle tracks for the three permeate water fluxes are indistinguishable. The particles follow the streamlines of the crossflow without permeation (Figure A.4a), which serve as a reference for the lateral motion of the particles due to permeation drag and lift forces. The residence time distribution of the particles in the channel resembles an inverse parabolic flow profile (Figure 4.4a).
At the medium crossflow velocity, the particles also approximately follow the streamlines of the channel flow without permeation (Figure A.4b). The residence time of the particle closest to the membrane at the high permeate water flux is slightly higher than at the low and the intermediate permeate water flux (Figure 4.4b). The residence times of the other particles at a medium crossflow velocity fall on the parabolic distribution.
At the lowest crossflow velocity, not all particle trajectories can be approximated by the streamlines without permeate water flux (Figure 4.4d). Visibly, the trajectories of the upper eight particles which are transported at low permeate water flux and low crossflow velocity are in-

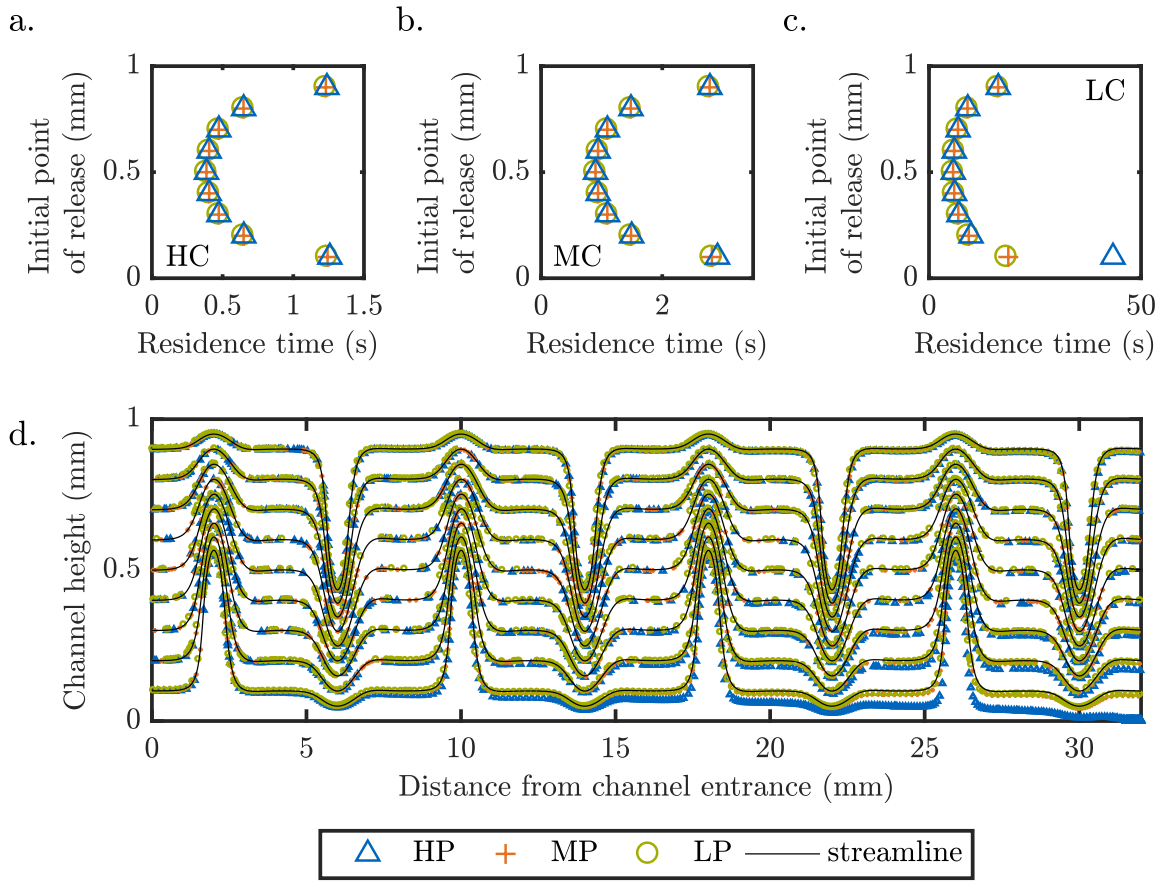

Figure 4.4: Residence time of the particles in the channel at a crossflow velocity of a. $42.70 \times 10^{-3}\,\mathrm{m\,s^{-1}}$ (HC), b. $20.00 \times 10^{-3}\,\mathrm{m\,s^{-1}}$ (MC) and c. $3.34 \times 10^{-3}\,\mathrm{m\,s^{-1}}$ (LC). d. Particle trajectories over four spacer elements at a crossflow velocity of $3.34 \times 10^{-3}\,\mathrm{m\,s^{-1}}$. The streamlines are the streamlines of the flow without permeate water flux.

distinguishable from the streamlines without permeate water flux. The bottommost particle, however, deviates slightly from this streamline in the fourth spacer element. Similarly, the bottommost particle at low crossflow velocity and medium permeate water flux also tends more towards the membrane than the streamline of the flow without permeate water flux, while the other eight particles approximately follow their respective streamlines. At the high permeate water flux, the bottom three particles are pulled towards the membrane, while the other six particles follow the streamlines of the flow without permeate water flux. The residence time distribution of the particles in the three flow scenarios with low crossflow velocity is depicted in Figure 4.4c. The upper particles at all three permeate water fluxes follow the residence time distribution of the channel flow without permeate water flux which resembles an inverse parabolic profile. However, the bottommost particle in all three flow scenarios exhibits a longer residence time than expected based on the ideal inverse parabolic flow profile. The residence time of the particle which is released at $0.1H$ increases with the permeate water flux.

Table 4.3: Ratios of the residence time of the particle which is released at $0.9H$ divided by the residence time of the particle which is released at $0.1H$.

	LC	MC	HC
HP	0.376	0.957	0.984
MP	0.871	0.987	0.990
LP	0.888	0.984	0.991

In general, particles which are closer to a channel wall or membrane exhibit longer residence times in the channel, because the horizontal velocity component of the fluid flow is lower in proximity to these no-slip surfaces. Therefore, a longer residence time of the bottom particles in the forward osmosis channel indicates that the particles are transported towards the membrane. The ratio of the residence time of the particle which is released at $0.9H$ to the residence time of the particle which is released at $0.1H$ serves as an indicator for the influence of the flow conditions in the channel on the particle trajectory. If the bottom wall of the channel is moderately permeable, the permeate water flux hardly influences the residence time of the particle close to the impermeable wall, while the residence time of the particle which is released at $0.1H$ increases as the particle is transported towards the membrane. In the extreme case that the particle which is released at $0.1H$ attaches to the membrane, the residence time of this particle in the channel becomes infinitely long and the characteristic ratio approaches zero. A flow with an impermeable bottom wall poses the other extreme for the ratio of the residence time of the particle which is released at $0.9H$ to the residence time of the particle which is released at $0.1H$. Here, the ratio of the two residence times is equal to one, because the particle which is released at $0.1H$ exhibits the same residence time as the particle which is released at $0.9H$.[2] Table 4.3 summarizes the residence time ratios for all nine flow scenarios. The residence time ratios, which are smaller than one at all flow conditions, indicate that the bottommost particles are transported towards the membrane. In hydrodynamic conditions which exhibit smaller residence time ratios, the particles tend more towards the membrane than in the hydrodynamic conditions with larger residence time ratios. Thus, the residence time ratio also serves as an indicator for the deposition probabiliy of the particles at a given crossflow velocity and permeate water flux. For the three crossflow velocities in this study, the residence time ratio decreases as the permeate water flux increases. The deposition of the particles becomes more likely at higer permeate water fluxes, because an increase in permeate water flux gives rise to a higher drag force towards the membrane. In contrast, the residence time ratio increases with the crossflow velocity in the channel. Higher crossflow velocities in-

[2] This is only true if gravity is negligible and if the flow in the channel is laminar.

duce lift forces, which transport the particles away from the membrane. Thus, the particle deposition becomes less likely as the crossflow velocity increases. Although all particles are transported towards the membrane, the drift of the bottommost particle towards the membrane is the least significant at the high crossflow velocity.
The key assumption of the residence time ratio is that the particle which is released at $0.9H$ approximately follows the streamline of the channel flow. The particle trajectories in Figure A.4 and Figure 4.4d confirm this assumption. However, the residence time ratio does not provide information on how far the influence of the permeate water flux extends into the channel. Figure 4.4d shows that the particle which is released into the low crossflow and high permeate water flux channel at $0.2H$ also tends towards the membrane, but its lateral motion in the channel cannot be quantified with the residence time ratio. Nevertheless, the residence time ratio provides a good measure for the probability of particle deposition at varying crossflow velocities and permeate water fluxes in a forward osmosis module, as it indicates how strongly the particle trajectory deviates from the streamline without permeate water flux towards the membrane.

4.4.2 Concentration Polarization Influences Deposition of Particles

The particle trajectories in the cases which consider concentration polarization (Figure A.5) resemble the particle trajectories without concentration polarization. As in the ideal cases, the lateral motion of the particles towards the membrane is negligible for the high crossflow velocity. At the medium crossflow velocity, the particles also approximately follow the streamlines of the impermeable channel. At low crossflow velocity and low or medium permeate water flux, the bottommost particles deviate from their corresponding streamlines without permeate water flux. In the configuration with the low crossflow velocity and high permeate water flux, the lower three particles show a net lateral motion towards the membrane. Within the fourth spacer element, the particle which is released at $0.1H$ attaches to the membrane. This has not been observed for the corresponding particle in the channel with a uniform permeate water flux (c.f. section 4.4.1). Thus, the local differences in permeate water flux resulting from concentration polarization alter the particle trajectories.
The two flow scenarios in which the permeation drag exhibits the strongest influence on the particle trajectories, namely low crossflow and medium permeate water flux and low crossflow and high permeate water flux, are further investigated to gain deeper insight on the effect of concentration polarization on the particle deposition. Figure 4.5 compares the cases which consider concentration polarization (real) to the cases which assume a uniform permeate water flux (ideal). The panels depict a close-up of the bottom quarter of the fourth spacer element instead of the entire channel to obtain a better spatial resolution of the particle trajectories and streamlines. The apparent discontinuities in the streamlines and the particle trajectories result from the bottom spacer filament. As the particles travel around the filament, their lateral distance from the membrane becomes larger than 0.5 mm (Figure 4.4d and Figure A.5c). Thus, the close-ups do not show the entire particle trajectory in the fourth spacer element, but only the sections which lie below $0.25H$.
At low crossflow velocity and medium permeate water flux (Figure 4.5a) the particle trajectories of the ideal and the real flow conditions lie on top of each other. They follow the fluid

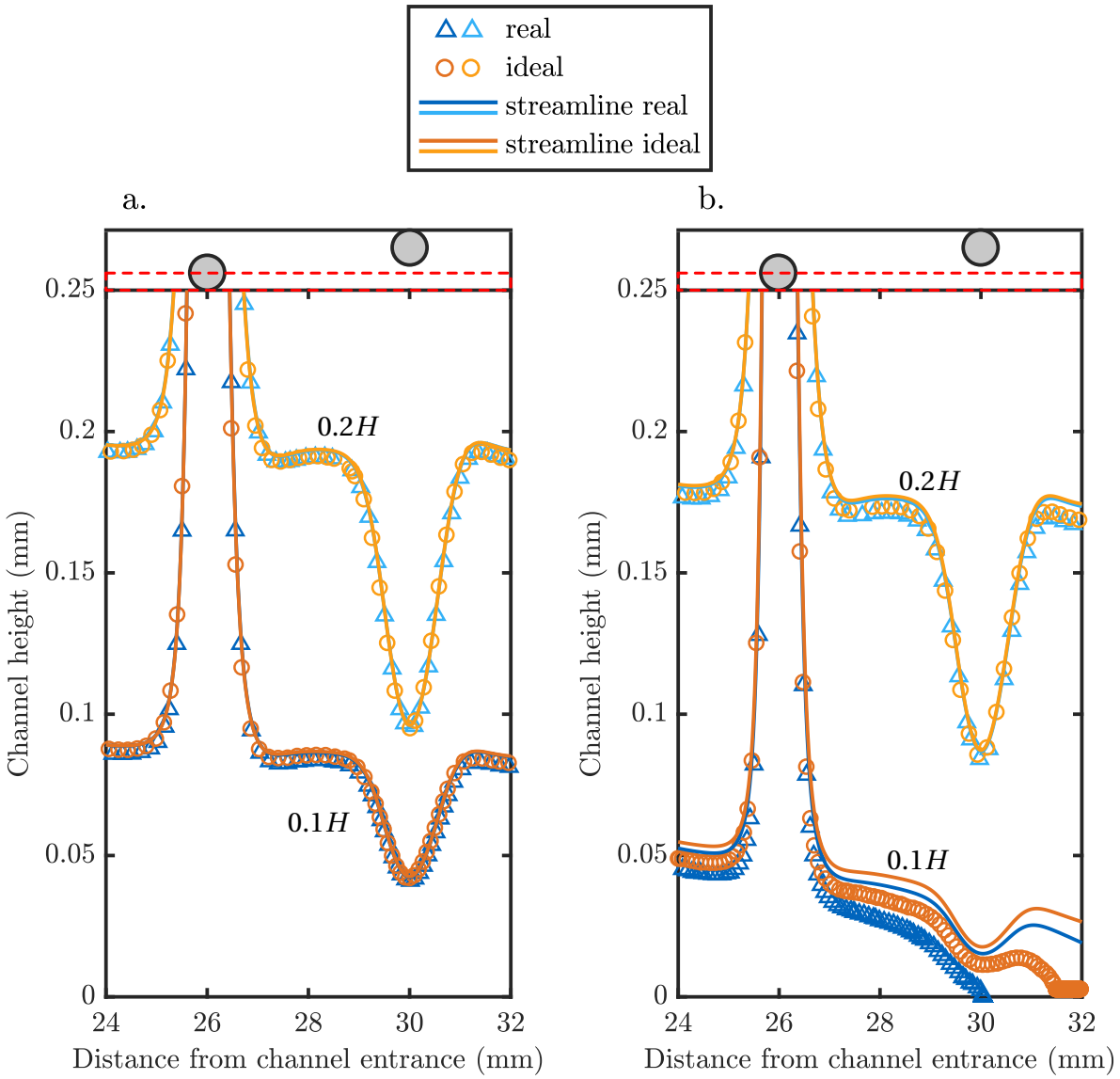

Figure 4.5: Close-up of the particle trajectories of the bottom two particles in the last spacer element of the channel at a crossflow velocity of $3.34 \times 10^{-3}\,\mathrm{m\,s^{-1}}$ (LC) and a. medium permeate water flux and b. high permeate water flux. The trajectories which were calculated with a uniform permeate water flux are orange and the trajectories which were calculated considering concentration polarization are blue. The light blue and the light orange correspond to the trajectories of the particles which are released into the channel at $0.2H$, while the darker colors mark the trajectories of the particles which are released into the channel at $0.1H$. The streamlines of the respective flows are marked in the corresponding color.

streamlines of the real and ideal flow, which also coincide. Hence, at low crossflow velocity and medium permeate water flux, local variations in permeate water flux do not alter the particle trajectories compared to the simplified case with a uniform permeate water flux. The particles are transported with the main flow, and volume forces, which act perpendicular to

the membrane, are negligible. In this flow regime, the particle trajectories can be approximated with the streamlines of the fluid in the ideal channel if their initial point of release lies between $0.1H$ and $0.9H$. Hence, the detailed resolution of the particle forces to determine the trajectories of these particles becomes obsolete.
The close-up of the channel at low crossflow and high permeate water flux is strikingly different (Figure 4.5b). While the trajectories of the particles which are released at $0.2H$ follow the same trajectory in the ideal and in the real case, the trajectory of the particle which is released into the real channel flow at $0.1H$ deviates from the trajectory of the corresponding particle in the ideal case. The particle which is released at $0.1H$ attaches to the membrane opposite of the upper spacer element (x = 30.0 mm) when concentration polarization is considered. In contrast, the ideal trajectory reaches the membrane at a distance of 31.2 mm from the channel entrance, but the particle does not attach to the membrane. In both cases, the particle trajectories deviate from the streamlines of the respective flows.
If only surface forces acted on the particles as they are transported along the channel, the particles would predominantly follow the fluid streamline. Therefore, the gravitational force, which is the only body force that acts on the particles in the bulk flow, must cause the observed deviation of the particles from their streamline. After the particles are hydrodynamically transported to the boundary region in proximity of the membrane, their horizontal velocity decreases, such that the residence time of the particle in the channel increases. This gives the particle more time to settle, which is a very slow process because of the small density difference between the particle and the continuous phase. Subsequently, as the particles approach the membrane, the permeation drag increases, such that the overall lateral force on the particles increases, too. This combined mechanism of gravitational force and permeate drag force eventually causes the particles to reach the membrane faster than expected based on the corresponding streamlines of the fluid.
When concentration polarization is considered, the particle trajectory tends even more towards the membrane than expected based on the streamline of the flow (Figure 4.5b). Potentially, when the particle deviates from the streamline of the flow with concentration polarization due to gravity, it comes sufficiently close to the membrane, such that the local differences in permeation drag influence its motion. The local permeation drag is the strongest opposite of the upper spacers and the weakest besides the lower spacers (Figure A.3). However, the particle is only close to the membrane in the regions of elevated permeation drag. Thus, the effective permeation drag which the particle experiences is higher than in the ideal case. Therefore, the transport of the particle toward the membrane is more pronounced compared to the ideal case.
When the particles reach the membrane, the real particle attaches immeadiatly, while the ideal particle does not stick to the membrane. Colloidal forces, which act as a deposition criterion in this simulation, favor particle-membrane interactions at elevated salt concentrations. Thus, concentration polarization facilitates the irreversible attachment of the particles to the membrane because the solute compresses the electrostatic double layer of the membrane and the particle. However, in the ideal simulation the solute concentration at the membrane corresponds to the bulk solute concentration, such that the surface charge of the particle and the membrane remains almost unaltered. In this case the forces which push the particle towards the membrane cannot overcome the electrostatic repulsion between the particle and

the membrane and the particle cannot attach.

4.4.3 Comparison of the Results for the Single Particles to the Literature

Radu et al. [60] simulated their particles as points following the streamlines of the flow. They did not resolve the particle forces and wall interactions of the particles in their analysis of a spacer-filled channel. As we demonstrated here, this approximation holds well in comparably high Reynolds number flows and when the particles are truly neutrally buoyant. The Stokes number St provides a measure for the degree to which the particle is tied to the fluid [19]

$$\mathrm{St} = \frac{\tau_\mathrm{P}}{\tau_\mathrm{Flow}} = \frac{\rho_\mathrm{P} d_\mathrm{P}^2 u_\mathrm{c}}{18 \eta_\mathrm{F} d_\mathrm{h}}. \tag{4.1}$$

Here, τ_P is the particle momentum response time and τ_Flow is a characteristic time scale of the flow. In the present geometry, the characteristic time scale of the flow is calculated with the crossflow velocity at the channel entrance u_c and the hydraulic diameter of the channel d_h. In all cases, the Stokes number lies in the range $\mathrm{St} = 1.1 \times 10^{-6}$ to 1.4×10^{-5}. Thus, the particles respond instantaneously to changes in the fluid motion, i.e. the particles follow the streamlines. If the membrane boundary condition is chosen such that the streamlines in the channel consider concentration polarization, neutrally buoyant particles even follow the streamlines of the flow close to the membrane. However, if gravity plays a role in the particle motion, the particles deviate from the streamlines of the flow as they approach the wall. In this case the force equation of the particles must be solved to accurately predict the deposition.
The trends for particle deposition which can be inferred from the residence time ratio agree with Bogler et al.'s [10] experimental observations for the particle deposition in a forward osmosis module. In accordance with the residence time ratios in Table 4.3, they reported the highest deposition at low crossflow velocity and high permeate water flux, followed by low crossflow velocity and low permeate water flux flow conditions and high crossflow velocity and high permeate water flux flow conditions. The lowest deposition was observed at high crossflow velocity and low permeate water flux.

4.5 Deposition Patterns

The particle deposition patterns in the two extreme cases high crossflow with low permeate water flux and low crossflow with high permeate water flux are depicted in Figure 4.6. The second spacer element was chosen as a representative spacer element, because it is sufficiently far from the channel entrance to not show significant entrance effects [43], but the deposition numbers are still high enough to obtain a statistically sound deposition pattern. Concentration polarization was considered in both flow scenarios.
The spacer element was divided into 16 zones to evaluate the spatial distribution of the deposited particles in the channel. Each zone is 0.5 mm long. The deposition within one zone is the number of particles which sticks to the membrane in the respective zone divided by the number of particles which enter the zone with the crossflow. Thus, the deposition is adjusted for the particles which attach to the membrane upstream of the regarded zone.

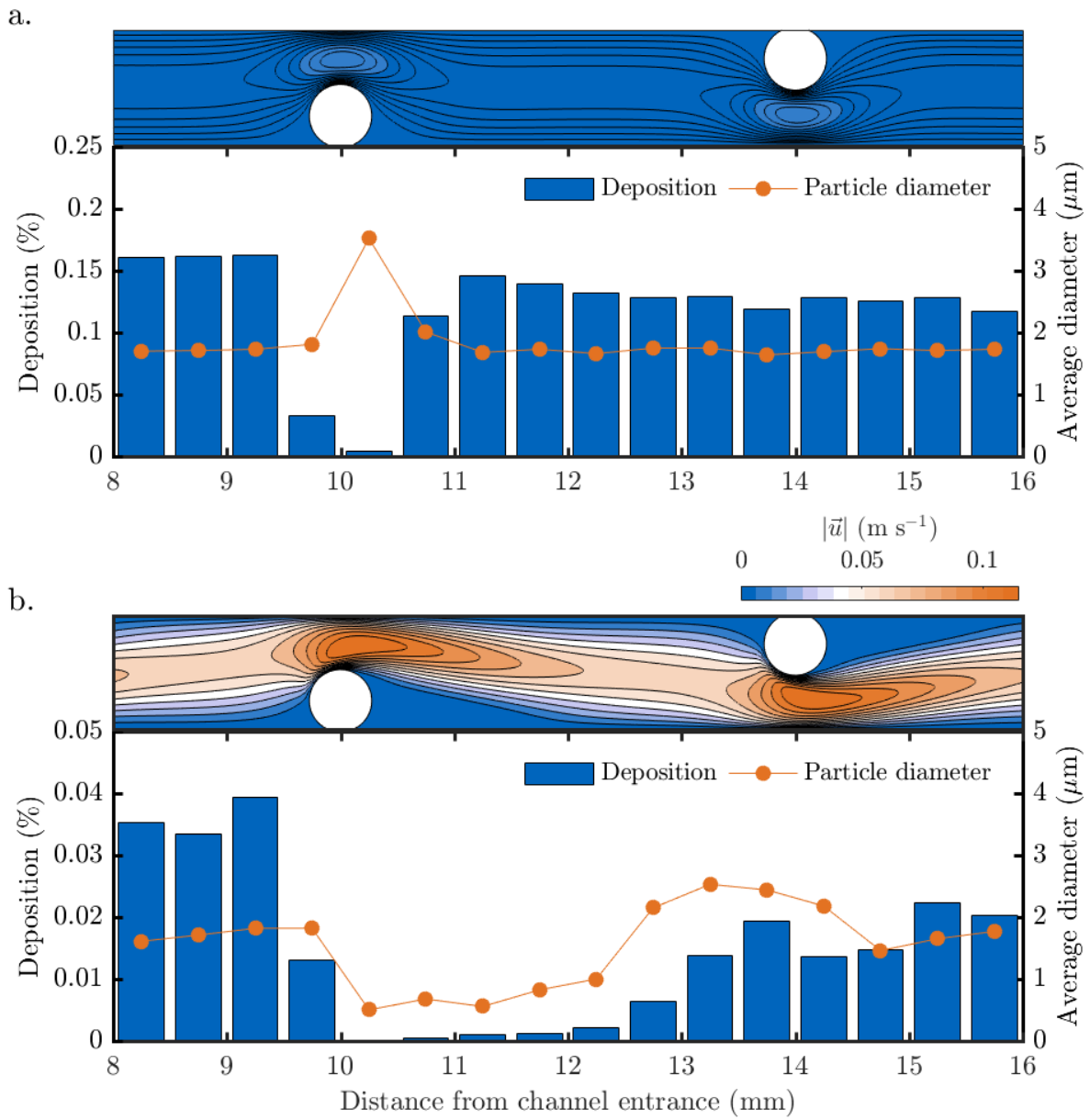

Figure 4.6: Particle deposition in the second spacer element of the forward osmosis channel at a. a crossflow velocity of $3.34 \times 10^{-3}\,\mathrm{m\,s^{-1}}$ (LC) and gauge draw salt mass fraction of $7.4 \times 10^{-3}\,\mathrm{kg\,kg^{-1}}$ and b. a crossflow velocity of $42.70 \times 10^{-3}\,\mathrm{m\,s^{-1}}$ (HC) and a gauge draw salt mass fraction of $1.1 \times 10^{-3}\,\mathrm{kg\,kg^{-1}}$.

4.5.1 Uniform Deposition at Low Crossflow and High Permeate Water Flux

At low crossflow and high permeate water flux, the deposition of the particles on the membrane is mostly uniform with an attachment efficiency between 0.113 % and 0.167 % (Figure 4.6a). However, only 0.004 % to 0.033 % of the particles deposit in the zones between 9.5 mm from the channel entrance and 10.5 mm from the channel entrance. Here, the spacer

filament reduces the surface area of the two zones compared to the other zones, because it intersects the membrane. Additionally, the zones which exhibit lower deposition correspond to the areas in which the flow is detached from the membrane. As the Stokes number of the flow is very low (c.f. section 4.4), the particles mostly remain within the main flow of the channel and are not transported into the recirculation zones by inertial forces. Thus, the deposition in the recirculation region is lower than in the areas in which the main flow is attached to the membrane.
The results of the simulation are in agreement with the experimental results by Bogler et al. [10], who also observe a unform particle distribution at low crossflow velocity and high permeate water flux. To quantify the deposition, they divide a membrane area enclosed by a three dimensional spacer element into nine distinct, equally sized diamond-shaped zones. In each of the zones the deposited fluorescently labelled polystyrene beads are counted to determine the deposition pattern of the beads. The two-dimensional slice in this simulation corresponds to a slice of the three-dimensional geometry which intersects one filament that touches the membrane and one filament that touches the impermeable top wall. The slice is aligned with the main flow direction in the experimental channel and lies in a 45° angle to the three-dimensional spacer filaments. In contrast to the simulation, the experiments did not show a lower attachment in the stagnation zones. Possibly, the lower deposition in proximity to the bottom spacer filament is not captured in the image of the spacer element because the filament covers this area in the top view. Different flow patterns in the three-dimensional channel compared to the two-dimensional approximation could provide a physical explanation for the discrepancy between simulation and experiment. The spacer filaments in the experiment leave voids between the filament and the membrane for the water to pass through. Additionally, the three-dimensional flow profile exhibits local fluxes at an angle to the main flow direction of the channel [10]. Therefore, the experimental flow at low crossflow and high permeate water flux might not exhibit recirculation zones in the corner between the membrane and the spacer filament and could, hence, transport particles to deposition locations close to the bottom spacer filament.
While Bogler et al. [10] used uniform beads with a diameter of 1 µm, the deposition simulation allows for a detailed resolution of the sizes of the deposited particles. Here, a Rosin-Rammler size distribution (Figure A.7, $n = 0.5$, $d_{\mathrm{P,mean}} = 3\,\mu\mathrm{m}$) with particle diameters between 0.5 µm and 5.5 µm was randomly injected over the inlet patch. The average diameter of the particles is 1.711 µm. The average diameter of the deposited particles is homogeneous over most deposition zones with an average diameter of 1.74 ± 0.09 µm (Figure 4.6a). Only the deposition zone right behind the spacer filament at the membrane exhibits a higher average particle diameter of 3.52 µm.
The average diameter of the deposited particles in all deposition zones except for the deposition zone behind the bottom spacer filament corresponds to the average diameter of the injected particles. Thus, the deposition efficiency is equal for all particle diameters. As Chellam et al. [16] showed, the particle deposition efficiency on the membrane depends on the ratio of lift force to permeation drag force. On the one hand, the lift force, which accelerates particles away from the membrane, is proportional to the square of the particle diameter [67]. On the other hand, the sphere drag force from the permeate water flux, which hydrodynamically pulls particles towards the membranes, only scales linearly with the diameter of the

particle [44]. Hence, the ratio of lift force to drag force is proportional to the particle diameter and larger particles experience less drag towards the membrane than smaller particles. However, all particles within this size distribution are in the transport regime which is governed by permeation drag [10, 16].
In contrast to the average diameter of the deposited particles in all other deposition zones, the average diameter of the deposited particles in the deposition zone behind the bottom spacer filament exhibits a higher particle diameter than the average injected particle. Immediately behind the spacer, inertial transport of particles away from their streamline might superimpose the particle motion along the fluid streamline. The Stokes number provides a measure for how tight the particles are tied to the streamlines of the fluid flow. It is proportional to the square of the diameter of the particles (equation 4.1), such that it is 100 fold larger for the largest particles ($St = 3.60 \times 10^{-6}$) compared to the smallest particles ($St = 2.98 \times 10^{-8}$). However, even for the largest particle the Stokes number is still much smaller than 1 ($St \ll 1$), such that the particles react promptly to changes in the flow direction of the continuous phase. Therefore, the overall deposition in the deposition zone behind the bottom spacer filament is lower than in the other deposition zones, but the orders of magnitude difference between the Stokes numbers of the small and the large particles could cause the elevated average particle size of the deposited particles in this deposition zone.

4.5.2 Lower Deposition in Recirculation Zone and in Region of High Shear Stress

While both the number of deposited particles and the average diameter of the deposited particles are very uniform at low crossflow velocity and high permeate water flux, the deposition at high crossflow and low permeate water flux is highly heterogeneous. Figure 4.6b shows the particle deposition pattern in the second spacer element. The deposition efficiency between 9.4×10^{-5} % and 3.9×10^{-2} % is on average an order of magnitude lower than the deposition at low crossflow and high permeate water flux. At high crossflow and low permeate water flux, the deposition efficiency reaches its highest value before the bottom spacer filament (3.0×10^{-2} % to 4.0×10^{-2} %). In the five deposition zones which follow behind the bottom spacer filament, the deposition efficiency is smaller than 2.0×10^{-3} %. These five deposition zones correspond to the regions in which the flow is detached from the membrane. After this section, the deposition efficiency increases again up to a value of 2.0×10^{-2} %, before the deposition becomes slightly lower opposite of the top spacer filament and then increases again. Similar to the deposition at low crossflow and high permeate water flux, the recirculation zone behind the spacer filament inhibits the attachment of particles to the membrane. As the elevated salt concentration in the recirculation zone (Figure 4.3) compresses the electrostatic double layer around the particle and on the membrane, the electrostatic repulsion decreases, such that the attachment is facilitated compared to regions of lower salt concentration in the main flow. Hence, colloidal forces would enhance the deposition in the recirculation zones, but the flow conditions impede the deposition of particles in this region. The particles mostly follow the streamlines of the main channel flow (c.f. section 4.4). Thus, they are only rarely transported into the recirculation zones convectively, because there is hardly any fluid exchange between the recirculation zones and the main flow.

As the main channel flow re-attaches to the membrane, the particles deposit again. However, the deposition efficiency decreases opposite of the top spacer filament. As the crossflow accelerates between the filament and the membrane due to a reduction in cross sectional area of the channel, the shear in the crossflow increases. Simultaneously, the permeate flux increases slightly because of lower concentration polarization in the region of high shear stress (Figure A.3). While the higher permeate flux accelerates the particles towards the membrane, the strong shear in the fluid gives rise to an elevated lift force [67]. At high crossflow and low permeate water flux this lift force outweighs the permeation drag and reduces the overall deposition.
The recirculation zone exhibits a lower deposition efficiency than the region of elevated shear stress. In contrast to the recirculation zone, particles are transported to the region of high shear stress, but the net force on the particles prevents them from attaching to the membrane. Bogler et al. [10] observed a deposition front behind the top spacers. They attribute the region of lower deposition downstream of the upper spacer filaments to a region of increased shear stress. Similar to the simulation, a small number of particles still attaches to the membrane in the respective deposition zones. However, the flow conditions in the three-dimensional experiment differ strongly from the two-dimensional approximation of the simulation. In the experiment, the major local flow direction at high crossflow and low permeate water flux is parallel to the spacer elements which touch the membrane and perpendicular to the spacer elements which touch the impermeable top wall [10]. Therefore, the predominant local flux in the filament is better approximated by the flow through a channel slice with spacer cavities that touch the impermeable wall instead of the zig-zag slice in this study. Nevertheless, besides the reduced deposition downstream of the upper spacer filament, the experiment also shows the lowest particle deposition downstream of the spacer filament which touches the membrane. While the three-dimensional geometry might not allow for the development of extended recirculation zones, the reduced deposition of the particles in regions of lower mixing behind the lower spacer filaments can be confirmed by the experiment. Both the simulation and the experiment exhibit a highly inhomogeneous particle deposition pattern in the spacer element at high crossflow velocity and low permeate water flux with lower deposition efficiencies downstream of upper and lower spacer filaments.

4.5.3 Particle Size Distribution of Deposited Particles Confirms Dominant Regional Deposition Mechanisms

The average diameter of the deposited particles at high crossflow and low permeate water flux also depends on the deposition zone of the spacer element (Figure 4.6b). At these flow conditions, one spacer element can be divided into three distinct deposition regions which each exhibit a different average diameter of the deposited particles. In the four zones before the first spacer filament and the last three deposition zones of the elementary cell, the average diameter of the deposited particles is 1.69 ± 0.13 µm. As more than one spacer element is simulated, this first deposition region corresponds to the region between an upper spacer filament and the subsequent bottom spacer filament. The recirculation zone, which consists of the five deposition zones downstream of the bottom spacer filament, is the second deposition region. Here, the average diameter of the deposited particles is significantly lower (0.71

± 0.20 µm) than in the first deposition region ($p > 0.99$). Lastly, the three deposition zones upstream of the upper spacer filament together with the first deposition zone downstream of the upper spacer filament constitute the third deposition region. The average diameter of the deposited particles in this region is 2.33 ± 0.19 µm, which is significantly higher than in the first deposition zone ($p > 0.99$). Here, the flow attaches to the membrane and is subsequently accelerated as the cross sectional area of the channel is reduced.
The average diameter of the deposited particles provides insights into the dominant deposition mechanism of the respective regions. In the first deposition region, the average diameter of the deposited particles is comparable to the average diameter of the deposited particles at low crossflow and high permeate water flux (Figure 4.6a). The permeation drag towards the membrane outweighs the lift force at all particle diameters. While the hydrodynamic parameters, namely crossflow and permeate water flux, are not comparable to the flow conditions at low crossflow and high permeate water flux, the deposition mechanism in this region corresponds to the deposition mechanism at low crossflow and high permeate water flux. The particles are convectively transported to the membrane, where their attachment efficiency depends on the permeation drag. As the drag force due to permeation increases with the permeate water flux, the overall attachment efficiency in this region is lower than at low crossflow and high permeate water flux (c.f. section 4.5.2).
The particles which deposit on the membrane in the recirculation region are predominantly smaller than 1 µm. In this second deposition region, convective transport of the particles is negligible. Instead, the particle transport is dominated by Brownian motion, which is the mechanism by which particles diffuse in a fluid. On a molecular level, Brownian motion is facilitated by random particle molecule collisions. As a water molecule collides with a particle, it transfers a part of its momentum to the particle, such that the magnitude and the direction of the velocity of the particle (and the water molecule) change. However, for particles whose mass is orders of magnitude larger than the mass of the water molecule, this momentum exchange only marginally alters the velocity of the particle. Thus, the diffusive motion of larger particles ($d_P > 1\,\mu m$) is negligible. In contrast, the momentum exchange between a molecule and a nano-sized particles can significantly influence the motion of the particle [35]. Hence, the smallest of the injected particles are diffusively transported into and within the recirculation zones where they eventually deposit. As diffusion is much slower than convection, the deposition efficiency in the second deposition region is lower than in the other two deposition regions.
The average diameter of the deposited particles in the third deposition region is higher than the average injection diameter and the average diameter in the other two deposition regions. Similar to the deposition zone in in which the flow re-attaches to the membrane in the high crossflow and low permeate water flux simulation (Figure 4.6a; c.f. section 4.5.1), larger particles might be inertially transported to the membrane as the main flow changes direction. Thus, the deposition in the third deposition region is governed by a mix of hydrodynamic and inertial forces.

5 Conclusions and Future Work

The purpose of this work was to obtain a detailed understanding of the particle transport and deposition mechanism in a forward osmosis module. With this knowledge, strategies for fouling mitigation through optimization of the hydrodynamic conditions in the channel can be developed. As the particles which enter desalination modules are typically very small, because larger particles are removed in the pre-treatment of the feed, experimental options to explore the forces which act on the particles in the weakly compressible salt water shear flow are limited. Thus, a simulative approach was chosen in this study.
The objective of this thesis was to develop a numerical model which (i) represents the flow conditions in the channel as accurately as possible and (ii) incorporates all the relevant particle forces. The first objective was met by implementing a new set of boundary conditions which model the water and salt flux through the membrane. With these boundary conditions the local permeate water flux through the membrane is resolved. Additionally, the numerical model determines the local salt mass fraction in the channel, such that the variations in the fluid properties, namely density, viscosity and Debye length, are correctly considered when solving the particle transport equation.
With an in depth understanding of the origin and effect of the forces which act on a particle in a fluid flow, the seven most relevant forces were selected and incorporated into the model. To the best of our knowledge, this is the first computational fluid dynamic model for the particle transport in a spacer filled desalination module which incorporates hydrodynamic forces, colloidal forces and diffusive transport. Furthermore, previous models have not explicitly resolved the local variations in membrane water flux and salt concentration.
In a first set of simulations, the model was applied to single particles which are released into a forward osmosis channel at defined locations. With these simulations we could confirm that the particles predominantly follow the streamlines of the main flow. However, close to the membrane, the particle trajectories detach from the streamlines of the fluid, such that the particles deposit faster than expected based on the streamlines. The local variation in permeate water flux due to concentration polarization also affects the particle motion in the near membrane region. Understanding the trajectories of single particles lies the basis for predicting the effective particle deposition in a forward osmosis module. The residence time ratio, which compares the residence time of a particle which is released in the upper half of the forward osmosis module to the residence time of a particle which is released in the lower half of the forward osmosis module serves as a predictor for the deposition probability at certain hydrodynamic flow conditions. In accordance with the experimental results by Bogler et al. [10], we observe that the deposition probability of the particles increases with an increase in permeate water flux and a decrease in crossflow velocity. The behavior is attributed to the ratio of lift force to drag force which determines the lateral motion of the particles.
A second set of simulations studied the particle deposition pattern in a representative spacer

element of the forward osmosis channel. While the deposition efficiency in distinct zones on the membrane has been reported previously [43], we conducted the first simulations which also investigated the particle size distribution of the deposited particles. At low crossflow velocity and high permeate water flux, a uniform particle distribution, both in number and in size, was observed on the membrane. In contrast, the particle deposition was more heterogeneous at high crossflow and low permeate water flux. Here, three distinct deposition zones could be identified. In the first deposition zone, the deposition efficiency of the particles is the highest and the particle size distribution corresponds to the size distribution of the particles which enter the channel. In the second deposition zone, which is characterized by a detachment of the crossflow from the membrane, the particles are mostly transported to the membrane through diffusion. Thus, the overall deposition and the average size of the deposited particles in this deposition zone is lower than the average particle size in the channel. The third deposition zone is the region in which the main flow re-attaches to the membrane. Here, the average size of the deposited particles is larger than the average size of the injected particles, because the particles are transported to the membrane by inertial forces. Overall, we could infer that the local particle deposition is the highest at moderate shear. Regions of high local shear and the recirculation zones exhibit lower deposition efficiencies.
Future investigations should aim at analyzing different spacer geometries and transferring the model to a three-dimensional representation of a forward osmosis channel. If this is successful, the model can be used as a tool to find the optimal parameters which minimize the particle deposition through a combination of geometrical and hydrodynamic optimization. Additionally, an extension of the model to account for particle-particle interaction could resolve later stages of particle deposition.

Bibliography

[1] A. L. Ahmad, K. K. Lau, and M. Z. Abu Bakar. Impact of different spacer filament geometries on concentration polarization control in narrow membrane channel. *Journal of Membrane Science*, 262(1-2):138–152, 2005.

[2] A. Alexiadis, D. E. Wiley, D. F. Fletcher, and J. Bao. Laminar flow transitions in a 2D channel with circular spacers. *Industrial and Engineering Chemistry Research*, 46(16):5387–5396, 2007.

[3] Raphaela Allgayer. Influence of water chemistry on methylene blue adsorption by hybrid graphene oxide-cellulose nanocrystal sponge, 2019.

[4] M. Amokrane, D. Sadaoui, C. P. Koutsou, A. J. Karabelas, and M. Dudeck. A study of flow field and concentration polarization evolution in membrane channels with two-dimensional spacers during water desalination. *Journal of Membrane Science*, 477:139–150, 2015.

[5] Peter W. Atkins and Julio de Paula. *Physikalische Chemie*. Wiley-VHC, Weinheim, 5 edition, 2013.

[6] T. R. Auton. The lift force on a spherical body in a rotational flow. *Journal of Fluid Mechanics*, 183:199–218, 1987.

[7] T. R. Auton, J. C.R. Hunt, and M. Prud'Homme. The force exerted on a body in inviscid unsteady non-uniform rotational flow. *Journal of Fluid Mechanics*, 197:241–257, 1988.

[8] Amrit Bhinder, Simin Shabani, and Mohtada Sadrzadeh. Effect of Internal and External Concentration Polarizations on the Performance of Forward Osmosis Process. *Osmotically Driven Membrane Processes - Approach, Development and Current Status*, 2018.

[9] Anne Bogler, Andreas Kastl, Markus Spinnler, Thomas Sattelmayer, Avraham Be'er, and Edo Bar-Zeev. Particle counting and tracking: Zooming on deposition and flow paths during initial stages of cake formation in forward osmosis with spacers. *Journal of Membrane Science*, page 117619, oct 2019.

[10] Anne Bogler, Andreas Kastl, Markus Spinnler, Thomas Sattelmayer, Avraham Be'er, and Edo Bar-Zeev. Where, when and why? Quantifying the relation of particle deposition to crossflow velocity and permeate water flux in forward osmosis. *Journal of Membrane Science*, 604(March):118055, 2020.

[11] Chanhee Boo, Sangyoup Lee, Menachem Elimelech, Zhiyong Meng, and Seungkwan Hong. Colloidal fouling in forward osmosis: Role of reverse salt diffusion. *Journal of Membrane Science*, 390-391:277–284, 2012.

[12] Howard Brenner. The slow motion of a sphere through a viscous fluid towards a plane surface. *Chemical Engineering Science*, 16(3-4):242–251, 1961.

[13] G. J. Brown. Erosion prediction in slurry pipeline tee-junctions. *Applied Mathematical Modelling*, 26(2):155–170, 2002.

[14] Tzahi Y. Cath, Amy E. Childress, and Menachem Elimelech. Forward osmosis: Principles, applications, and recent developments. *Journal of Membrane Science*, 281:70–87, sep 2006.

[15] David L. Chapman. A contribution to the theory of electrocapillarity. *The London, Edinburgh, and Dublin Philisophical Magazine and Journal of Science*, 25:475–481, 1913.

[16] Shankararaman Chellam and Mark R. Wiesner. Particle Transport in Clean Membrane Filters in Laminar Flow. *Environmental Science and Technology*, 26(8):1611–1621, 1992.

[17] Maksym N. Chernyshov, G. Wytze Meindersma, and André B. de Haan. Modelling temperature and salt concentration distribution in membrane distillation feed channel. *Desalination*, 157(1-3):315–324, 2003.

[18] E. J. Clayfield, E. C. Lumb, and P. H. Mackey. Retarded dispersion forces in colloidal particles-Exact integration of the Casimir and Polder equation. *Journal of Colloid And Interface Science*, 37(2):382–389, 1971.

[19] Clayton T. Crowe, John D. Schwarzkopf, Martin Sommerfeld, and Yutaka Tsuji. *Multiphase Flows with Droplets and Particles*. CRC Press Taylor&Francis Group, 2 edition, 2012.

[20] Boris Derjaguin and Lev Landau. Theory of the stability of strongly charged lyophobic sols and of the adhesion of strongly charged particles in solutions of electrolytes. *Acta Physico Chimica URSS*, 14:633, 1941.

[21] Masao Doi. *Soft matter physics*. Oxford University Press, Oxford, 1 edition, 2013.

[22] Menachem Elimelech and William A. Phillip. The future of seawater desalination: Energy, technology, and the environment. *Science*, 333(6043):712–717, 2011.

[23] Hilding Faxén. Der Widerstand gegen die Bewegung einer starren Kugel in einer zähen Flüssigkeit, die zwischen zwei parallelen ebenen Wänden eingeschlossen ist. *Annalen der Physik*, 373(10):89–119, 1922.

[24] R. L.C. Flemmer and C. L. Banks. On the drag coefficient of a sphere. *Powder Technology*, 48(3):217–221, 1986.

[25] D. F. Fletcher and D. E. Wiley. A computational fluids dynamics study of buoyancy effects in reverse osmosis. *Journal of Membrane Science*, 245(1-2):175–181, 2004.

[26] C. Fritzmann, J. Löwenberg, T. Wintgens, and T. Melin. State-of-the-art of reverse osmosis desalination. *Desalination*, 216(1-3):1–76, 2007.

[27] Vítor Geraldes, Viriato Semião, and Maria Norberta De Pinho. Flow and mass transfer modelling of nanofiltration. *Journal of Membrane Science*, 191(1-2):109–128, 2001.

[28] P. Gleick and C. Iceland. Water, Security and Conflict. Technical report, World Resource Institute, 2018.

[29] John Gregory. Approximate Expressions for Retarded van der Waals Interactions. *Journal of Colloid and Interface Science*, 83(1), 1981.

[30] M. F. Gruber, C. J. Johnson, C. Y. Tang, M. H. Jensen, L. Yde, and C. Hélix-Nielsen. Computational fluid dynamics simulations of flow and concentration polarization in forward osmosis membrane systems. *Journal of Membrane Science*, 379(1-2):488–495, 2011.

[31] Louis G. Guoy. Sur la construction de la charge electrique a la surface d'un electrolyte. *Journal de Physique*, 9:657–668, 1910.

[32] Jacques S. Hadamard. Mouvement permanent lent d'une sphère eliquide et visqueuse dans un liquide visqueux. *Comptes Rendus de l'Académie des Sciences*, 152:1735–1738, 1911.

[33] H. C. Hamaker. The London-Van Der Waals attraction between spherical particles. *Physica*, 4(1):1058–1072, 1937.

[34] Nathan T. Hancock and Tzahi Y. Cath. Solute coupled diffusion in osmotically driven membrane processes. *Environmental Science and Technology*, 43(17):6769–6775, 2009.

[35] Christophe Henry, Jean Pierre Minier, and Grégory Lefèvre. Towards a description of particulate fouling: From single particle deposition to clogging. *Advances in Colloid and Interface Science*, 185-186:34–76, 2012.

[36] R. Hogg, T. W. Healy, and D. W. Fuerstenau. Mutual coagulation of colloidal dispersions. *Transactions of the Faraday Society*, 62(615):1638–1651, 1966.

[37] Gerhard Holzinger. OpenFOAM - A little user manual. Technical report, Johannes Kepler University, Linz, 2018.

[38] Nils Horstmeyer, Thomas Lippert, David Schön, Felizitas Schlederer, Cristian Picioreanu, Klaus Achterhold, Franz Pfeiffer, and Jörg E. Drewes. CT scanning of membrane feed spacers - Impact of spacer model accuracy on hydrodynamic and solute transport modeling in membrane feed channels. *Journal of Membrane Science*, 564(June):133–145, 2018.

[39] Andreas Kastl, Anne Bogler, Markus Spinnler, Thomas Sattelmayer, Avraham Be'er, and Edo Bar-Zeev. Impact of Hydrodynamics on the First Stages of Biofilm Formation in Forward Osmosis with Spacers. *Environmental science & technology*, 54(8):5279–5287, 2020.

[40] Florian Kiefer. *Multi-effect vacuum membrane distillation for high-recovery desalination*. PhD thesis, 2019.

[41] Sahan T.W. Kuruneru, Emilie Sauret, Suvash C. Saha, and Yuan Tong Gu. Coupled CFD-DEM simulation of oscillatory particle-laden fluid flow through a porous metal foam heat exchanger: Mitigation of particulate fouling. *Chemical Engineering Science*, 179(2018):32–52, 2018.

[42] Yu Ling Li, Kuo Lun Tung, Yu Shao Chen, and Kuo Jen Hwang. CFD analysis of the initial stages of particle deposition in spiral-wound membrane modules. *Desalination*, 287:200–208, 2012.

[43] Yu-Ling Ling Li, Ting-Hsiang Hsiang Chang, Chung-Yeh Yeh Wu, Ching-Jung Jung Chuang, and Kuo-Lun Lun Tung. CFD analysis of particle deposition in the spacer-filled membrane module. *Journal of Water Supply: Research and Technology - AQUA*, 55(7-8):589–601, 2006.

[44] Martin R. Maxey and James J. Riley. Equation of motion for a small rigid sphere in a nonuniform flow. *Physics of Fluids*, 26(4):883–889, 1983.

[45] Jeffrey R. McCutcheon and Menachem Elimelech. Influence of concentrative and dilutive internal concentration polarization on flux behavior in forward osmosis. *Journal of Membrane Science*, 284:237–247, 2006.

[46] Jeffrey R. McCutcheon and Menachem Elimelech. Modeling Water Flux in Forward Osmosis: Implications for Improved Membrane Design. *AIChE Journal*, 57(7):1736–1744, 2007.

[47] Jeffrey R. McCutcheon, Robert L. McGinnis, and Menachem Elimelech. A novel ammonia-carbon dioxide forward (direct) osmosis desalination process. *Desalination*, 174(1):1–11, 2005.

[48] Robert L. McGinnis and Menachem Elimelech. Energy requirements of ammonia-carbon dioxide forward osmosis desalination. *Desalination*, 207(1-3):370–382, 2007.

[49] Agustin Aragon Mesa, Claudio Miguez Gomez, and Ramon Urcelay Azpitarte. Energy saving and desalination of water. *Desalination*, 108(1-3):43–50, 1997.

[50] G. Micale, L. Rizzuti, and A. Cipollina. *Seawater desalination - Conventional and renewable energy processes*. Springer Berlin Heidelberg, 1 edition, 2009.

[51] Efstathios E. Michaelides. A novel way of computing the Basset term in unsteady multiphase flow computations. *Physics of Fluids A: Fluid Dynamics*, 4(7):1579–1582, 1992.

[52] Efstathios E. Michaelides. *Particles, bubbles, and drops: Their motion, heat and mass transfer*. World Scientific Publishing, Singapore, 2006.

[53] P. R. Neal, H. Li, A. G. Fane, and D. E. Wiley. The effect of filament orientation on critical flux and particle deposition in spacer-filled channels. *Journal of Membrane Science*, 214(2):165–178, 2003.

[54] J. T. G. Overbeek. The interaction between colloidal particles. *Colloid Science*, 1:245–277, 1952.

[55] Minkyu Park and Joon Ha Kim. Numerical analysis of spacer impacts on forward osmosis membrane process using concentration polarization index. *Journal of Membrane Science*, 427:10–20, 2013.

[56] S. V. Patankar and D. B. Spalding. *A calculation procedure for the transient and steady-state behaviour of shell-and-tube heat exchangers*. PhD thesis, Imperial College of Science and Technology, 1972.

[57] William A. Phillip, Jui Shan Yong, and Menachem Elimelech. Reverse draw solute permeation in forward osmosis: Modeling and experiments. *Environmental Science and Technology*, 44(13):5170–5176, 2010.

[58] Sherub Phuntsho, Ho Kyong Shon, Seungkwan Hong, Sangyoup Lee, and Saravanamuthu Vigneswaran. A novel low energy fertilizer driven forward osmosis desalination for direct fertigation: Evaluating the performance of fertilizer draw solutions. *Journal of Membrane Science*, 375(1-2):172–181, 2011.

[59] Wolfgang Polifke. Simulation of Thermo-Fluids with Open Source Tools. Technical report, 2019.

[60] A. I. Radu, M. S.H. van Steen, J. S. Vrouwenvelder, M. C.M. van Loosdrecht, and C. Picioreanu. Spacer geometry and particle deposition in spiral wound membrane feed channels. *Water Research*, 64:160–176, 2014.

[61] M. W. Reeks and S. McKee. The dispersive effects of Basset history forces on particle motion in a turbulent flow. *Physics of Fluids*, 27(7):1573–1582, 1984.

[62] C.J.F. Ridders. A new algorithm for computing a single root of a real continuous function. *IEEE Transactions on Circuits and Systems*, 26(11):979–980, 1979.

[63] P. J. Roache. Perspective: A method for uniform reporting of grid refinement studies. *Journal of Fluids Engineering, Transactions of the ASME*, 116(3):405–413, 1994.

[64] S. I. Rubinow and Joseph B. Keller. The transverse force on a spinning sphere moving in a viscous fluid. *Journal of Fluid Mechanics*, 11(3):447–459, 1961.

[65] John W. Ruge and Klaus Stüben. Multigrid Methods. In *Algebraic Multigrid*, pages 73–130. Society for Applied Mathematics, 1987.

[66] Witold Rybczynski. Über die fortschreitende Bewegung einer flüssigen Kugel in einem zähen Medium. *Bulletin International de l'Académie des Sciences de Cracovie*, pages 40–46, 1911.

[67] P. G. Saffman. The lift on a small sphere in a slow shear flow. *Journal of Fluid Mechanics*, 22(2):385–400, 1965.

[68] G. Schock and A. Miquel. Mass transfer and pressure loss in spiral wound modules. *Desalination*, 64:339–352, 1987.

[69] J. Schwinge, D. E. Wiley, and D. F. Fletcher. Simulation of the flow around spacer filaments between channel walls. 2. Mass-transfer enhancement. *Industrial and Engineering Chemistry Research*, 41(19):4879–4888, 2002.

[70] Raphael Semiat. Energy issues in desalination processes. *Environmental Science and Technology*, 42(22):8193–8201, 2008.

[71] R. F. Service. Desalination Freshens Up. *Science*, 313(5790):1088–1090, 2006.

[72] Devin L. Shaffer, Jay R. Werber, Humberto Jaramillo, Shihong Lin, and Menachem Elimelech. Forward osmosis: Where are we now? *Desalination*, 356:271–284, 2015.

[73] Mark A. Shannon, Paul W. Bohn, Menachem Elimelech, John G. Georgiadis, Benito J. Marias, and Anne M. Mayes. Science and technology for water purification in the coming decades. *Nature*, 452(7185):301–310, 2008.

[74] Lianfa Song and Menachem Elimelech. Particle Deposition onto a Permeable Surface in Laminar Flow. *Journal of Colloid and Interface Science*, 173(1):165–180, jul 1995.

[75] Markus Spinnler. *Desalination (Lecture Slides)*. Lehrstuhl für Thermodynamik, Technische Universität München, 2019.

[76] Otto Stern. Zur Theorie der elektrolytischen Doppelschicht. *Zeitschrift für Elektrochemie und Angewandte Physikalische Chemie*, 30:508–516, 1924.

[77] Georg G Stokes. *On the effect of internal friction of fluids on the motion of a pendulum*. Transactions of the Chambridge Pholosophical Society, Cambridge, 9 edition, 1851.

[78] Alberto Tiraferri, Ngai Yin Yip, Anthony P. Straub, Santiago Romero-Vargas Castrillon, and Menachem Elimelech. A method for the simultaneous determination of transport and structural parameters of forward osmosis membranes. *Journal of Membrane Science*, 444:523–538, 2013.

[79] R. Valladares Linares, Sz S. Bucs, Z. Li, M. AbuGhdeeb, G. Amy, and J. S. Vrouwenvelder. Impact of spacer thickness on biofouling in forward osmosis. *Water Research*, 57(4):223–233, 2014.

[80] J. van't Hoff. The Function of Osmotic Pressure in the Analogy between Solutions and Gases. *Proceedings of the Physical Society of London*, 9(1):307–334, 1887.

[81] Evert Verwey and Theodoor Overbeek. Theory of the stability of lyophobic colloids: the interaction of sol particles having an electric double layer. *Elsevir Publishing, Amsterdam*, 1948.

[82] J. Visser. On Hamaker constants: A comparison between Hamaker constants and Lifshitz-van der Waals constants. *Advances in Colloid and Interface Science*, 3(4):331–363, 1972.

[83] D. J. Vojir and E. E. Michaelides. Effect of the history term on the motion of rigid spheres in a viscous fluid. *International Journal of Multiphase Flow*, 20(3):547–556, 1994.

[84] Peter von Böckh and Christian Saumweber. *Fluidmechanik - Einführendes Lehrbuch*. Springer Vieweg, Berlin Heidelberg, 3 edition, 2013.

[85] Hermann von Helmholtz. Studien über elektrische Grenzschichten. *Annalen der Physik*, 243(7):337–382, 1879.

[86] J. S. Vrouwenvelder, D. A. Graf von der Schulenburg, J. C. Kruithof, M. L. Johns, and M. C. M. van Loosdrecht. Biofouling of spiral-wound nanofiltration and reverse osmosis membranes: A feed spacer problem. *Water research*, 43(3):583–594, feb 2009.

[87] H. G. Weller, G. Tabor, H. Jasak, and C. Fureby. A tensorial approach to computational continuum mechanics using object-oriented techniques. *Computers in Physics*, 12(6):620, 1998.

[88] Seokkwan Yoon and Antony Jameson. Lower-upper symmetric-gauss-seidel method for the euler and navier-stokes equations. *AIAA Journal*, 26(9):1025–1026, 1988.

A Appendix

A.1 OpenFOAM®

OpenFOAM® [87] is a C++ based library which allows for the evaluation of complex computational fluid dynamics (CFD) and related multi-physics problems. The framework consists of applications, which can be divided into solvers and utilities, and the underlying classes, which are stored in pre-compiled libraries. Solvers evaluate the governing equations for the regarded problem, while utilities perform pre- and post-processing tasks. During compilation, applications are dynamically linked to the corresponding pre-compiled OpenFOAM® libraries. Applications and libraries are stored in the applications and src directories, respectively. The run directory contains the files that are required to solve a case, i.e. a specific problem.
Each case directory in OpenFOAM® consists of three mandatory sub-folders, namely 0, constant and system. The initial and boundary conditions of the case are set in files in the 0 folder which are named after the respective flow variables. The geometric information of the case is stored in the polyMesh sub-folder of the constant folder. Additionally, the constant folder contains files to specify constant material properties (e.g. the file thermophysicalProperties, which contains information such as the laminar viscosity and the density of the fluid) and turbulence specifications of the flow. Lastly, all specification files for the applications that the case requires are stored in the folder system. Of these, the files controlDict, fvSchemes and fvSolution refer to the solver, while all other files concern pre- and post-processing utilities.

A.2 Grid Convergence Study

A grid convergence study was conducted to ensure that the numerical solution is independent from the mesh. The second finest mesh was applied for all simulations.

A.3 Additional Validation Case

The additional validation case for larger particles shows that our model does not hold for larger particles. In addition to the particle trajectories which we calculated with our model, Figure A.2 shows the flow conditions in the channel and the particle tracks which were determined by Chellam et al. [16].

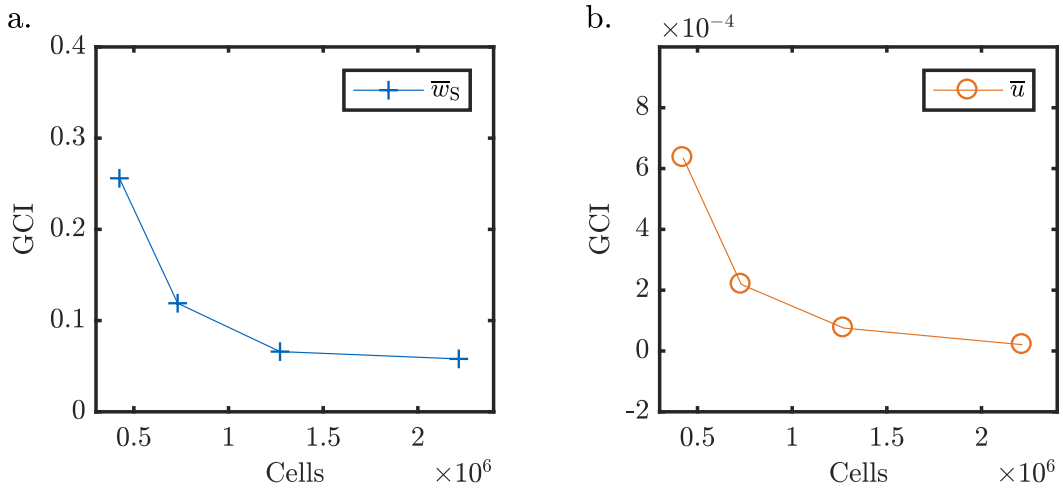

Figure A.1: Grid convergence index for a. the average salt mass fraction at the membrane in the third spacer element and b. the average crossflow velocity above the bottom spacer filament of the third spacer element.

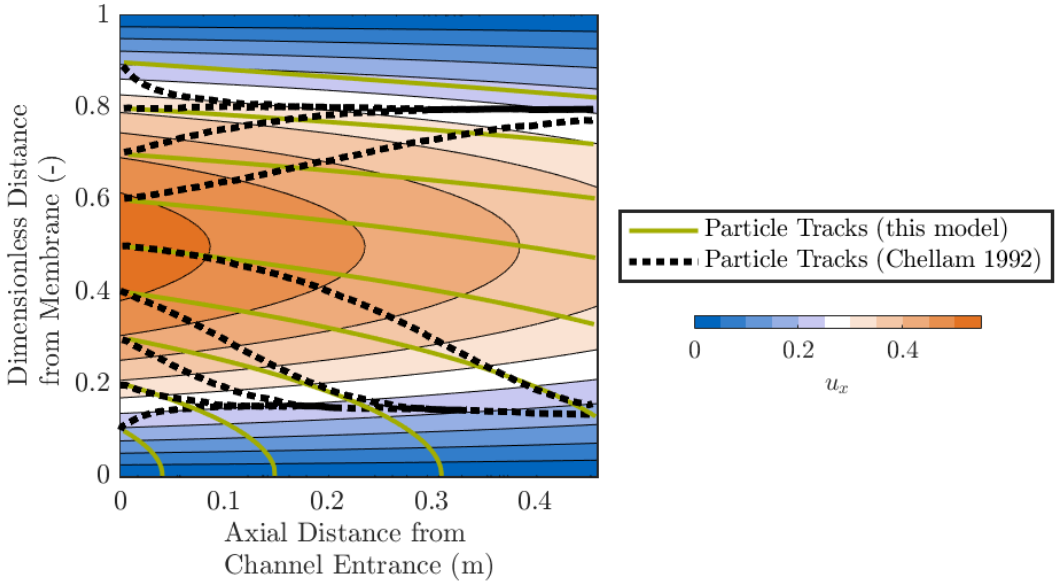

Figure A.2: Comparison of the particle trajectories of large particles ($d = 26\mu$m) calculated by Chellam et al. [16] with the particle trajectories determined with the present model.

A.4 Detailed Analysis of Flow Characteristics at the Membrane

The flow characteristics at the membrane were measured to determine the effect of concentration polarization on the local permeate water flux. The permeate water flux is inversely proportional to the salt mass fraction at the membrane and slightly higher than expected based on the calculations in section 3.5.3 (Figure A.3).

A.5 Additional Particle Trajectories

Figure A.4 shows the particle trajectories at high and medium crossflow velocity and uniform permeate water flux. The trajectories of the particles at locally varying permeate water flux are depicted in Figure A.5.

A.6 Control Experiments

A case which calculates the particle trajectories at a uniform permeate water flux that matches the permeate water flux of the case which resolves the concentration polarization was set up to ensure that the small difference in permeate water flux does not alter the particle trajectories. Figure A.6 compares the particle tracks of the ideal case with a permeate water flux of $2.78 \times 10^{-6}\,\mathrm{m\,s^{-1}}$ to an ideal case with permeate water flux of $2.88 \times 10^{-6}\,\mathrm{m\,s^{-1}}$ (Table 4.2). While the streamlines of the corresponding fluxes slightly deviate from each other, the particle trajectories coincide. Thus, the on average higher permeate water flux in the simulations which resolve concentration polarization is not responsible for the deviation of the particle trajectories close to the membrane between the ideal case and the real case.

A.7 Particle Size Distribution for the Deposition Studies

A Rosin-Rammler particle size distribution was injected into the forward osmosis channel

$$f(d_\mathrm{P}) = \frac{n}{d_\mathrm{P,mean}} \left(\frac{d_\mathrm{P}}{d_\mathrm{P,mean}} \right)^{n-1} \exp\left(-\left(\frac{d_\mathrm{P}}{d_\mathrm{P,mean}} \right)^{n} \right). \tag{A.1}$$

$n = 0.5$ and $d_\mathrm{P,mean} = 3\,\mu\mathrm{m}$ were chosen for the parameters for the distribution probability function. The resulting size distribution, which is pictured in Figure A.7, is common for ground and abberated matter, such as sand grains. In the simulations the particle size distribution is cut off at 0.5 µm and 5 µm, such that the average particle diameter at the inlet patch is 1.711 µm.

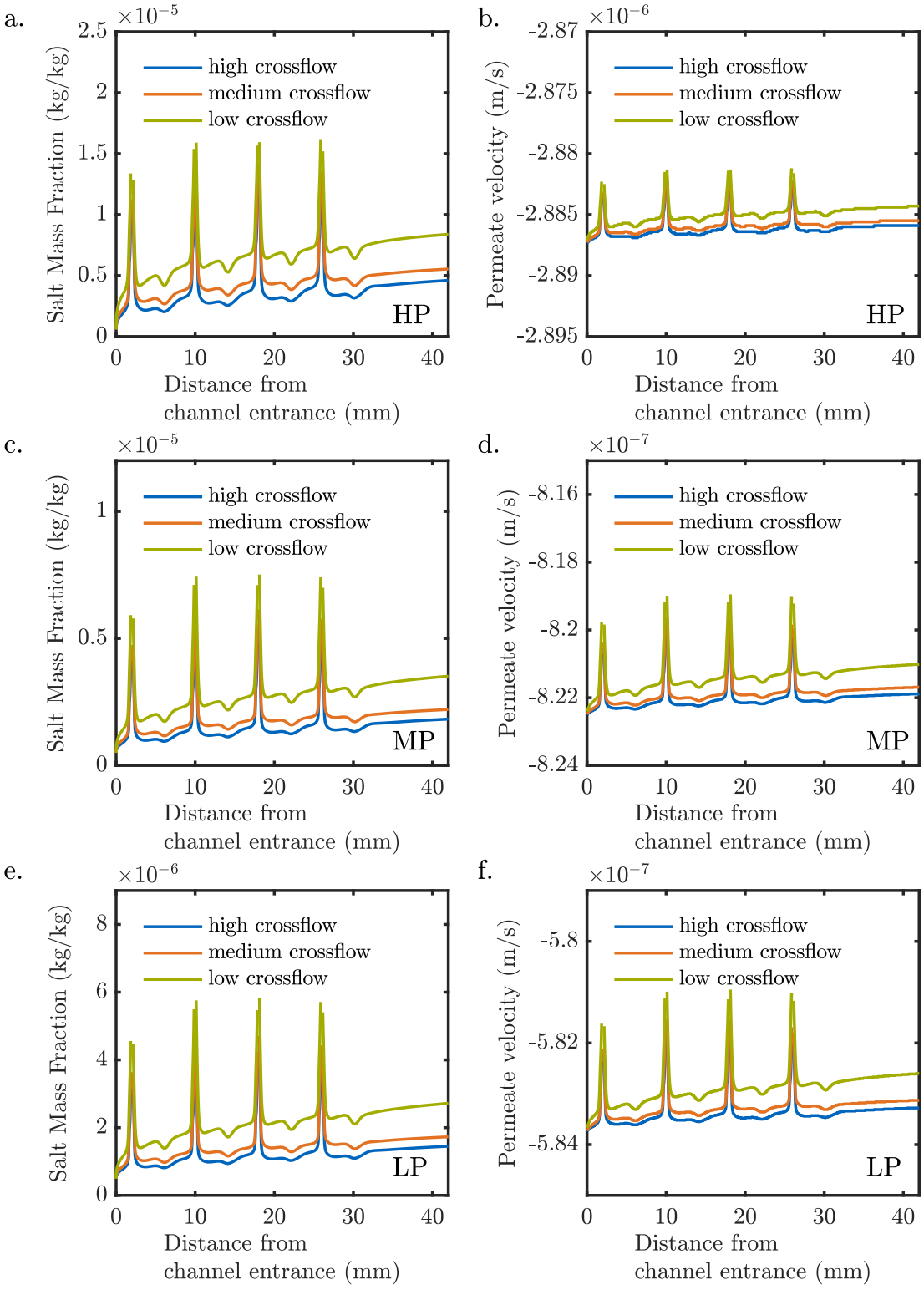

Figure A.3: Local salt mass fraction on the feed side of the membrane and permeate water flux at draw salt mass fractions of a. and b. 7.4×10^{-3} kg kg^{-1}, c. and d. 1.6×10^{-3} kg kg^{-1} and e. and f. 1.1×10^{-3} kg kg^{-1}.

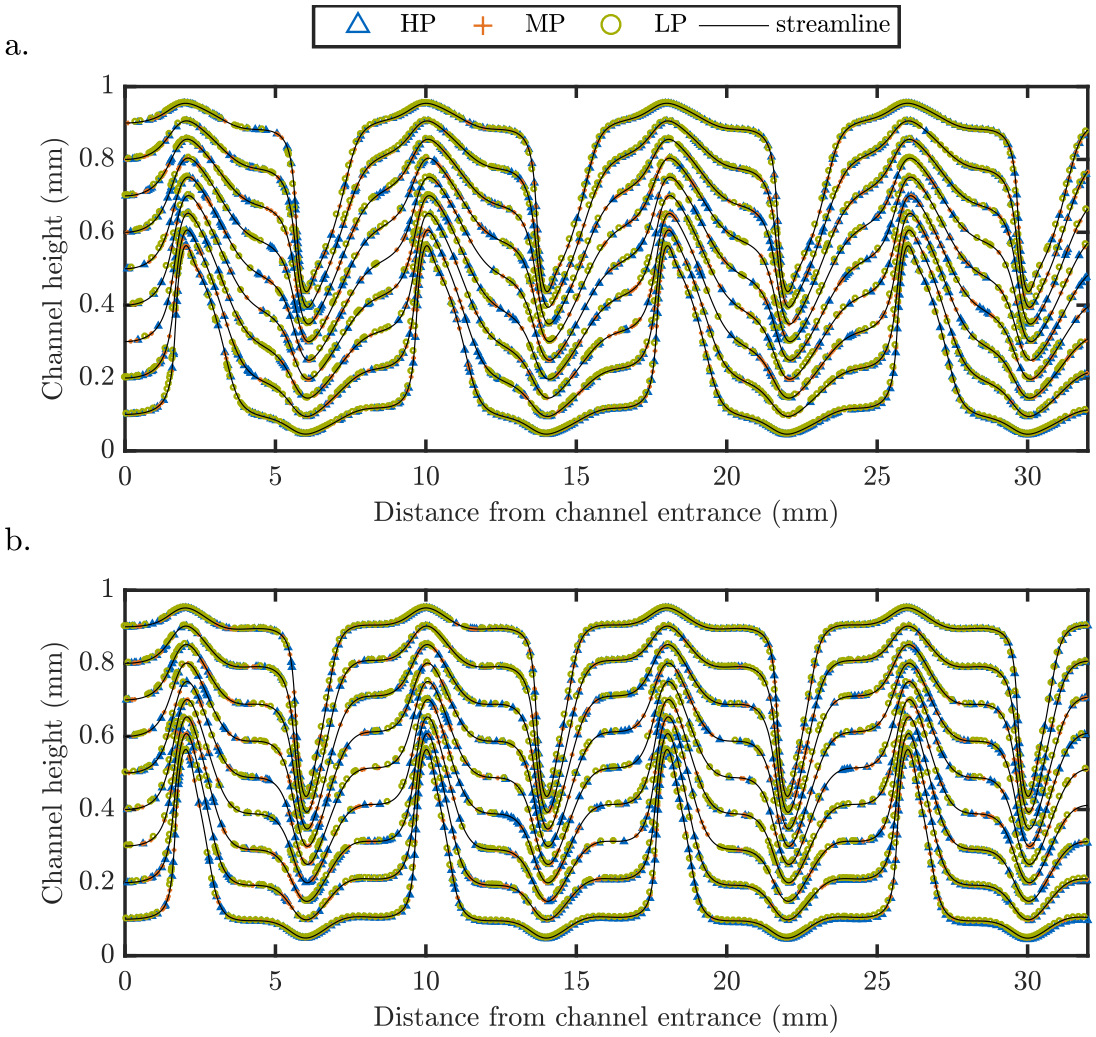

Figure A.4: Particle trajectories over four spacer elements at uniform crossflow velocities of a. $42.70 \times 10^{-3}\,\mathrm{m\,s^{-1}}$ (HC) and b. $20.00 \times 10^{-3}\,\mathrm{m\,s^{-1}}$ (MC). The streamlines are the streamlines of the flow without permeate water flux.

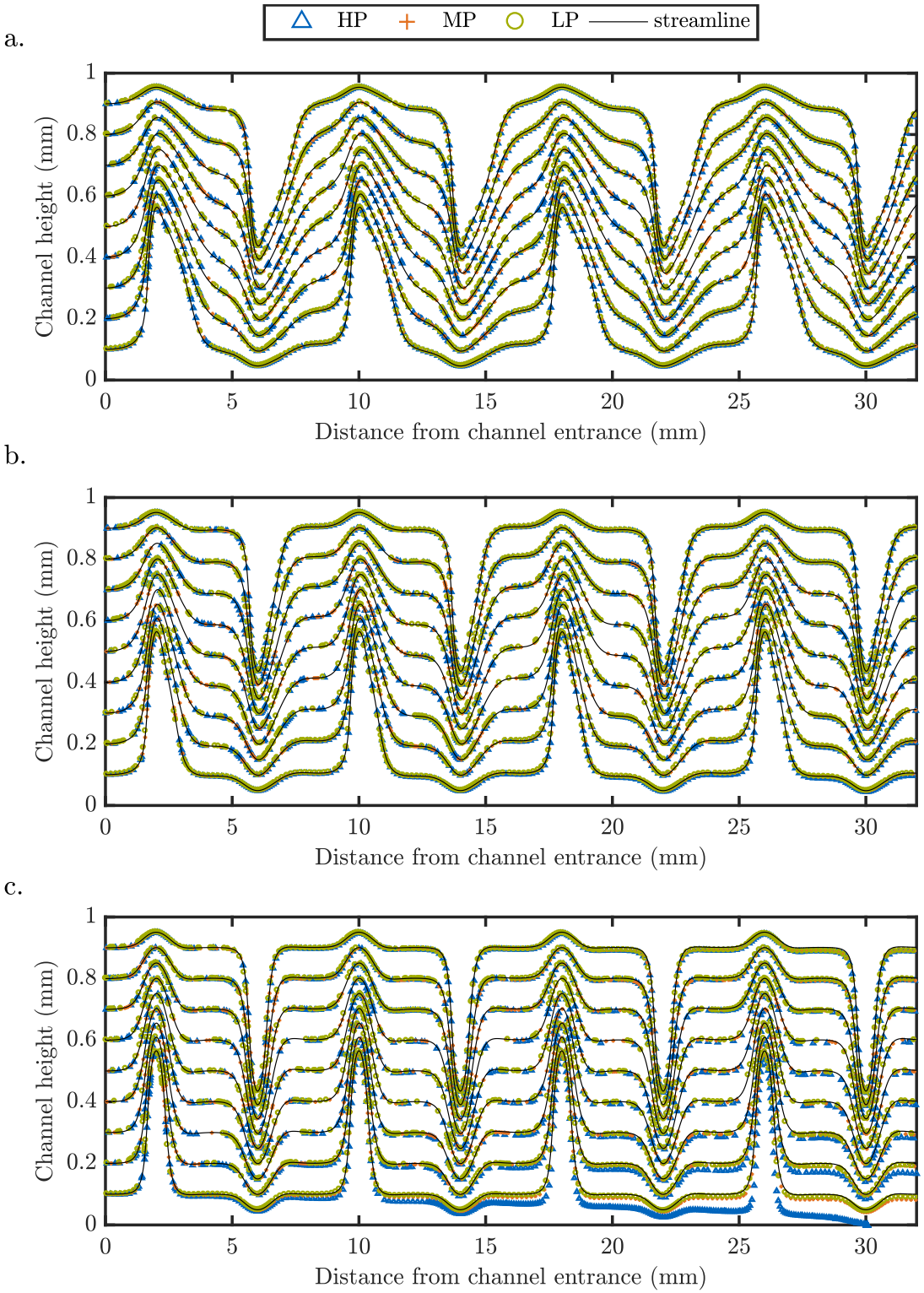

Figure A.5: Particle trajectories over four spacer elements at a crossflow velocity of a. $42.70 \times 10^{-3}\,\mathrm{m\,s^{-1}}$ (HC), b. $20.00 \times 10^{-3}\,\mathrm{m\,s^{-1}}$ (MC) and c. $3.34 \times 10^{-3}\,\mathrm{m\,s^{-1}}$ (LC). The trajectories consider local variations in permeate water flux due to concentration polarization. The streamlines are the streamlines of the flow without permeate water flux.

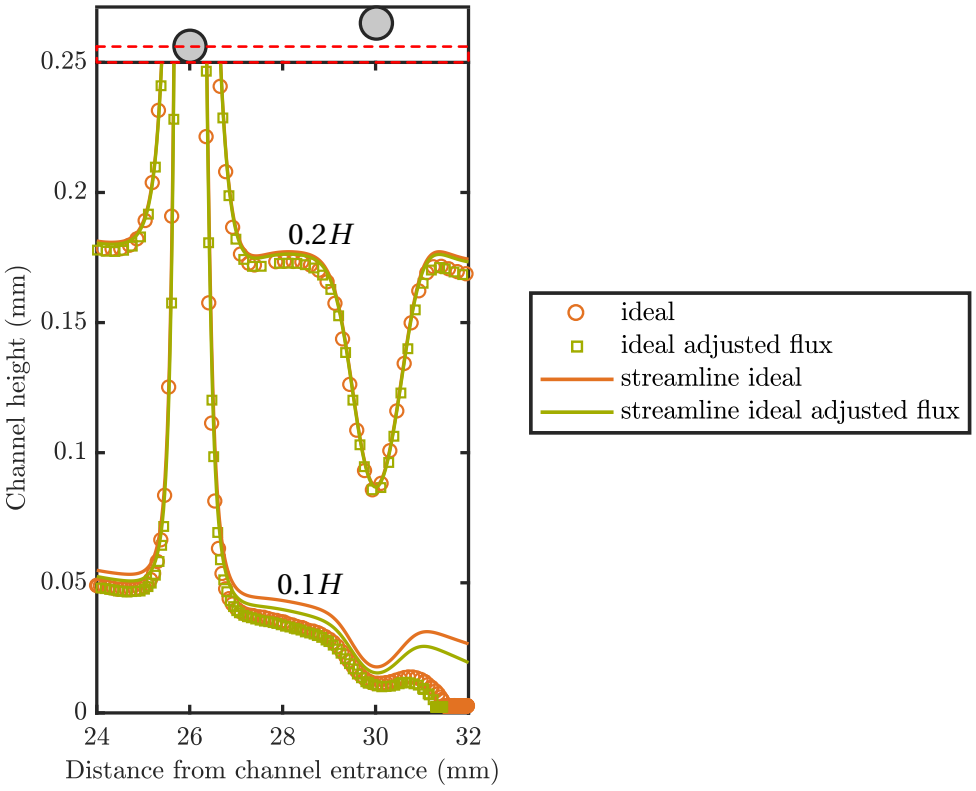

Figure A.6: Control experiment for the comparison of the particle deposition of the ideal with the real case.

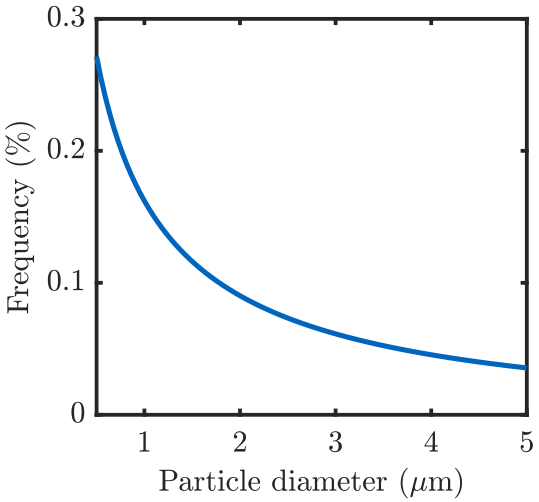

Figure A.7: Rosin-Rammler particle size distribution.